8-2022

Controlled Manipulation of Droplets on Fibers: Fundamentals and Printing Applications

Yueming Sun
yuemins@clemson.edu

CONTROLLED MANIPULATION OF DROPLETS ON FIBERS: FUNDAMENTALS AND PRINTING APPLICATIONS

A Dissertation
Presented to
the Graduate School of
Clemson university

In Partial Fulfillment
Of the Requirements for the Degree
Doctor of Philosophy
Materials Science and Engineering

By
Yueming Sun
August 2022

Accepted by:
Dr. Konstantin G. Kornev, Committee Chair
Dr. Fei Peng
Dr. Jianhua Tong
Dr. Ulf D. Schiller

ABSTRACT

In this dissertation, the drop interactions with a single fiber is discussed under an application angle for development on new Drop-on-Demand (DOD) printhead using a fiber-in-a tube platform[1] to print highly viscous materials[2]. To control the drop formation and manipulation on a fiber, one needs to know how the fiber wetting properties and the fiber diameter influence drop formation. And then one needs to know the effects of fiber movement in the device on drop formation. These two questions constitute the main theme of this dissertation

Before this study, it was accepted that the liquids could not form axisymmetric droplets if the liquid drop will make the contact angle greater than 90 degrees on flat substrate of the same material. In **Chapter 2**, all possible configurations of an axisymmetric drop wrapping up the fiber were analyzed rigorously by studying all solutions of the Laplace equation of capillarity for small droplets for which gravity is insignificant. In **Chapter 3**, an experimental analysis of morphological transitions of droplet configurations has been systematically conducted. When the droplets are large and are able to wrap up the fiber, they form barreled configurations; when the volume of droplets is small, the barrels cannot be formed and droplets rest as clamshells on the fiber side. With these analyses in hands, one can design of a fiber-in-a-tube printhead taking advantage of the established diagrams for formation of barreled droplets.

Drop-on-demand (DOD) printing is a versatile manufacturing tool, which has been widely used in applications ranging from graphic products to manufacturing of ceramics,

even for cell engineering. However, the existing DOD methods cannot be applied for highly viscous materials: the printing technologies are typically limited to the inks with the water level viscosity and fall short of ejecting jets from thick fluids and breaking them into droplets. To address this challenge, a new wire-in-a-tube technology for drop generation has been developed replacing the nozzle generator with a wire-in-a-tube drop generator[2]. In **Chapter 4**, we introduce the wire-in-a-tube generator and show successful printing results of droplets on-demand from highly viscous (~10 Pa*s) liquids. In **Chapter 5**, we study the drop formation mechanisms in the wire-in-a-tube drop generators. These mechanisms couple unique fluid mechanics, capillarity, and wetting phenomena providing a new platform that can be used in different microfluidic applications.

References

1. Andrukh, T., B. Rubin, and K.G. Kornev, *Wire-in-a-nozzle as a new droplet-on-demand electrogenerator.* Langmuir, 2011. **27**(6): p. 3206-10.
2. Sun, Y., et al., Making droplets from highly viscous liquids by pushing a wire through a tube. Physics of Fluids, 2022. **34**(3).

DEDICATION

This Dissertation is dedicated to my family for their support and encouragement throughout my PhD study.

ACKNOWLEDGMENTS

First, I would like to thank my advisor, Dr. Konstantin Kornev, for his guidance, patience, and encouragement during my PhD study at Clemson University. His passion about science, broad knowledge in multiple disciplines, ingenious insights on research, and hard work certainly inspired and helped me grow as a scientist. I would also like to express my gratitude to my committee members, Dr. Fei Peng, Dr. Jianhua Tong and Dr. Ulf Schiller for their valuable comments, suggestions, and time. I want to thank all the past and current group members, in particular, Dr. Chengqi Zhang, Dr. Pavel Aprelev, Luke Sande, Dr. Arthur Salamatin, Tatiana Stepanova, Vaibhav Palkar, Brennan Shealy, Bochuan Sun, Dr. Alexandre Palaoro, Dr. Fang Wang, Artis Brasovs, Griffin Donley, Adam Puchalski, Deborah George, Akshata Ramchandra Gole, Megan Williams for their help and support during this journey. I would also like to thank David White, Kimberly Ivey, James Lowe, Stanley Justice, Diane Swope and all other faculty and staff members of MS&E department for their continuous support. I would like to thank all my close friends especially Xiao Geng, Ming Lei, Jianxing Ma for making my life enjoyable and memorable at Clemson. I would also like to thank my girlfriend, Chenglu Yu for always supporting my work and decisions from 12250 kilometers away. Last but certainly not least, I would like to thank my parents. No words can ever describe my gratefulness for your unwavering support and encouragements. You are the greatest parents in the World.

TABLE OF CONTENTS

Page

LIST OF TABLES

Table Page

LIST OF FIGURES

Figure Page

CHAPTER I

SUMMARY

Spherical drop is the most common configuration of an unconfined liquid body. The drop takes on its spherical shape owing to its surface tension. Depending on the substrate properties, droplets of the same liquid can make different configurations. Although the relationship between drop configurations and properties of flat substrates has been well established, the relationship between drop configurations and properties of cylindrical substrate is poorly understood. The lack of understanding of the mechanisms of drop shaping on the fibers hinders the development of fiber-based microfluidic devices. With the rapid development of advanced materials, drops made of surfactant solutions, ceramic precursors, and bio-polymeric materials are widely required in novel applications. Printing applications are growing. However, many advanced materials show high viscosity, which is hard to be manipulated using the traditional 3D printer. In this dissertation, we focus on two main problems: 1) how to control the drop morphology on the fiber and 2) how to manipulate highly viscous materials. Both problems are discussed theoretically and experimentally. The structure of this dissertation is as follows.

In **Chapter 2**, we theoretically analyzed all possible configurations of axisymmetric droplets on fibers. It is shown that the drops can be subdivided into two families, unduloidal and nodoidal droplets. The maximum drop radius R_{max}, capillary pressure ΔP , drop volume V, and contact angle θ are the main parameters controlling the droplet shape. It is confirmed that axisymmetric droplets can be formed for the entire range of

contact angles $0 < \theta < \pi$. This discovery opens up a new avenue for the development of fiber-based microfluidic devices for different applications.

In **Chapter 3**, we studied the transition between clamshell and barreled drops on fibers by controlling the drop radius R_d, advancing contact angle θ_{adv} and receding contact angle θ_{rec}. Experiments carried out for the transition of barrel-clamshell, and clamshell-barrel indicate two distinguishing scenarios of morphological transition of drop configurations on fibers. We also confirm that the contact angle hysteresis is responsible for asymmetry of barreled drop transited from the clamshell drop.

In **Chapter 4**, we introduce a novel wire-in-a-tube DOD generator. Using this technique, we printed single droplets on-demand from highly viscous materials with a narrow size distribution, which have been considered non-printable for the existing DOD print-heads.

In **Chapter 5**, a new wire-in-a-tube printhead has been analyzed. First, we discuss the mechanisms of drop formation in the wire-in-a-tube drop generators. We suggest a fluid flow model explaining the ink pickup when the wire moves through the tube and specify the critical conditions for the net ink displacement. These results can be used not only for developing wire-in-a-tube printing devices but also for developing the fiber coating methods when one threads a fiber through a liquid-filled tube. Then we experimentally study the dynamics of drop formation in the wire-in-a-tube generators and investigate the pressure distribution by modeling the drop and meniscus with unduloids and nodoids, respectively. This preferential flow explains the drop formation mechanism on demand: once the drop is nucleated, it grows by pulling the liquid mostly from the film. The liquid bridge connecting this nucleated drop with the meniscus squeezes the ink down to the tube, hindering communication of the drop with the feeding tube. This way, the drop remains dynamically isolated from the feeding tube. The depletion and breakup of this liquid bridge work in favor of this DOD technology. The size of the final drop is mostly controlled by the stick-out length of the wire and the wire radius. We showed that the thinner the wire and the wider the wire-tube gap thickness, the shorter the time of drop formation.

CHAPTER II

COULD NON-WETTABLE FIBER HOST AXISYMMETRIC DROPLETS?

2.1 Introduction

Since childhood, droplets of water or glue on spider webs[1-3] and needle-like leaves[4-6] capture people's attention and make us wonder how could the drop finds its perfect symmetric shape and stays unperturbed for a long time. These droplets always fascinate photographers and inspire the development of novel fiber-based microfluidics ranging from fiber-based liquid collectors and fabric-based filters to the fluid delivery devices[2, 7-10]. Perfectly axisymmetric shape of droplet suggests that the human eye cannot detect any surface deformation caused by the droplet weight. Thus, the drop shape is fully controlled by its surface properties and the surface properties of the material it interacts with. Interactions between the drop, surrounding fluid and the substrate are manifested through the contact angle that the drop forms with the substrate. A flat substrate is called wettable by the given liquid when its drop makes contact angle less than $90°$ with it. If the drop makes contact angle greater than $90°$, a flat substrate is considered practically non-wettable implying that the drop could be easily shaded off from the substrate. Using the $90°$ contact angle as the upper limit for classification of wettable surfaces is practically attractive, but not necessarily correct as it comes to the condition of drop detachment[11, 12].

Therefore, the analyses of conditions of wetting and dewetting of flat surfaces received the deserved attention of physicists and materials scientists and the $90°$ contact angle criterium was corrected to include different physico-chemical characteristics of substrates [11, 13, 14]. One cannot say the same about fibers. Wetting of fibers remained poorly understood and offers many surprises calling for special approach in classification of fiber wettability [8, 15-20]. Take, for example, a low surface tension oil, which would readily wet a flat surface and spread over it forming a puddle, [11]Fig. 2.1(a). However, on a fiber made of the same material, oil would not form a sheath analogous to a 2D puddle. The drop may form either an asymmetric clamshell or an axisymmetric barrel-like drop[21] (Fig 2.1(b) and Fig 2.1(c)).

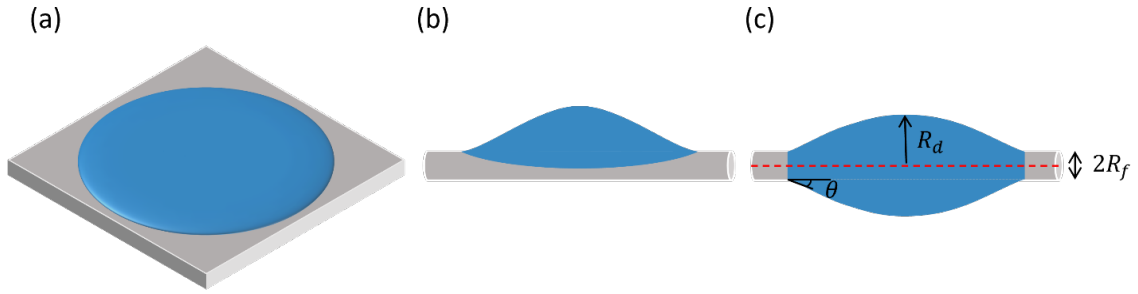

Fig. 2.1 (a) A drop of a wetting liquid spreads on a flat surface. On a fiber made of the same material, the same drop may form either a clamshell drop (b) or a barrel drop (c). The shape of the barrel drop with its maximum radius R_d is controlled by the contact angle (θ), the fiber radius R_f and droplet volume.

Joseph Plateau was, probably, the first to rigorously study spontaneous formation of the barrel-like droplets on fibers[22, 23]. D'Arcy Wentworth Thompson found very many applications of this fundamental work to biology[24]. Since then, spontaneous formation

of droplets by fibrous materials attracted attention of biologists and engineers[1, 15-17, 25-27].

The shape and conditions of equilibrium of a single axisymmetric barrel-like droplet on fiber is less understood[8, 18-20, 28, 29]. Carroll[30] postulated that the profile of the barrel-like drop must be described by unduloids, a family of the constant mean curvature surfaces[31]. Surprisingly, to the best of our knowledge, the other family of the constant mean curvature surfaces, nodoids, has never been investigated for description of drops on fibers.

In this chapter, we fill this gap by theoretically studying all possible shapes of axisymmetric droplets on fibers. Nodoidal and unduloidal droplets are investigated and the transition from one family to another is determined. It is shown that the Carroll choice of unduloidal droplet model has its limitations. To describe all possible wetting scenarios, one needs to include nodoidal droplets. Nodoidal droplets significantly enrich the family of barrel-like axisymmetric droplets. The fibers could be completely wrapped up by these droplets even if the droplets make contact angles greater than $90°$. We attempted to experimentally validate the theory and showed that the droplets do wrap up non wettable fibers, but the shape of these droplets are not necessarily axisymmetric. Thus, a more thorough analysis is required to answer the question on possible formation of axisymmetric droplets on non-wettable fibers.

2.2 Equilibrium shapes of droplets on fibers

2.2.1 Laplace law for axisymmetric droplets

The equilibrium droplets must have constant pressure everywhere inside the liquid and the difference in pressure P^- inside the liquid body and pressure P^+ in surrounding fluid is determined by the Laplace law of capillarity as[13, 32]:

$$P^- - P^+ = \sigma\left(\frac{1}{R_r}+\frac{1}{R_g}\right) \tag{2.1}$$

where R_r and R_g are two principal radii of curvature, and σ is the interfacial tension between phases. For example, if the surrounding fluid is air, P^+ equals to the atmospheric pressure, and σ is the surface tension of the liquid. In applications to axisymmetric droplets on fibers, the two principal radii of curvature at an arbitrary point on the drop surface are determined as follows, Fig. 2.2.

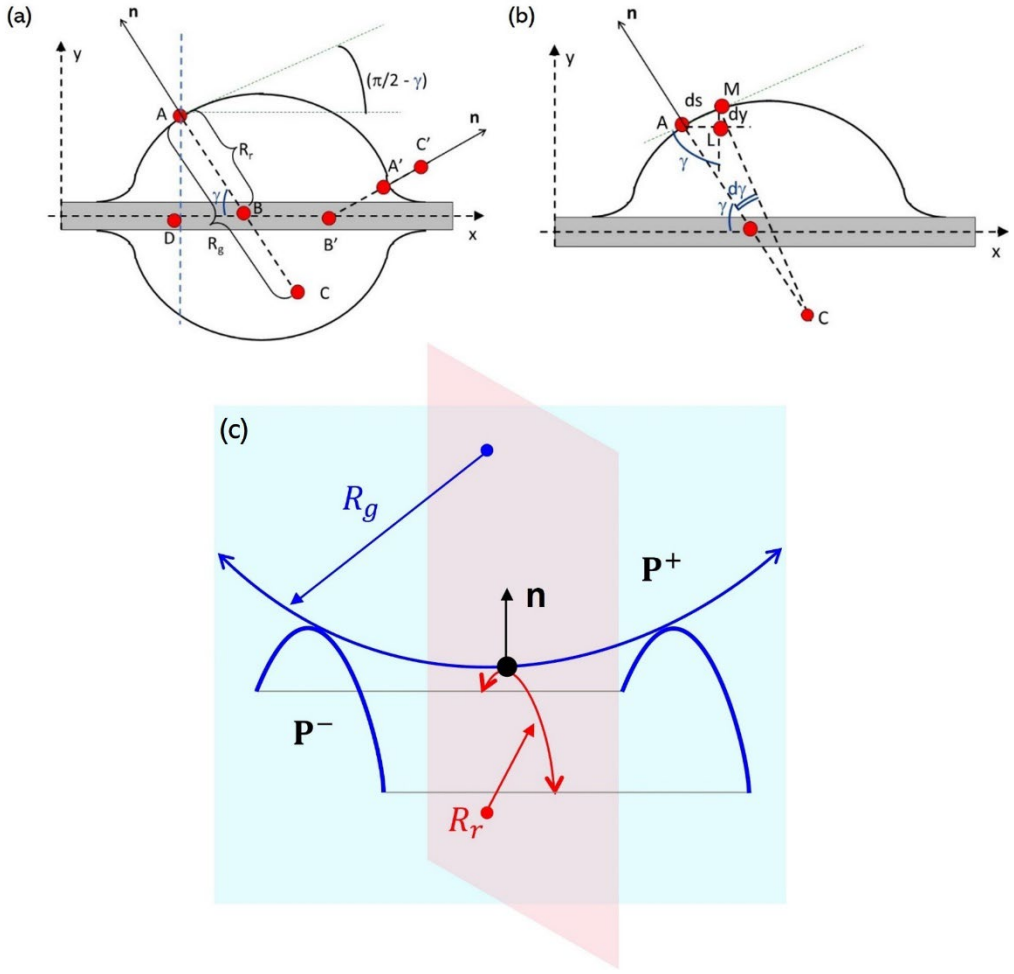

Fig. 2.2 The first principal radius of curvature $R_g = AB$ in Fig. 2.2(a) is merely the curvature of the plane curve AA', $1/R_g = d\gamma/ds$, where angle γ is defined in Fig. 2.2(a), and $d\gamma$ is defined in Fig. 2.4(b) and s is the arc length of the generator. The second principal radius of curvature R_r is obtained by continuing the ray along the normal vector until it intersects the fiber axis at point B, see Fig. 2.2(a). Noticing that the angle $\widehat{DBA} = \gamma$ of the right triangle ADB is related to the inclination angle $\pi/2 - \gamma$ formed by the tangent at point A with the $x-$axis, one can relate $|AB| = R_r$ with the drop radius at point A as $R_r = y/\sin\gamma$. (c) A saddle-like surface element of a surface of revolution with R_r and R_g as the two principal radii of curvature. The centers of curvatures are separated by the generator; therefore, one curvature is positive, and the other is negative.

The drop is obtained by rotating the generator, a plane curve AA' in Fig. 2.2, around the x-axis. Taking an arbitrary point A at the droplet surface, which generator curve is described by function $y = y(x)$, and drawing the outward normal vector $\boldsymbol{n}$, we define the two principal radii of curvature, R_r and R_g by continuing the ray along the normal vector as shown in Fig. 2.2. This ray is shown as the dashed line; it intersects the fiber axis at point B.

When the centers of curvatures, i.e. the centers of the circles described by R_r and R_g, are positioned on the same side of generator curve, these curvatures, $1/R_r$ and $1/R_g$ are defined positive. In the opposite case, one is positive, the other is negative. For example, when the drop wets the fiber completely making zero contact angle, an infinitesimally small patch on meniscus looks like a saddle shown in Fig. 2.2(c), and one radius of principal curvature, R_r, is positive and another, R_g , is negative.

The principal radius of curvature of the generator $y = y(x)$ at arbitrary point A is defined as the radius of curvature of this plane curve $y = y(x)$. The center of this radius of curvature is positioned at point C in Fig. 2.2(a), thus,

$$R_g = |\mathrm{AC}| = \frac{d\gamma}{ds}, \tag{2.2}$$

where angle γ is defined in Fig. 2.2(a), $d\gamma$ is defined in Fig. 2.2(b), and s is the arc length of the generator.

The drop radius $y = |AD| = y(x)$ at position x along the fiber is measured with respect to the fiber axis where $y = 0$. Therefore, the principal radius of curvature of the rotational plane can be expressed as,

$$R_r = \frac{y}{\sin\gamma}. \tag{2.3}$$

Turning to the right triangle $AB'A'$ and noticing that the angle $\widehat{AA'B'}$ in Fig. 2.2 (b) is equal to γ, and the side $B'A$ of this triangle is equal $|B'A'| = dy$, we have

$$ds = \frac{dy}{cos\,\gamma}, \Longrightarrow R_g = \frac{d\gamma}{ds} = \frac{d\gamma}{dy} cos\,\gamma\,. \tag{2.4}$$

Substituting Eq. (2.3) and (2.4) into the Laplace equation of capillarity Eq. (2.1), one obtains

$$\frac{\Delta P}{\sigma} = \frac{d\gamma}{dy} cos\,\gamma + \frac{1}{y} sin\,\gamma \tag{2.5}$$

It is convenient to express the angle γ in terms of derivatives of $y(x)$. The slope of the tangent to the drop surface at point A is defined as

$$\frac{dy}{dx} = tan\left(\frac{\pi}{2} - \gamma\right) = \cot\gamma\,. \tag{2.6}$$

Then Eq. (2.3) is rewritten as

$$R_r = y\sqrt{1 + cot^2\,\gamma} = y\left(1 + y'^2\right)^{-\frac{1}{2}}. \tag{2.7}$$

The curvature of the generator curve, $1/R_g$, can also be written in terms of derivatives of $y(x)$,

$$\frac{1}{R_g} = \frac{d\gamma}{ds} = y''(1 + (y')^2)^{-3/2}. \tag{2.8}$$

Therefore, any local pressure at the surface of any axisymmetric liquid body is given by the following formula,

$$P^- = P^+ + \sigma\left(y^{-1}(1+(y')^2)^{-1/2} + y''(1+(y')^2)^{-3/2}\right). \quad (2.9)$$

2.2.2 Two families of constant mean curvature surfaces

According to the Laplace law, in equilibrium, $H = \frac{1}{R_r} + \frac{1}{R_g} = const$, i.e., the liquid body is bounded by a constant mean curvature surface. To find the solutions to the family of constant mean curvature surfaces, , we integrate (2.5) and write the first integral as

$$y\,sin\,\gamma = \frac{\Delta P}{2\sigma}y^2 + \frac{\sigma}{\Delta P}C. \quad (2.10)$$

Determined by the integration constant C, all solutions (2.10) are divided into two families. When this constant varies between $0 \leq C \leq 1/2$, the surfaces of this family are called "unduloids"; when the constant is negative $C < 0$, the surfaces of this family are called "nodoids" [31]. The physical meaning of constant C will be discussed later in this chapter. These two families of constant mean curvature surfaces will be used to describe the drop configurations on fibers.

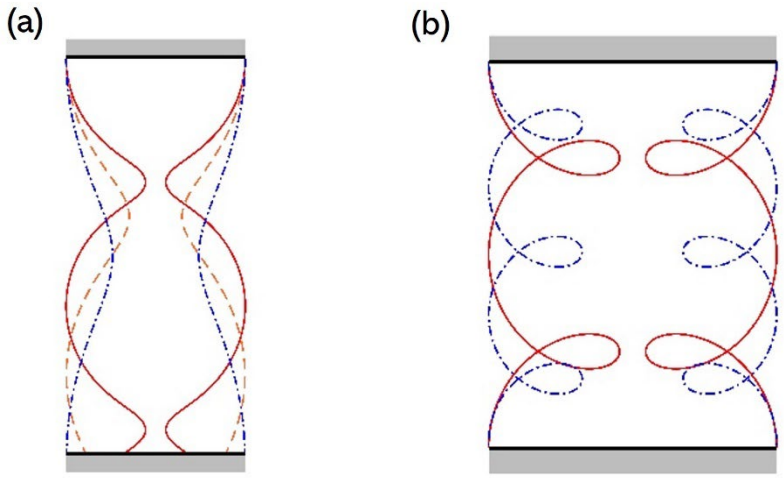

Fig. 2.3 (a) Series of unduloids. (b) Series of nodoids. To obtain these surfaces, the Laplace equation (2.5) was parameterized by arc length and rewritten as a set of first-order differential equations $\frac{dx}{ds} = cos\,\gamma$, $\frac{dy}{ds} = sin\,\gamma$, $\frac{d\gamma}{ds} = \frac{\Delta P}{\sigma} - \frac{sin\,\gamma}{y}$. *Integrating from s=0 with different parameters* $\frac{\Delta P}{\sigma}$, *these examples were obtained for (a)* $\frac{\Delta P}{\sigma} = 0.22\ mm^{-1}$ *and* $R_{min} = 1.1\ mm$, *solid curves,* $\frac{\Delta P}{\sigma} = 0.126\ mm^{-1}$ *and* $R_{min} = 0.45\ mm$ *dashed curves and* $\frac{\Delta P}{\sigma} = 0.072\ mm^{-1}$ *and* $R_{min} = 0.2\ mm$ *broken curves;(b)* $\frac{\Delta P}{\sigma} = -0.2\ mm^{-1}$ *and* $R_{min} = 1\ mm$, *solid curves and* $\frac{\Delta P}{\sigma} = -0.28\ mm^{-1}$ *and* $R_{min} = 1\ mm$ *broken curves*

2.3 Unduloidal droplets

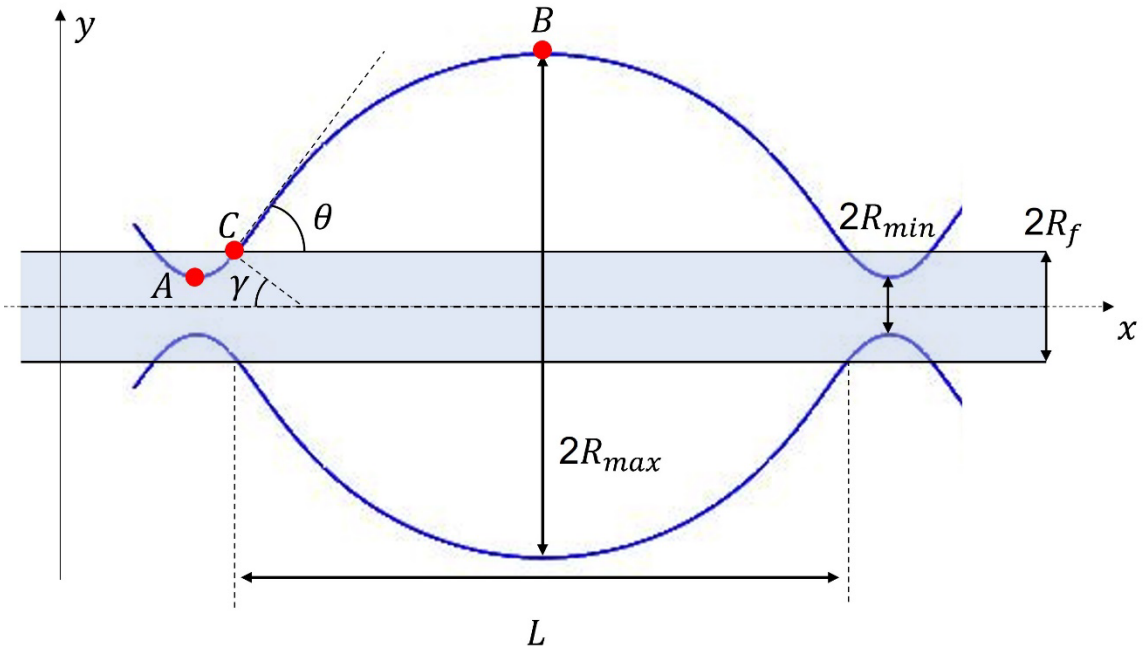

Fig. 2.4 Schematic of a unduloidal drop wrapping a fiber

We assume that there is a unduloidal drop sitting on a fiber with radius R_f, and the drop forms contact angle θ with the fiber surface (see Fig. 2.6).

At the neck of the unduloid (point A in Fig. 2.4), we have $\gamma = \frac{\pi}{2}$ and $y = R_{min}$. Therefore, Eq. (2.10) is written as

$$R_{min} = \frac{\Delta P}{2\sigma} R_{min}^2 + \frac{\sigma}{\Delta P} C. \tag{2.11}$$

At the bulge of the unduloid (point B in Fig. 2.4), we have $\gamma = \frac{\pi}{2}$ at $y = R_{max}$. Therefore,

$$R_{max} = \frac{\Delta P}{2\sigma} R_{max}^2 + \frac{\sigma}{\Delta P} C. \tag{2.12}$$

Solving these two equations $(2.11) - (2.12)$ for the pressure drop, we immediately obtain

$$\Delta P = \frac{2\sigma}{R_{max} + R_{min}}. \tag{2.13}$$

Solving for constant C, we have

$$C = \frac{\Delta P R_{min}}{\sigma} - \frac{1}{2}\left(\frac{\Delta P}{\sigma}\right)^2 R_{min}^2 = \frac{2R_{max}R_{min}}{(R_{max} + R_{min})^2}. \tag{2.14}$$

Since $R_{max} > R_{min} > 0$ in Eq. (2.13), the pressure drop in the unduloid is always positive suggesting that the pressure inside unduloid is always greater than the pressure of the surrounding fluid. Moreover, investigating the Eq. (2.14), we confirm that the constant varies between $0 \leq C \leq 1/2$. As $R_{min} \to 0$, the unduloid transforms into a sphere, and the constant C goes to zero; as $R_{min} \to R_{max,}$ the unduloid transforms into a circular cylinder, and the constant C goes to 1/2. Thus, Eq. (2.10) contains all possible unduloidal solutions.

2.3.1 Profile of unduloidal drop

We are in position to apply the unduloidal solution (2.10) for description of profile of the drop on fiber. In the general case of unduloidal solution, the neck of the unduloid describing the drop is invisible, Fig. 2.4. Therefore, to use Eq. $(2.13) - (2.14)$ the neck radius has to be determined. To find it, we apply Eq. (2.10) at the fiber surface where the drop meets the fiber at contact angle θ.

At the contact line between the unduloidal drop and fiber (point C in Fig. 2.4), we have $\gamma = \frac{\pi}{2} - \theta$ at $y = R_f$. Therefore,

$$R_f \sin\left(\frac{\pi}{2} - \theta\right) = \frac{\Delta P}{2\sigma} R_f^2 + \frac{\sigma}{\Delta \mathrm{P}} \mathrm{C}. \tag{2.15}$$

Solving Eq. (2.12) and Eq. (2.15) for pressure drop ΔP, we find the following expression

$$\Delta P = 2\sigma \frac{R_{max} - R_f \cos\theta}{R_{\max}^2 - R_f^2} \tag{2.16}$$

Substituting Eq. (2.16) in Eq. (2.13), the neck radius of the unduloid can be rewritten in terms of observable parameters

$$R_{\min} = \frac{R_{\max}^2 - R_f^2}{R_{max} - R_f \cos\theta} - R_{\max} \tag{2.17}$$

Similarly, C can be rewritten as,

$$C = \frac{2R_{max}R_f\left(R_{max} - R_f\cos\theta\right)\left(R_{max}\cos\theta - R_f\right)}{\left(R_f^2 - R_{max}^2\right)^2} \tag{2.18}$$

In order to ensure the existence of an unduloidal drop on fiber, we have to guarantee that the following conditions are met:

1) The neck radius of the unduloid must be positive and smaller than the fiber radius.

$$0 \le R_{\min} \le R_f, \Longrightarrow 0 \le \frac{R_{\max}^2 - R_f^2}{R_{max} - R_f\cos\theta} - R_{\max} \le R_f \tag{2.19}$$

2) The bulge of the unduloid must be above the surface of the fiber, $R_f < R_{max}$.

3) In conditions 1-2, the contact angle θ is allowed to change from $0°$ to $90°$, therefore, $0 \leq \cos\theta \leq 1$.

Solving the left-hand side of the inequality (2.19) for R_{max} with constraints $R_f < R_{max}$ & $0 \leq \cos\theta \leq 1$, we have

$$\frac{R_f}{\cos\theta} \leq R_{max} \tag{2.20}$$

Solving the left-hand side of the inequality (2.19) for R_{max}, we have $\cos\theta \leq 1$, which holds true. Thus, $R_f \leq \frac{R_f}{\cos\theta}$ holds true. Thus, for the given contact angle θ that varies from $0°$ to $90°$, we can always find an unduloidal drop sitting on a fiber with radius R_f. The maximum radius of this drop must be greater than $\frac{R_f}{\cos\theta}$.

2.3.2 Characteristic features of unduloidal droplets on fibers

The drop of limiting radius $R_{max} = \frac{R_f}{\cos\theta}$ has a very special geometrical meaning. Substituting $R_{max} = \frac{R_f}{\cos\theta}$ in Eq. (2.18), we find that $C = 0$. This constant C=0 corresponds to the case when the unduloid turns into a sphere. Since $R_{max} = \frac{R_f}{\cos\theta}$ specifies the smallest radius of unduloidal drop, Eq. (2.20), this spherical drop of radius $\frac{R_f}{\cos\theta}$ sets up the boundary of existence of unduloidal droplets on fibers. Below the curve $n = R_{max}/R_f$ shown in Fig. 2.5, no unduloidal droplets can occur.

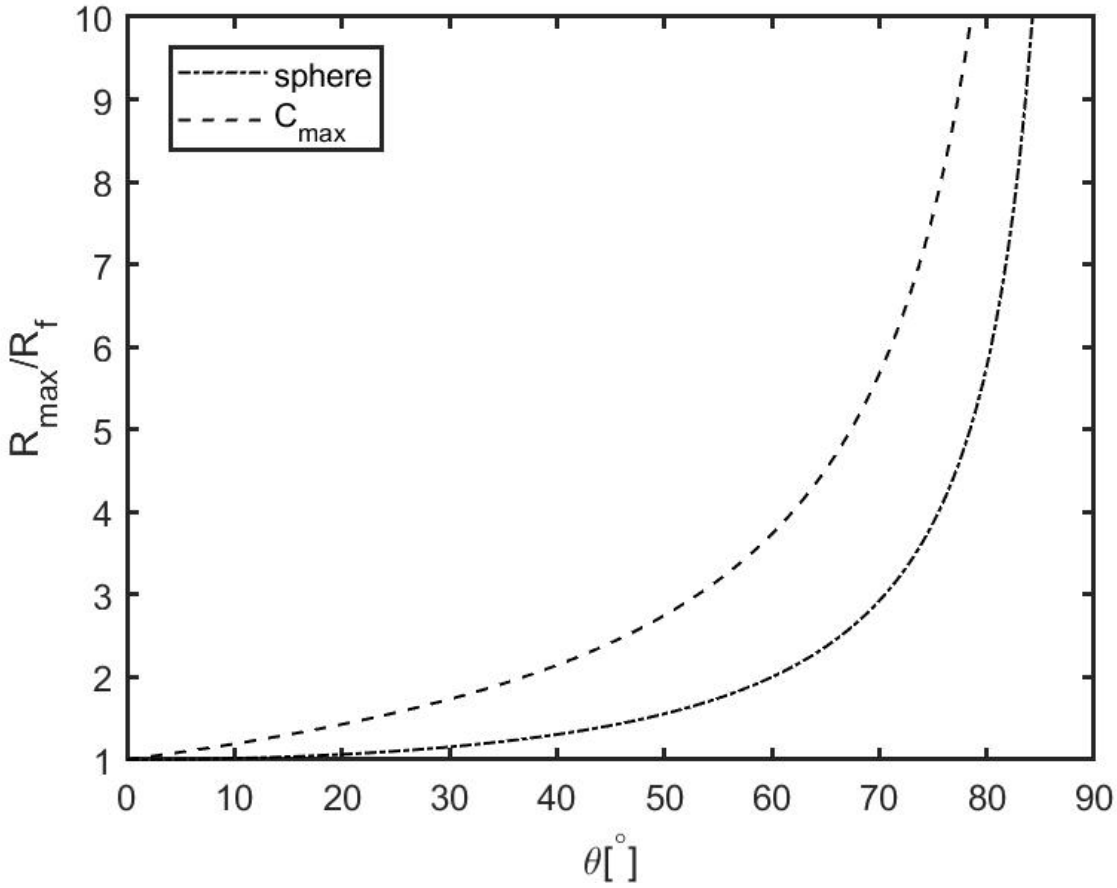

Fig. 2.5 The broken curve specifies the boundary where the unduloidal drop becomes spherical. Below this curve, no unduloidal droplets wrapping up the fiber can occur. The dashed curve specifies the boundary where the maximum value of integration constant C for unduloidal drop has been reached.

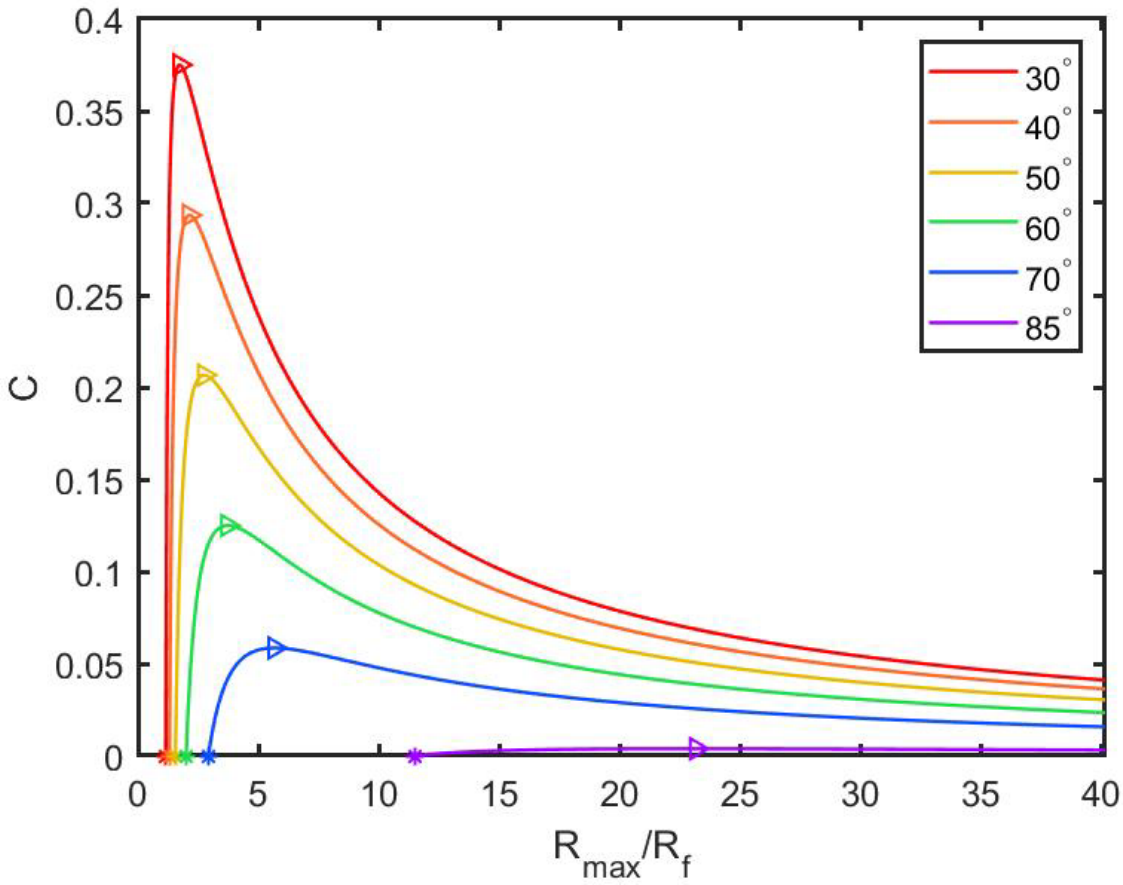

Fig. 2.6 Dependence of constant C on the ratio R_{max}/R_f at different contact angles. The hollow triangles label the maximum values of C. The asterisks correspond to the spherical droplets of radius $R_{max} = \frac{R_f}{\cos\theta}$ meeting the fiber surface at the given contact angle θ

As discussed earlier, the constant C fully specifies the shape of unduloid. For an unduloidal drop on fiber, this constant is fixed by R_{max} ,see Eq. (2.18). We, therefore, in position to investigate the dependence of C on R_{max} In Fig. 2.6, we plot C versus

dimensionless drop radius R_{max}/R_f at different contact angles. Owing to constraint (2.20), each curve has a unique beginning point $R_{max} = R_f/\cos\theta$, asterisked in Fig. 2.6.

Surprisingly, the plots show that C changes with the size of the unduloidal drop non-monotonously. Moreover, the maximum value of C is not necessarily ½. The hollow triangles in Fig. 2.6 label the maximum peaks on each curve. This non-monotonous dependence suggests that each C selects not a single unduloid but two different unduloids with different R_{max}. When R_{max} goes to infinity, C approaches zero as $C \approx \frac{2R_{max}R_f(R_{max})(R_{max}\cos\theta)}{(R_{max}^2)^2} = R_f\cos\theta\,/R_{max} \to 0$. Again, this constant $C = 0$ corresponds to the case when the unduloid turns into a sphere. Thus, we have two limiting spheres, one has a finite radius $\frac{R_f}{\cos\theta}$ and another has an infinite radius.

We further plot the dimensionless capillary pressure $\frac{\Delta P R_f}{\sigma}$ as a function of the ratio $\frac{R_{max}}{R_f}$, Fig 2.7(a). This dependence appears monotonous. Therefore, we can re-parametrize C as a function of dimensionless capillary pressure $\frac{\Delta P R_f}{\sigma}$. This dependence C ($\frac{\Delta P R_f}{\sigma}$) is shown in Fig 2.7(b). In both Fig. 2.7(a) and Fig. 2.7(b), the capillary pressure approaches zero when R_{max} goes to infinity. The non-monotonicity of constant C on the capillary pressure and on the maximum radius of unduloidal droplet calls for establishing a selection principle for the given unduloid as a possible model of a droplet resting on a fiber. We first analyze the maximum of C as a function of contact angle θ.

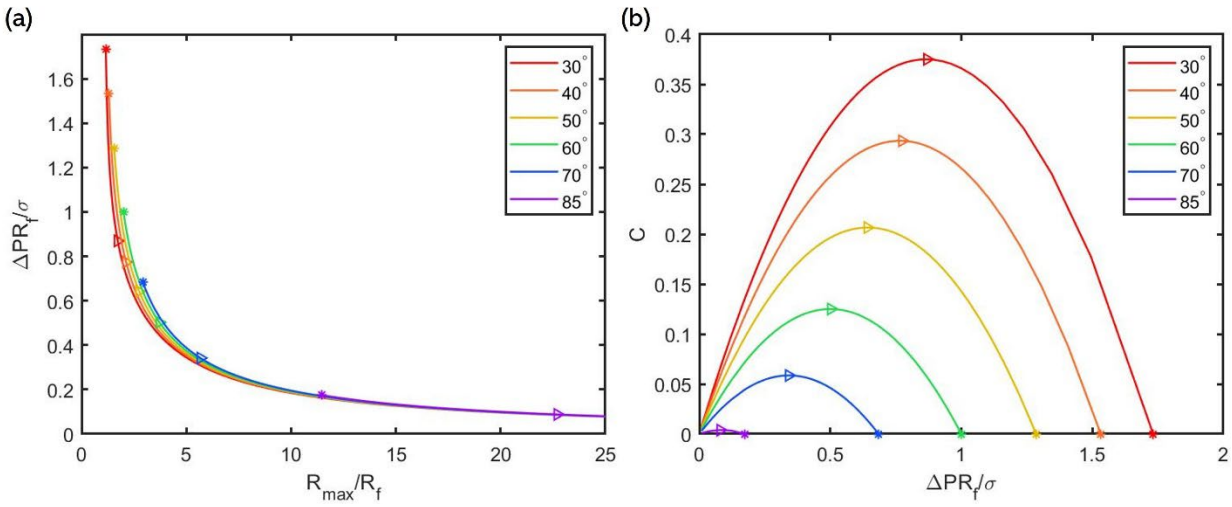

Fig. 2.7 (a) Dimensionless capillary pressure $\frac{\Delta PR_f}{\sigma}$ *versus dimensionless radius of unduloidal drop* $\frac{R_{max}}{R_f}$*.(b) Constant C versus dimensionless capillary pressure* $\frac{\Delta PR_f}{\sigma}$*. The contact angles are the same as in Fig 2.6. The hollow triangles correspond to the maximums of C-curves. The asterisks correspond to the spherical droplets with the radius* $R_{max} = \frac{R_f}{\cos\theta}$ *and capillary pressure* $\Delta P = 2\,\sigma\cos\theta / R_f$.

Taking the partial derivative of C, Eq. (2.18), with respect to R_{max}, we obtain

$$\frac{\partial C}{\partial R_{max}} = \frac{2R_f\left[\cos\theta\left(R_f^4 + 6R_f^2R_{max}^2 + R_{max}^4\right) - R_fR_{max}(\cos 2\theta + 3)\left(R_f^2 + R_{max}^2\right)\right]}{\left(R_f^2 - R_{max}^2\right)^3}$$

$$= 0,$$

Or

$$\cos\theta\,(1 + 6n^2 + n^4) - n(\cos 2\theta + 3)(1 + n^2) = 0,\ n = R_{max}/R_f. \tag{2.21}$$

Equation (2.21) has to be solved with constraints $0 < R_f < R_{max}$ & $0 < \theta < \frac{\pi}{2}$. To solve Eq. (2.21), we rewrite it as

$$\frac{1+6n^2+n^4}{n^2+1} \equiv \frac{2\cos^2\theta+2}{\cos\theta} \tag{2.21.1}$$

And further rearrange $(2.21.1)$ as

$$\frac{2n}{n^2+1}+\frac{n^2+1}{2n} \equiv \cos\theta + 1/\cos\theta \tag{2.21.2}$$

One observes that identifying

$$\cos\theta = \frac{2n}{n^2+1} \tag{2.21.3}$$

equation $(2.21.2)$ can be solved analytically. We note that the ratio n is always greater than 1, $n > 1$, therefore, $\frac{n^2+1}{2n} > 1$ and $\frac{n^2+1}{2n}$ could not be equal to $\frac{n^2+1}{2n} \neq \cos\theta$.

Rewriting $(2.21.3)$ in the form $(n-\sec\theta)^2 = \sec^2\theta - 1$, we solve the latter for n to obtain

$$n = \frac{1+\sin\theta}{\cos\theta}, or\ n = \frac{1-\sin\theta}{\cos\theta} \tag{2.21.4}$$

When $0 < \theta < \frac{\pi}{2}$, we have $0 < \frac{1-\sin\theta}{\cos\theta} < 1$ (see Fig. 2.8). Thus $n = \frac{1-\sin\theta}{\cos\theta}$ cannot be the solution to $(2.21.2)$.

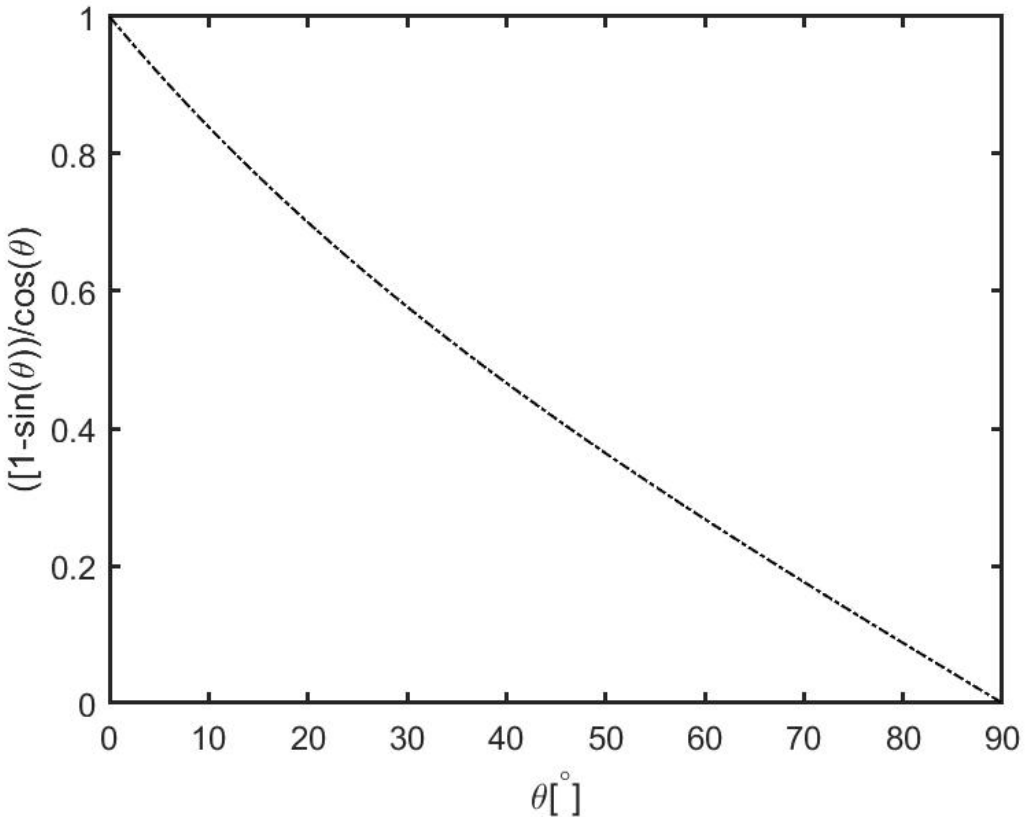

Fig. 2.8 The ratio $\frac{1-sin\,\theta}{cos\,\theta}$ varies from 1 to 0, when $0 < \theta < \frac{\pi}{2}$.

Therefore, we retrieve the only solution as:

$$n = \frac{1+\sin\theta}{\cos\theta} \Rightarrow R_{max} = \frac{R_f(1+\sin\theta)}{\cos\theta} \tag{2.22}$$

Substituting Eq. (2.22) back into Eq. (2.18), we have the relation between contact angle θ and the maximum value of C,

$$C_{max} = \frac{\cos^2\theta}{2}. \tag{2.23}$$

The relations expressed by Eq. (2.22) and Eq. (2.23) are plotted in Fig. 2.9 and Fig. 2.5, respectively.

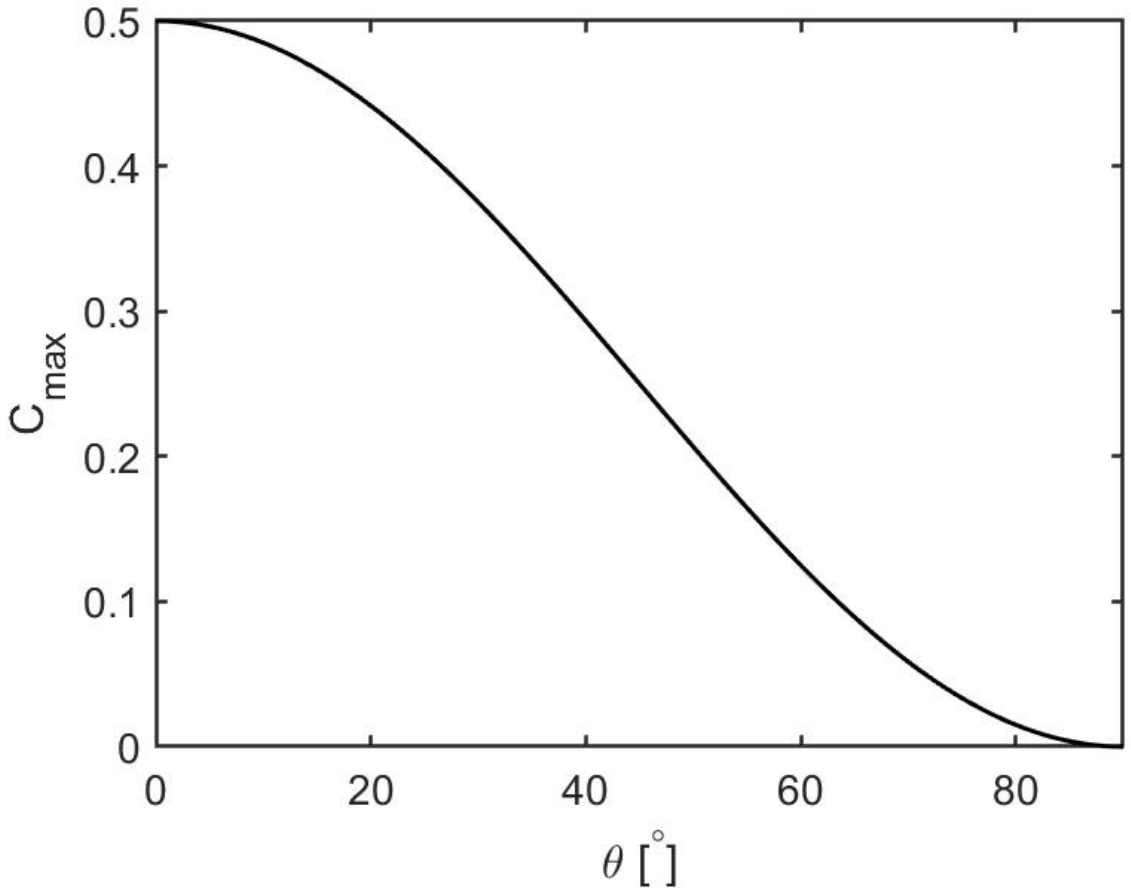

Fig. 2.9 Maximum C as a function of contact angle.

We notice that Eq. (2.22) specifies the radius of unduloidal drop having the contact angle with the fiber equal to the inflection angle of an unduloid[33, 34]. In other words, when $C = C_{max}$, the fiber radius R_f and the radius R_{inf} of the parallel corresponding to the point where the curvature of the generator changes its sign coincide. Carrol

conjectured that when $R_f = R_{inf}$ an unduloidal drop should be unstable and would turn in a clamshell[35]. The relation between R_{inf} and θ was later corrected by McHale[36].

2.3.3 Profile and volume of unduloidal drop

To find the unduloid profile, we rewrite Eq. (2.6) in the form

$$\frac{dy}{dx} = \cot\gamma \Rightarrow \frac{dx}{dy} = \tan\gamma = -\sin\gamma\,(1-\sin^2\gamma)^{-\frac{1}{2}} \tag{2.24}$$

Using the first integral, $sin\,\gamma = \frac{\Delta P}{2\sigma}\mathrm{y} + \frac{C\sigma}{\Delta P}\frac{1}{y}$, we then have

$$\frac{dx}{dy} = -\left(\frac{\Delta P}{2\sigma}y + \frac{C}{\sigma}\cdot\frac{1}{y}\right)\left[1-\left(\left(\frac{\Delta P}{2\sigma}y + \frac{C}{\sigma}\cdot\frac{1}{y}\right)\right)^2\right]^{-\frac{1}{2}} \tag{2.25}$$

where C is obtained from Eq. (2.18) and ΔP is obtained from Eq. (2.16). The differential equation (2.25) can be numerically integrated from R_f to R_{max} using MATLAB ODE45.

Hence, we can use MATLAB to integrate the function $x(y)$ of the unduloid and get its volume.

$$V = \int_{x_{left}}^{x_{right}} \pi y^2 dx = 2\pi \int_{R_f}^{R_{max}} y^2 \frac{dx}{dy} dy - 2\pi R_f^2\left(x_{right} - x_{left}\right) \tag{2.26}$$

where x_{left} and x_{right} are positions of the left and right contact lines.

Thus, varying the drop size R_{max} from $\frac{R_f}{\cos\theta}$ to infinity, we can calculate the volume of unduloidal drop at any specific contact angle θ. Figure 2.10 shows how the volume of an unduloidal drop grows on a fiber with different contact angles. Again, the hollow triangles

label the points where C reaches its maximum peak value, and the asterisks correspond to the spherical drop forming the given contact angle with the fiber.

To generate the curves with constant volume, we use an iterative algorithm as follows. Assume that one has a drop with the dimensionless volume of $V_0^{\frac{1}{3}}/R_f = 10$, $\frac{R_{max}}{R_f} = 5.93$ and the contact angle of $30°$, as marked as the red dot in Fig. 2.11(a). Now we need to find another drop with the same volume but a contact angle of $40°$ on the same fiber. By changing R_{max}/R_f near 5.93, we can calculate the dimensionless volume V at each value of R_{max}/R_f. Figure 2.11(b) plots the difference $|V - V_0|$ as a function of R_{max}/R_f. The minimum value $|V - V_0| = 0$ is achieved when $\frac{R_{max}}{R_f} = 5.98$. This is the needed R_{max}/R_f for the drop making contact angle of $40°$ with the fiber. Following this algorithm, we numerically obtained a series of unduloids of fixed volume with different contact angles in Fig. 2.12. As we see in the zoom-in figure of Fig. 2.13 and Fig. 2.14(a), the drop making contact angle of $85°$ with the fiber does not exist at this specific volume.

Combining Fig. 2.10 and Fig. 2.7(a), we found the relation between the capillary pressure and unduloid volume, which is plotted in Fig. 2.13. The smallest unduloid is a spherical drop (see asterisks in Fig. 2.13), which has a maximum capillary pressure $2\sigma \cos\theta \, /R_f$. The capillary pressure decreases monotonically with the increase of drop size.

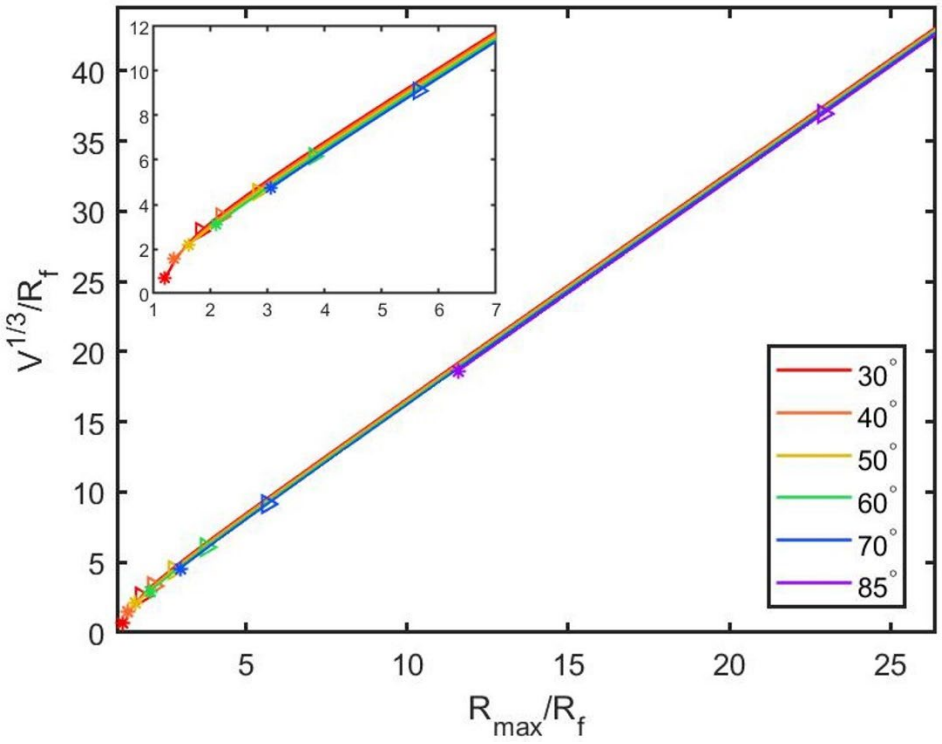

Fig. 2.10 The dimensionless unduloid volume is plotted as a function of dimensionless unduloid size.

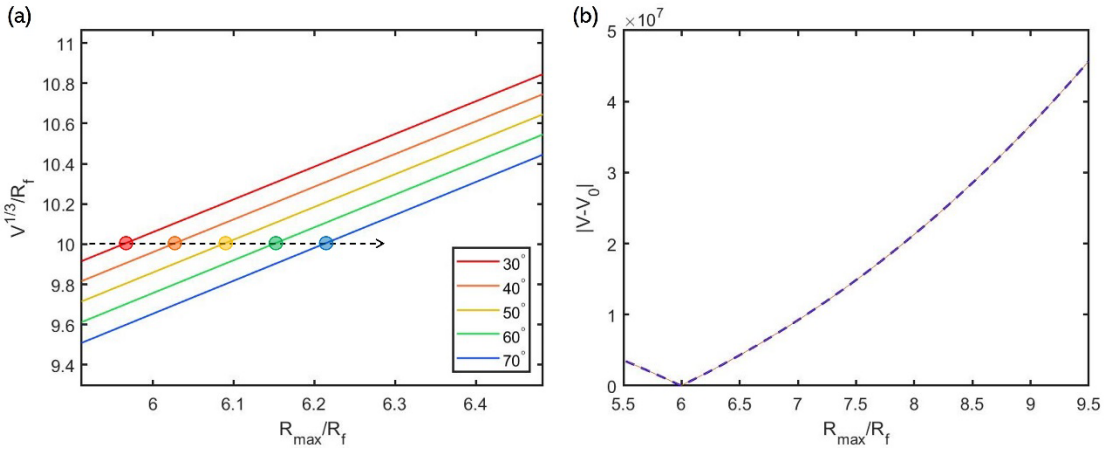

Fig. 2.11 (a) The Schematic shows how we numerically find the different unduloids having constant volume. As shown in the figure, the arrow won't cross the $85°$ *curve,*

meaning that the drop making contact angle of 85 degrees with the fiber does not exist at this specific volume. (b) At $CA = 40°$, $|V - V_0|$ *has a minimum value when* $\frac{R_{max}}{R_f} = 5.98$.

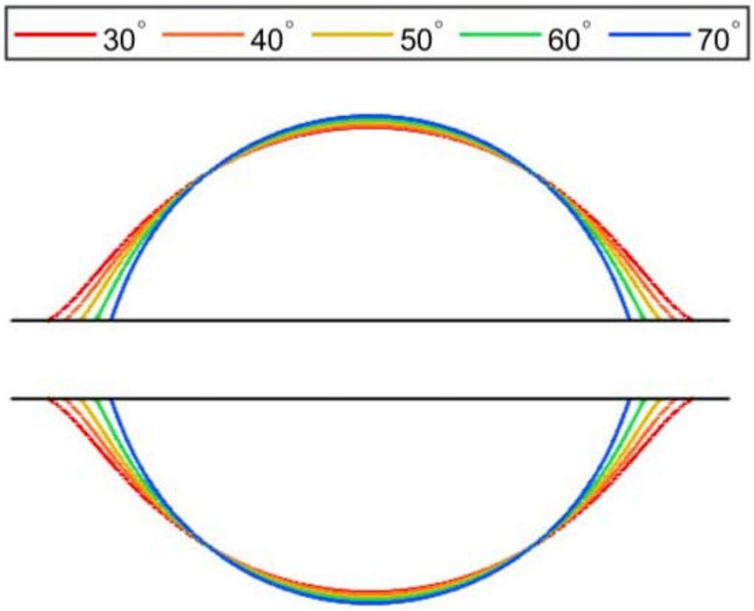

Fig. 2.12 Unduloidal droplets of constant volume making different contact angles with the fiber. The unduloid of volume V_0 *making* $85°$ *with the fiber doesn't exist.*

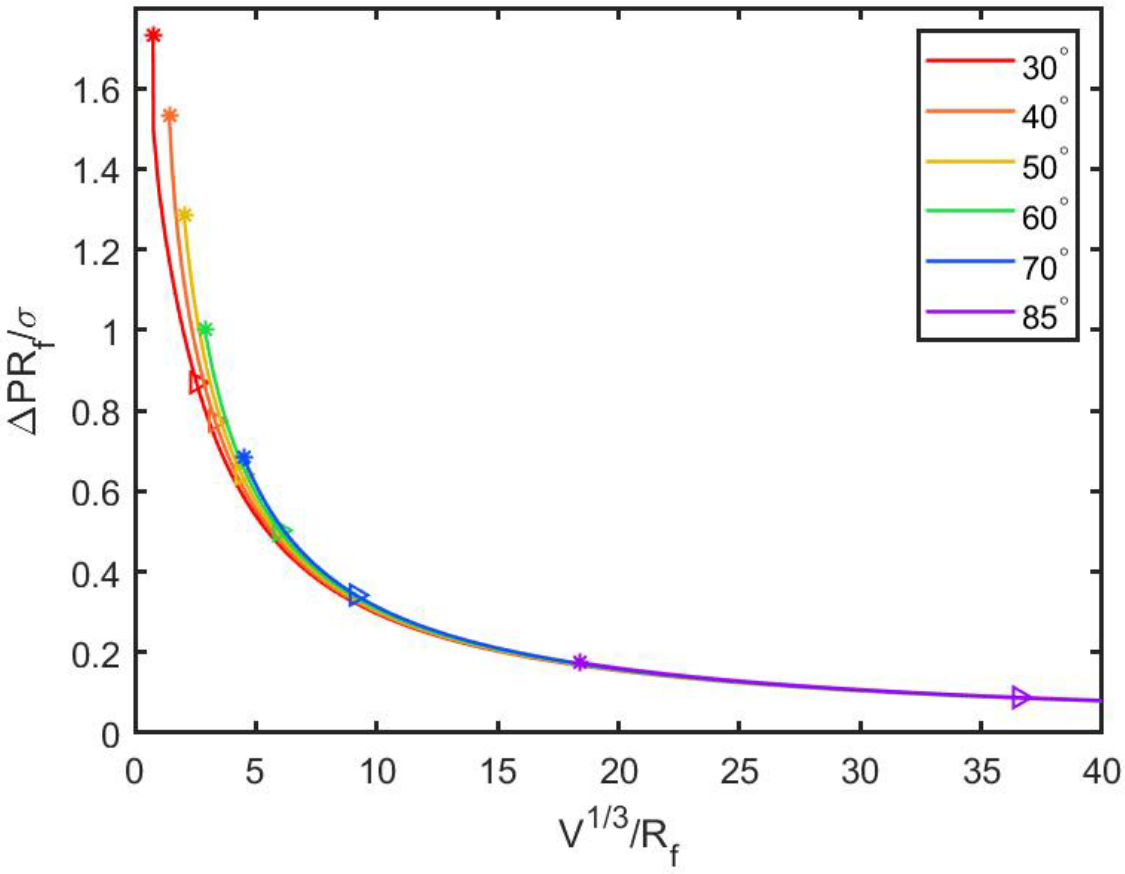

Fig. 2.13 Dimensionless capillary pressure versus dimensionless drop volume

2.4 Nodoidal droplets

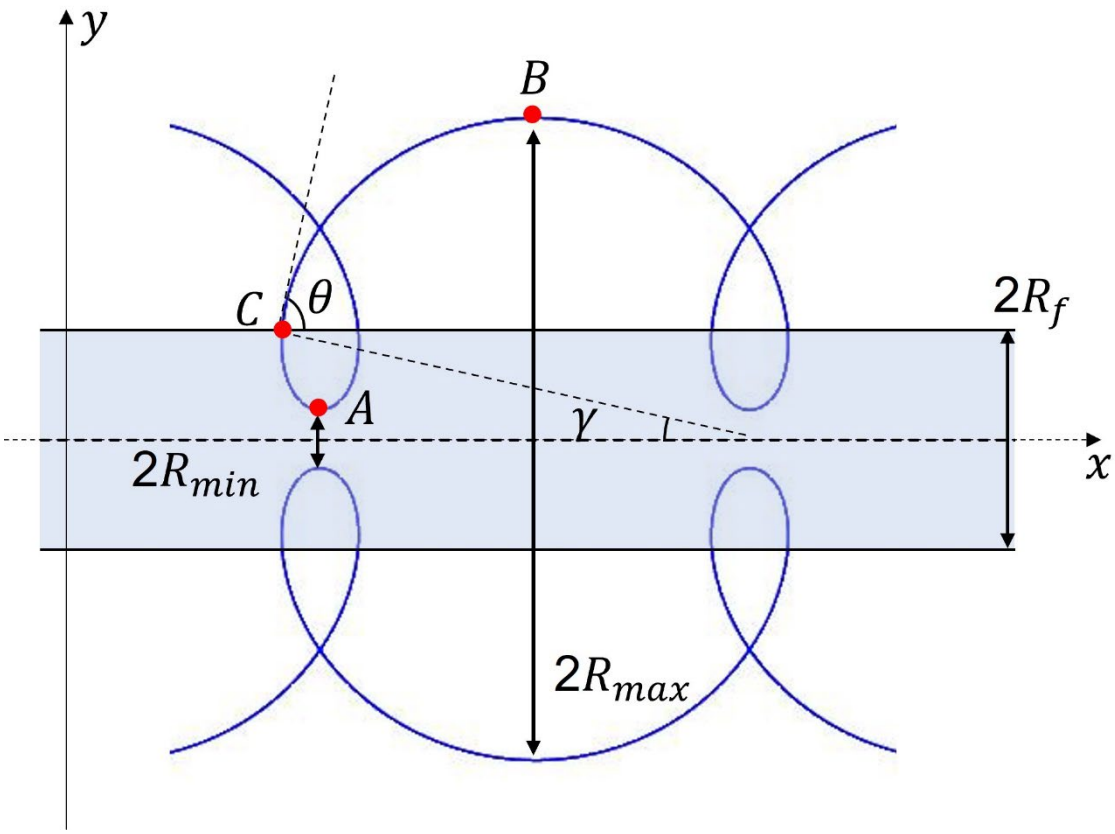

Fig. 2.14 Schematic of a nodoidal drop wrapping up a fiber

Consider a nodoidal drop sitting on a fiber with radius R_f. The drop forms a contact angle θ with the fiber surface, Fig. 2.14.

At the neck of the nodoid (point A in Fig. 2.14), we have $\gamma = -\frac{\pi}{2}$ and $y = R_{min}$. Therefore, Eq. (2.10) is written as

$$-R_{min} = \frac{\Delta P}{2\sigma} R_{min}^2 + \frac{\sigma}{\Delta P} C. \tag{2.27}$$

At the bulge of the nodoid (point B in Fig. 2.14), we have $\gamma = \frac{\pi}{2}$ and $y = R_{max}$. Then,

$$R_{max} = \frac{\Delta P}{2\sigma} R_{max}^2 + \frac{\sigma}{\Delta P} C. \tag{2.28}$$

Solving these two equations $(2.27) - (2.28)$ for the pressure drop ΔP and C separately, we immediately obtain

$$\Delta P = \frac{2\sigma}{R_{max} - R_{min}}. \tag{2.29}$$

$$C = -\frac{2R_{max}\, R_{min}}{(R_{max} - R_{min})^2}. \tag{2.30}$$

Comparing (2.13) with (2.29), we observe that the unduloidal drop of radius R_{max} will always have smaller capillary pressure relative to that of a nodoidal drop of the same R_{max}.

2.4.1 Parameters of nodoidal drop on a fiber

To specify the nodoidal droplet, we need to relate R_{min} with the fiber radius and droplet contact angle θ. At the contact line between nodoidal drop and the fiber (point C in Fig. 2.14), we have $\gamma = \frac{\pi}{2} - \theta$ at $y = R_f$. Therefore,

$$R_f \sin\left(\frac{\pi}{2} - \theta\right) = \frac{\Delta P}{2\sigma} R_f^2 + \frac{\sigma}{\Delta P} C. \tag{2.31}$$

Using (2.28) to eliminate C, we obtain from (2.31):

$$\Delta P = 2\sigma \frac{R_{max} - R_f \cos\theta}{R_{\max}^2 - R_f^2} \tag{2.32}$$

Then, using the pair of equations (2.27) and (2.31) to eliminate C, and eq. (2.32) to express ΔP via R_{max}, we find

$$R_{\min} = \frac{R_f(R_{max}\cos\theta - R_f)}{R_f \cos\theta - R_{max}} \tag{2.33}$$

Similarly, C can be found as,

$$C = \frac{R_{max}R_f\left(R_f\cos\theta - R_{max}\right)\left(R_f - R_{max}\cos\theta\right)}{\left(R_f^2 - R_{max}^2\right)^2} \tag{2.34}$$

2.4.2 Parametric analysis of the nodoidal solutions

In order to ensure the existence of a nodoidal drop on fiber, we have to satisfy the following conditions: 1) The neck radius of the nodoid must be positive and smaller than the fiber radius. 2) The bulge of nodoid must be above the surface of the fiber. 3) The contact angle θ is allowed to change from 0° degrees to 180°, $-1 \le \cos\theta \le 1$.

For the inequality $R_{\min} = \frac{R_f(R_{max}\cos\theta - R_f)}{R_f\cos\theta - R_{max}} \ge 0$ to hold true within the constraints $R_f < R_{max}$ & $0 \le \theta \le 90°$ ($0 \le \cos\theta \le 1$), we have to have

$R_{max}\cos\theta - R_f \ge 0$; $R_f\cos\theta - R_{max} \ge 0$ or (2.33.1)

$R_{max}\cos\theta - R_f \le 0$; $R_f\cos\theta - R_{max} \le 0$. (2.33.2)

From the first inequality (2.33.1) we have $R_{max} \ge R_f/\cos\theta$ and from the second inequality, we infer incorrect inequality $R_f\cos\theta \ge R_{max} \ge R_f/\cos\theta$. Therefore, the first set of inequalities (2.33.1) cannot be satisfied for $0 \le \cos\theta \le 1$.

For the second set of inequalities (2.33.2), from the first part, we have: $R_{max} \le R_f/\cos\theta$. Then, substituting this upper estimate of R_{max} in the second inequality (2.33.2), we find $R_f\cos\theta \le R_{max} \le R_f/\cos\theta$. This last inequality is true indeed: $1/\cos^2\theta \ge 1$. Thus, we arrive at the upper estimate for the maximum radius of nodoidal drop as

$$R_f < R_{max} \leq \frac{R_f}{\cos\theta} \tag{2.35}$$

Then, we investigate the inequality $R_{\min} = \frac{R_f(R_{max}\cos\theta - R_f)}{R_f\cos\theta - R_{max}} \geq 0$ with constraints $R_f < R_{max}$& $90° \leq \theta \leq 180°(-1 \leq \cos\theta \leq 0)$. When the contact angle is larger than $90°$, $90° < \theta \leq 180°$ $(-1 \leq \cos\theta < 0)$, both numerator and denominator in the ratio $\frac{(R_{max}\cos\theta - R_f)}{R_f\cos\theta - R_{max}}$are negative. Therefore, the inequality $R_{\min} = \frac{R_f(R_{max}\cos\theta - R_f)}{R_f\cos\theta - R_{max}} \geq 0$ holds true for any R_{max}.

Hence, for the given contact angle θ that varies from $0°$ to $90°$ degrees, we can only find a nodoidal drop with the maximum radius within the range of $R_f < R_{max} \leq \frac{R_f}{\cos\theta}$. For contact angles within the range $90° < \theta \leq 180°$, we can always have a nodoidal drop with any R_{max}.

Due to the discovery of the turning point of C for unduloids, we question whether a similar peak exists in the nodoid case.

Taking the partial derivative of C , Eq. (2.34), with respect to R_{max}, we obtain

$$\frac{\partial C}{\partial R_{max}} = \frac{R_f\left[cos\,\theta\left(R_f^4 + 6R_f^2R_{max}^2 + R_{max}^4\right) - R_fR_{max}(cos\,2\theta + 3)\left(R_f^2 + R_{max}^2\right)\right]}{\left(R_f^2 - R_{max}^2\right)^3}$$

$$= 0,$$

Or

$$cos\,\theta\,(1 + 6n^2 + n^4) - n(cos\,2\theta + 3)(1 + n^2) = 0, n = R_{max}/R_f. \tag{2.36}$$

Equation (2.36) is exactly the same as Eq. (2.21). When $0 < \theta < \frac{\pi}{2}$, $R_f < R_{max}$, there is only one inflection point at $R_{max} = \frac{R_f(1+\sin\theta)}{\cos\theta}$. On the other side, when $0 < \theta < \frac{\pi}{2}$, $R_{max} = \frac{R_f}{\cos\theta}$ is always smaller than $R_{max} = \frac{R_f(1+\sin\theta)}{\cos\theta}$ therefore, no solution of Eq. (2.36) exists for nodoids. We can safely conclude that within the range of $R_f < R_{max} \leq \frac{R_f}{\cos\theta}$, and $0 < \theta < \frac{\pi}{2}$, the constant C increases monotonically with R_{max}. According to Eq. (2.21.4), when $\frac{\pi}{2} < \theta < \pi$ & $n > 1$, there is no solution to satisfy Eq. (2.36). Thus, within the whole range of contact angles, $0 < \theta < \pi$ the constant C is a monotonous function reaching its maximum value $C = 0$ corresponding to a spherical drop of radius $R_{max} = \frac{R_f}{|\cos\theta|}$, asterisked in Fig 2.15.

Figure 2.16 shows that the dimensionless capillary pressure of nodoidal drop $\frac{\Delta P R_f}{\sigma}$ decreases monotonously from infinity to $2\cos\theta$ when R_{max} increases from R_f to $\frac{R_f}{\cos\theta}$.

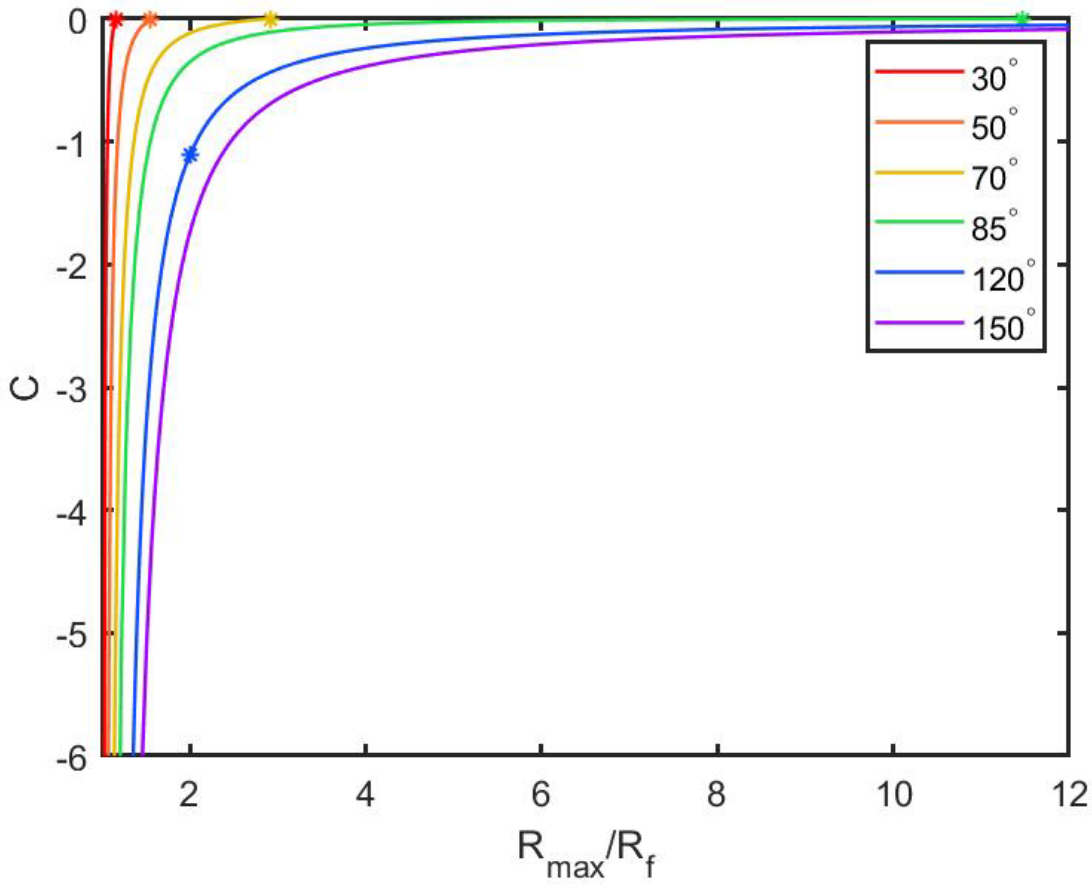

Fig. 2.15 C versus dimensionless nodoidal drop size R_{max}/R_f at different contact angles. The asterisks correspond to the spherical droplets with radius $R_{max} = \frac{R_f}{\cos\theta}$ and $C = 0$. The asterisk corresponding to the spherical drop for the purple curve of $CA = 150°$ is out of the range ($C < -6$).

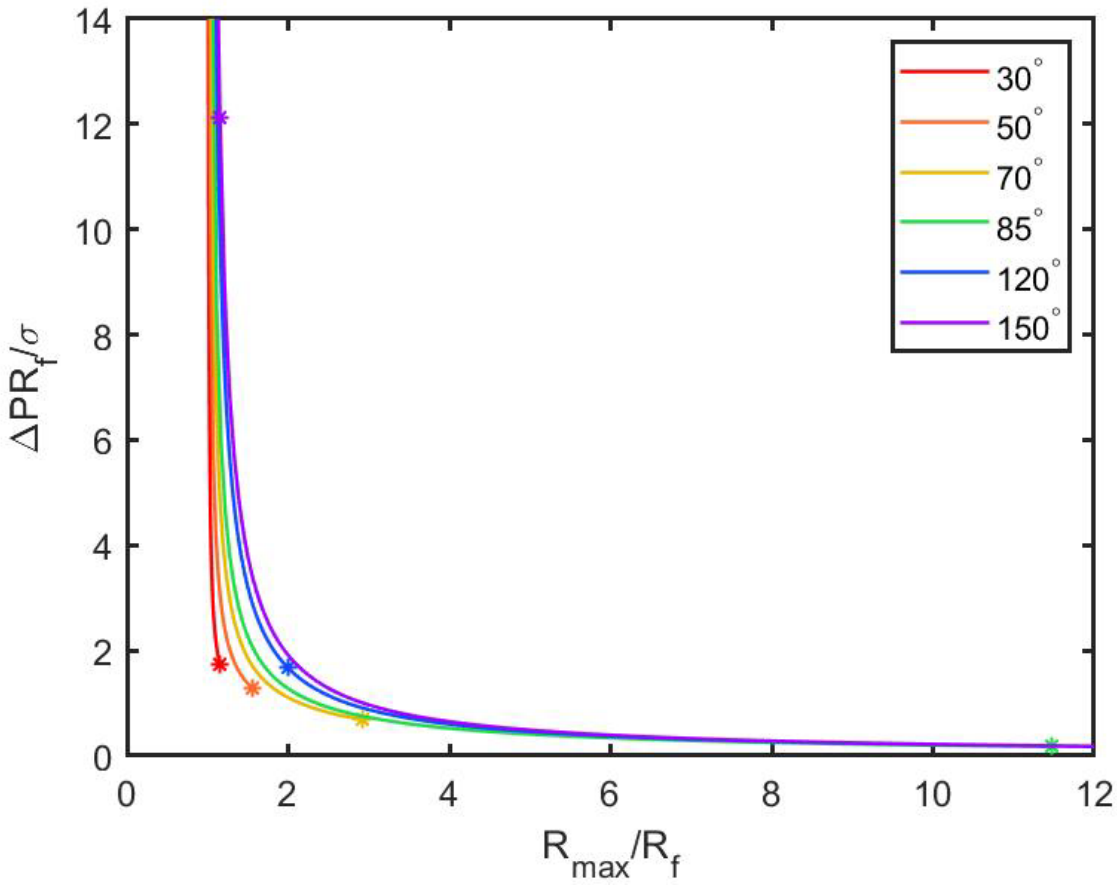

Fig. 2.16 Dimensionless capillary pressure $\frac{\Delta P R_f}{\sigma}$ versus dimensionless radius of nodoidal drop $\frac{R_{max}}{R_f}$. The asterisks correspond to the spherical droplets with $R_{max} = \left|\frac{R_f}{\cos\theta}\right|$. Notice that though the ratio $\left|\frac{R_f}{\cos\theta}\right|$ for $\theta = 30°$ and $150°$ is the same, the capillary pressure $\Delta P = 2\sigma \frac{R_{max} - R_f \cos\theta}{R_{max}^2 - R_f^2}$ is different because of the different signs of cosine.

2.4.3 Nodoid profile and its volume

The nodoid function $x(y)$ can be found in the same way as the unduloid using MATLAB ODE45. Then the volume can be calculated as well.

Substituting C in the expression of Eq. (2.34) and ΔP in the expression of Eq. (2.32) into the differential equation (2.25), the nodoid function $x(y)$ can be obtained by integrating from R_f to R_{max} using MATLAB ODE45, and the volume of nodoidal drop can be calculated by Eq. (2.26).

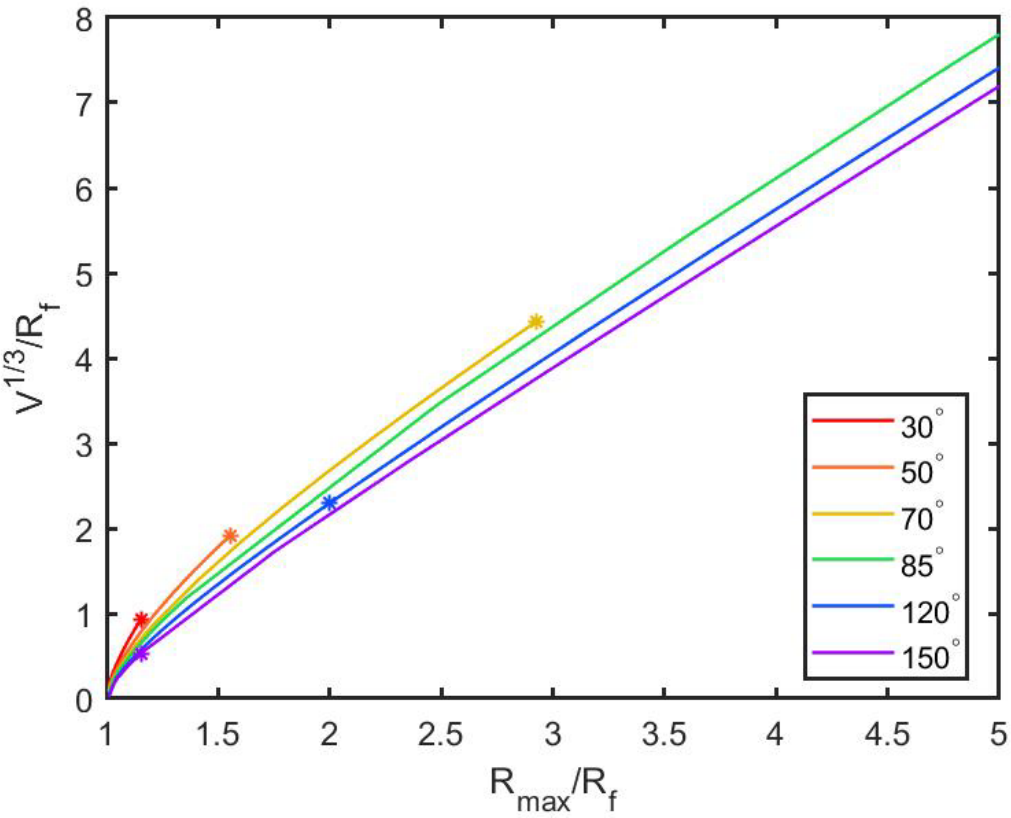

Fig. 2.17 The dimensionless nodoid volume is plotted as a function of dimensionless nodoid size. The asterisks correspond to the spherical droplets with $R_{max} = \left|\frac{R_f}{\cos\theta}\right|$ *. The asterisk corresponding to the dimensionless volume of the spherical drop having* $CA = 85°$ *is out of the range (*$\frac{V^{\frac{1}{3}}}{R_f} > 8$*).*

Figure 2.17 shows how the volume of a nodoidal drop grows on a fiber with different contact angles. The asterisks correspond to the spherical drop forming the given contact angle with the fiber.

Using the same iterative algorithm described in **Chapter 2.3.3**, one can generate the profiles of series of nodoidal drops with constant volume making different contact angles with the fiber.

Assume that one has a drop with the dimensionless volume of $V_0^{\frac{1}{3}}/R_f = 3, \frac{R_{max}}{R_f} = 2.16$ and the contact angle of 70 degrees on the fiber, as marked as the yellow dot in Fig. 2.18. By changing R_{max}/R_f near 2.16, we can calculate the dimensionless volume V at each value of R_{max}/R_f for given contact angles searching for the minimum value $|V - V_0| = 0$. Following this algorithm, we numerically obtained a series of nodoids of fixed volume with different contact angles in Fig. 2.19. As shown in Fig. 2.18, the droplets making contact angle of 30 or 50 degrees with the fiber do not exist at this specific volume. The dashed line in Fig. 2.19 is the limiting spherical nodoidal drop existing on the fiber at this volume, which can be numerically determined by searching for different $\frac{R_f}{\cos\theta}$. When $\theta = 61.75°$, the corresponding dimensionless volume is equal to 3.

Similarly, if one draws a vertical line at $\frac{R_{max}}{R_f} = 2.5$, we can find a series of nodoidal drops having the same R_{max} but different contact angles with the fiber, shown as the dashed curves in Fig. 2.20. For 30 degrees and 50 degrees, only unduloidal drops can be found, which are plotted as the solid curves.

Combining Fig. 2.18 and Fig. 2.19, we found the relation between the capillary pressure and nodoid volume, which is plotted in Fig. 2.21. The asterisks correspond to the spherical droplets with $R_{max} = \left|\frac{R_f}{cos\,\theta}\right|$, which has a capillary pressure $\Delta P = \begin{cases} \frac{2\sigma\, cos\,\theta}{R_f}(0° < \theta < 90°) \\ 2\sigma\frac{R_{max} - R_f \cos\theta}{R_{\max}^2 - R_f^2}(90° < \theta < 180°) \end{cases}$. The capillary pressure decreases monotonously with the drop size.

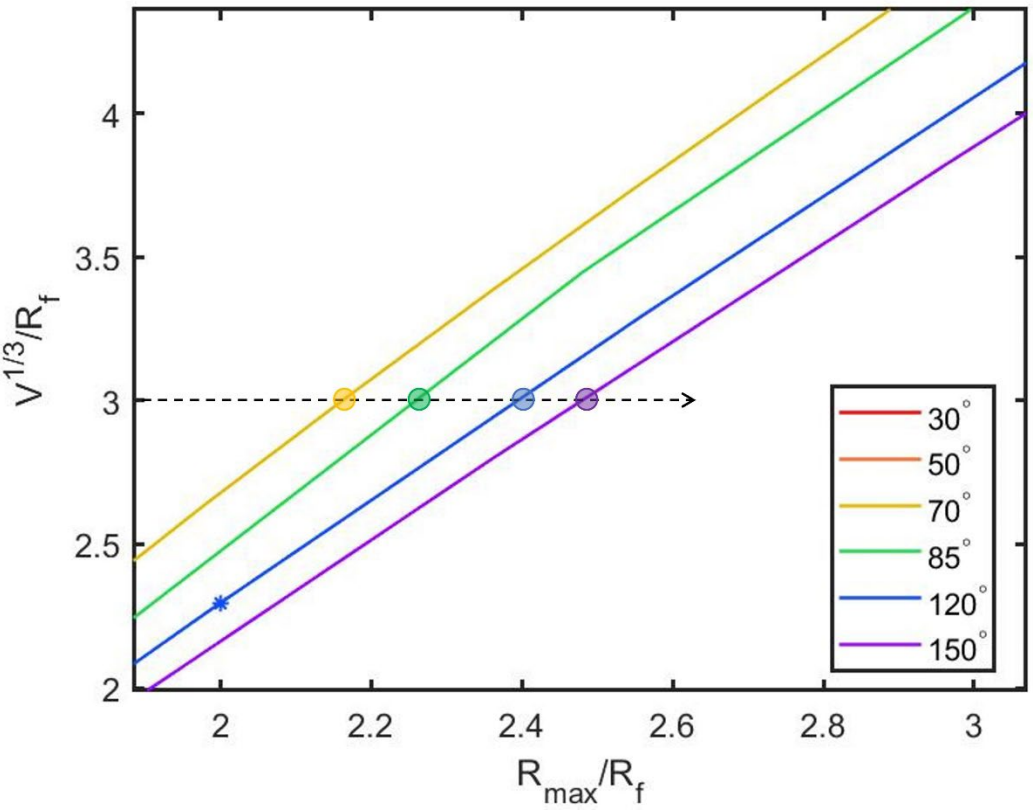

Fig. 2.18 The arrow won't cross the $30°$ and $50°$ curves, meaning that the drops making contact angle of 30 or 50 degrees with the fiber do not exist at this specific volume $V_0^{\frac{1}{3}}/R_f$.

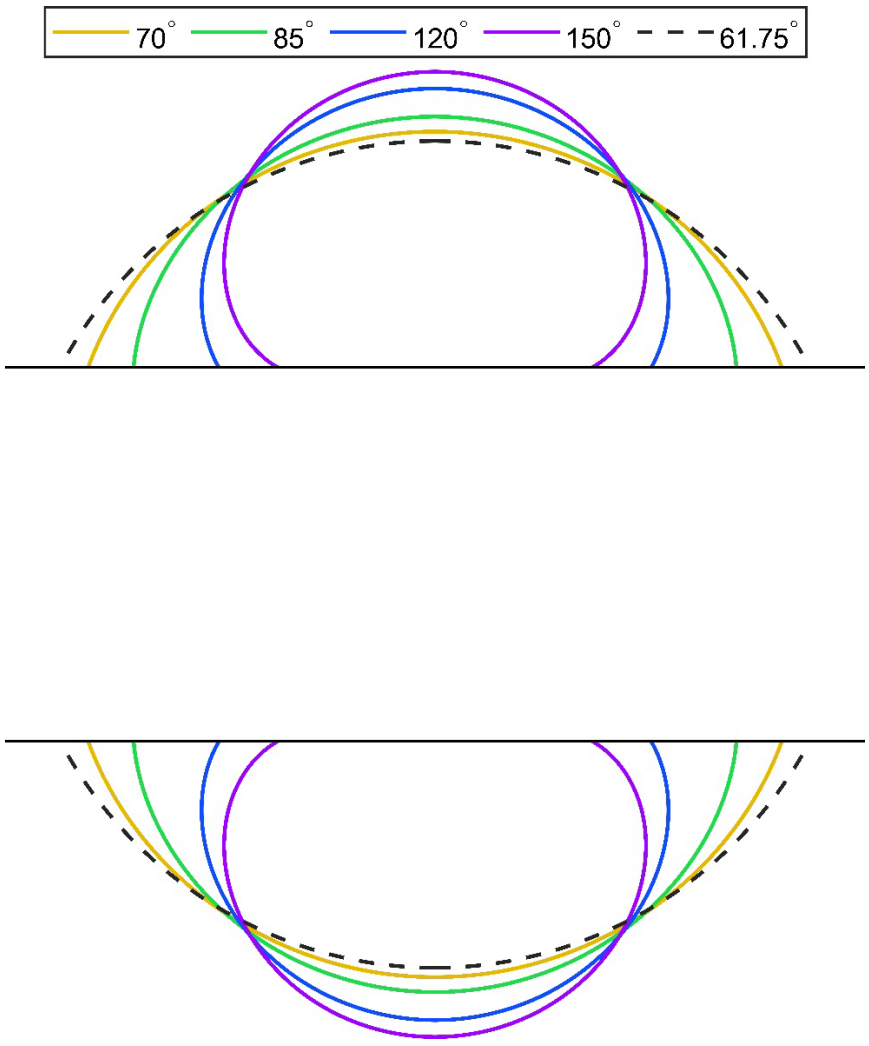

Fig. 2.19 Nodoidal droplets of constant volume making different contact angles with the fiber. The nodoids of volume V_0 making $30°$ or $50°$ with the fiber do not exist. The black dashed line shows the nodoidal drop having the smallest contact angle $61.75°$ of the same volume.

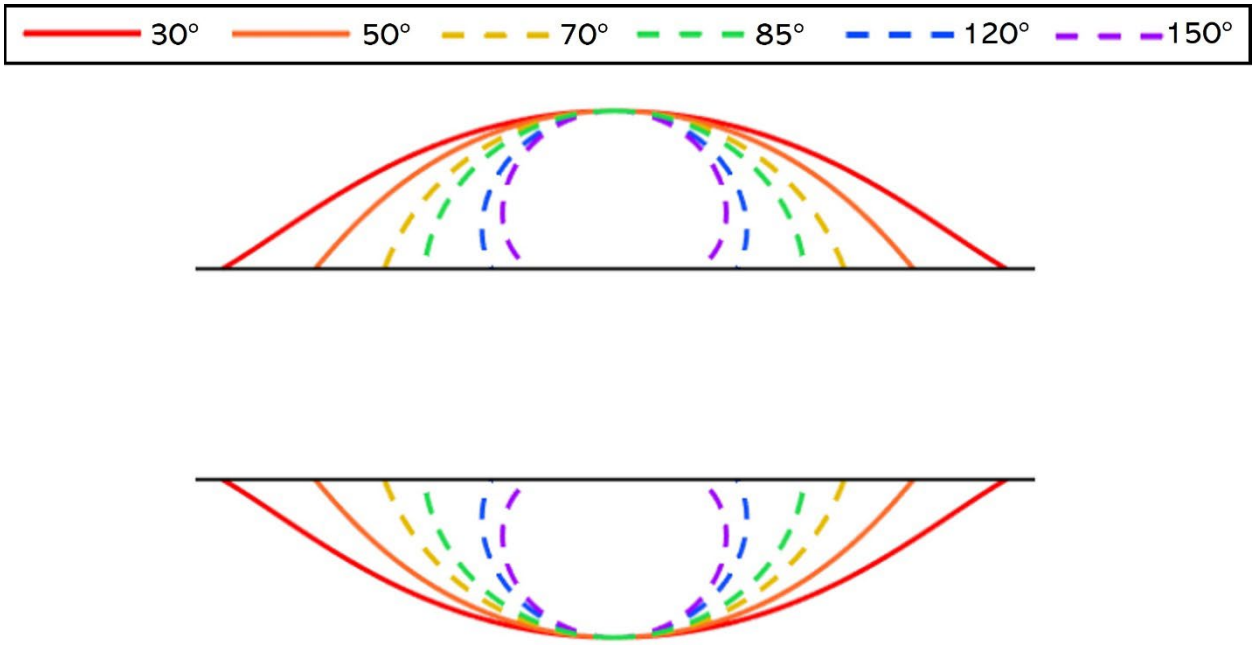

Fig. 2.20 The dashed curves show nodoidal droplets of constant R_{max}/R_f making different contact angles with the fiber. The solid curves show the unduloidal drops of the same dimensionless radius making $30°$ and $50°$ degrees contact angle with the fiber, when nodoids do not exist.

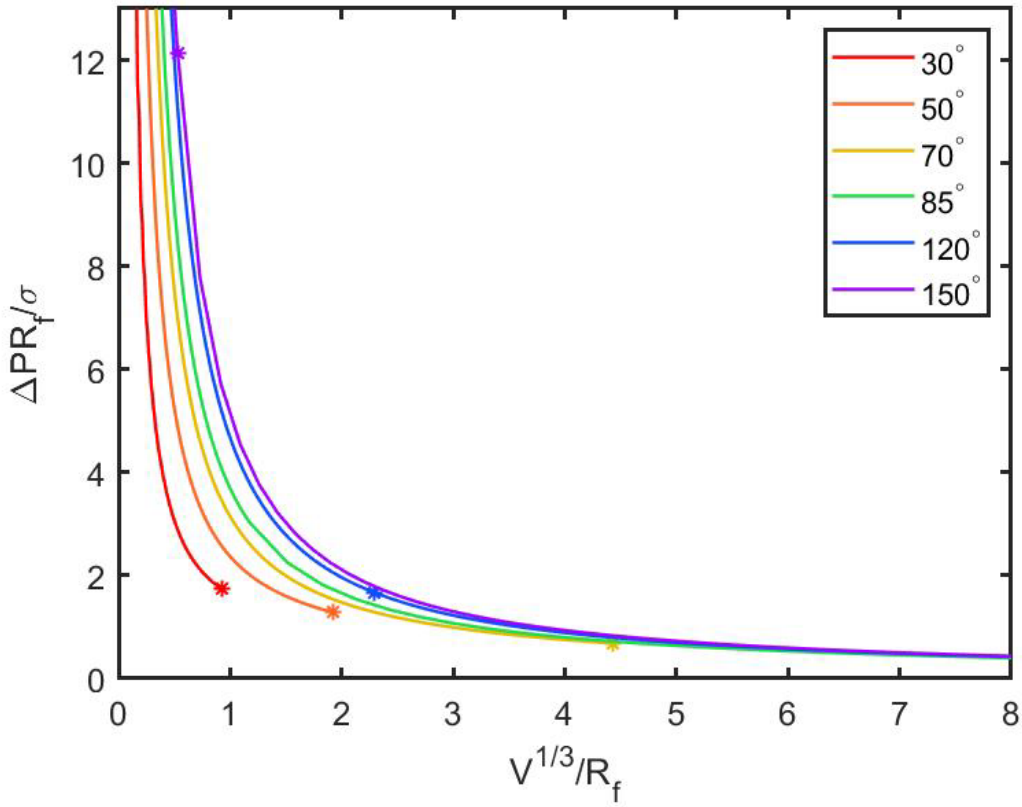

Fig. 2.21 Dimensionless capillary pressure $\frac{\Delta P R_f}{\sigma}$ *versus dimensionless volume* $V^{\frac{1}{3}}/R_f$. *The asterisks correspond to the spherical droplets with* $R_{max} = \left|\frac{R_f}{\cos\theta}\right|$ *and capillary pressure* $\Delta P = \frac{2\sigma\,|\cos\theta|}{R_f}$. *The asterisk corresponding to the dimensionless volume of the spherical drop having* $CA = 85°$ *is out of the range (*$\frac{V^{\frac{1}{3}}}{R_f} > 8$*).*

2.5 Transition between unduloids and nodoids

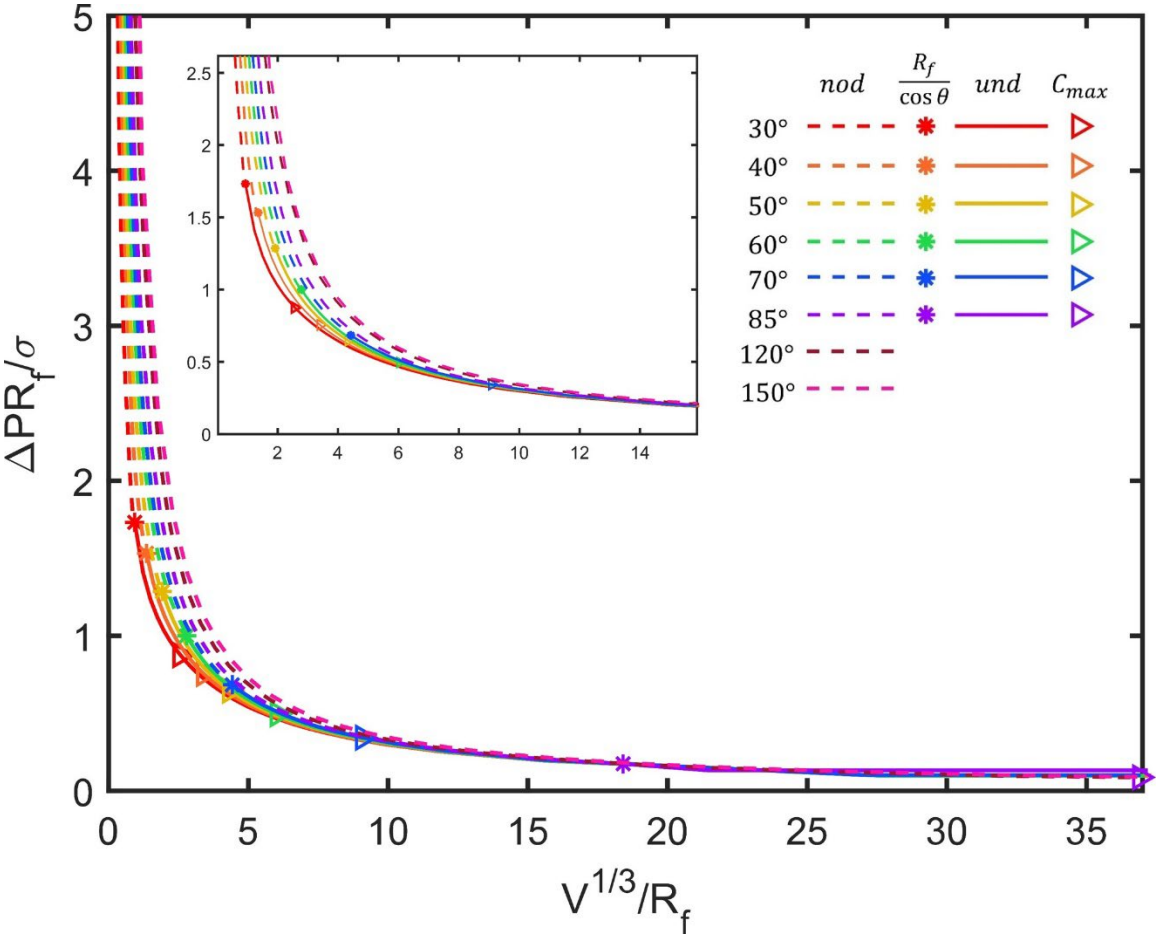

Fig. 2.22 Dimensionless capillary pressure $\frac{\Delta PR_f}{\sigma}$ of unduloids and nodoids versus dimensionless volume $V^{\frac{1}{3}}/R_f$.

Figure 2.22 shows relations between the dimensionless capillary pressure of unduloids and nodoids and their dimensionless drop volume at given contact angles. Each color of the symbols corresponds to a specific contact angle. The solid curves represent the unduloid cases, with two markers indicating two limiting cases. The asterisks point

out the limiting case of spherical drops with $R_{max} = R_f / \cos\theta$, and the hollow triangles correspond to the point when the unduloid has a maximum value of C. The dashed lines represent the nodoidal droplets. As expected, the unduloid and nodoid curves are connected by their shared spherical drop with radius $R_{max} = R_f / \cos\theta$. Besides, the capillary pressure of nodoids is always larger than that of the unduloids. The continuity of curves of unduloids and nodoids in Fig. 2.22 indicates that a nodoidal drop can transit to a unduloidal drop spontaneously with the increase of its volume. To confirm our guess, we further analyze the surface energy of unduloids and nodoids.

The surface energy of a drop on the fiber, W, includes two parts: 1) interfacial energy between drop and surrounding fluid, $W_1 = \sigma A_{drop}$ where A_{drop} is the surface area of the drop. 2)work of adhesion between drop and fiber, $W_2 = \sigma(1 + \cos\theta)A_{fiber}$, where A_{fiber} is the wetting area of the fiber.

Since we can obtain the profile of unduloid or nodoid $x(y)$ by numerically solving the differential equation (2.25), the surface area of A_{drop} can be determined by integrating the following equations,

$$A_{drop} = 4\pi \int_{R_f}^{R_{max}} y \frac{ds}{dy} dy \tag{2.37}$$

The wet area of the fiber can be calculated by multiplying the length of wet fiber by the perimeter of the fiber cross-section. The wetting length is known after the integration of Eq. (2.25), which equals to $L = 2(x_1 - x_0)$ where $x = \begin{cases} x_0(y = R_f) \\ x_1(y = R_{max}) \end{cases}$.

Hence,

$$A_{fiber} = 2\pi R_f L \tag{2.38}$$

Finally,

$$W = W_1 + W_2 = 4\sigma\pi \int_{R_f}^{R_{max}} y\frac{ds}{dy}dy + 2\sigma\pi R_f L(1+\cos\theta) \tag{2.39}$$

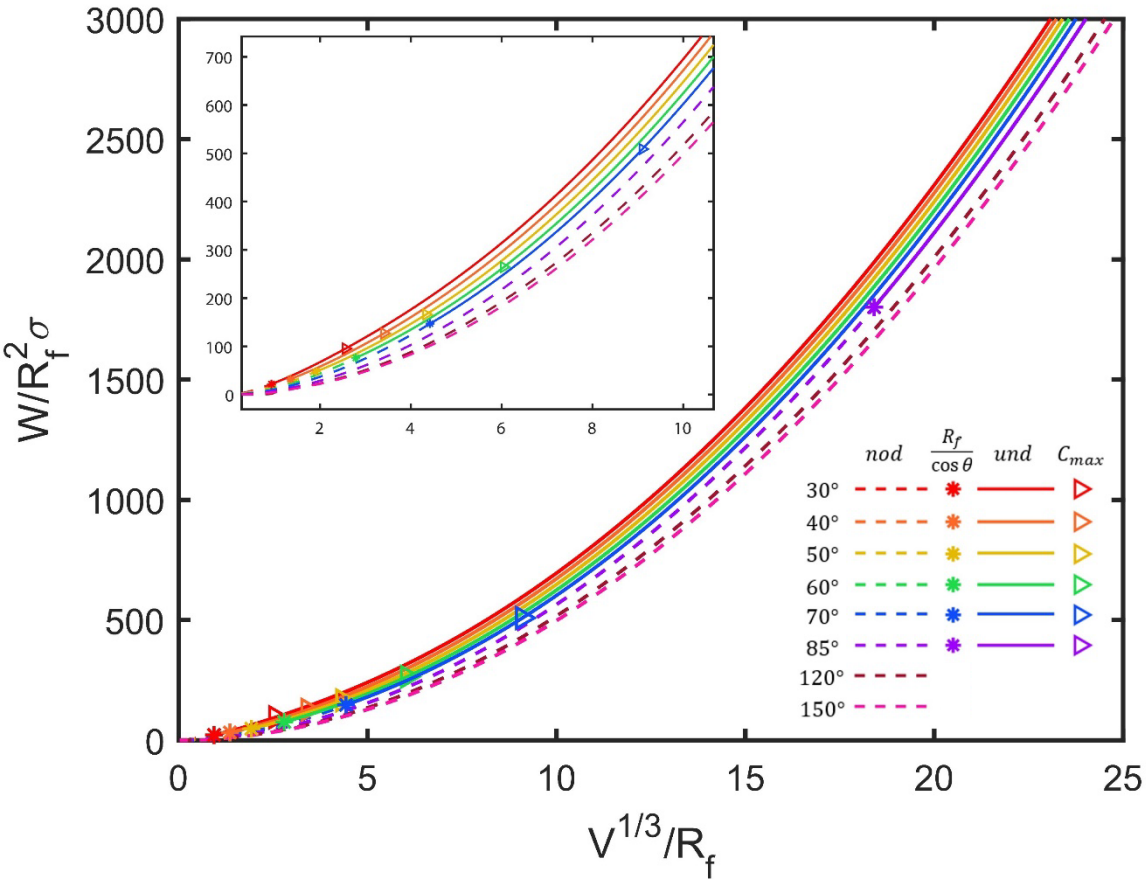

Fig. 2.23 Dimensionless surface energy $\frac{W}{R_f^2\sigma}$ of unduloids and nodoids versus dimensionless volume $V^{\frac{1}{3}}/R_f$.

In Fig. 2.23, we plot the dimensionless surface energy $\frac{W}{R_f^2\sigma}$ of unduloids and nodoids as a function of their dimensionless volume $\frac{V^{\frac{1}{3}}}{R_f}$. In Fig. 2.23, the dashed lines always show up before the solid lines, meaning that one would always expect to observe nodoidal drops first. Then, with the increase of drop volume, the nodoidal drop will become an unduloidal drop. Interestingly, in the phase diagram, the nodoidal domain increases fast with the increase of the contact angle. Suggesting that we probably can only observe nodoids but not unduloids wrapping up the fiber with a large contact angle.

2.6 Validation of existence of nodoidal drop on the fiber

In order to validate the existence of nodoidal drops wrapping up the fiber, we carried out the following experiments with hydrophobic Basalt fiber (FibreCoat GmbH) about 21 microns in diameter. The receding/advancing contact angles between the fiber and the DI water were analyzed from image sequences of withdrawing/immersing the fiber vertically from/in the water bath, as shown in Fig. 2.24(a) and Fig. 2.24(b), respectively.

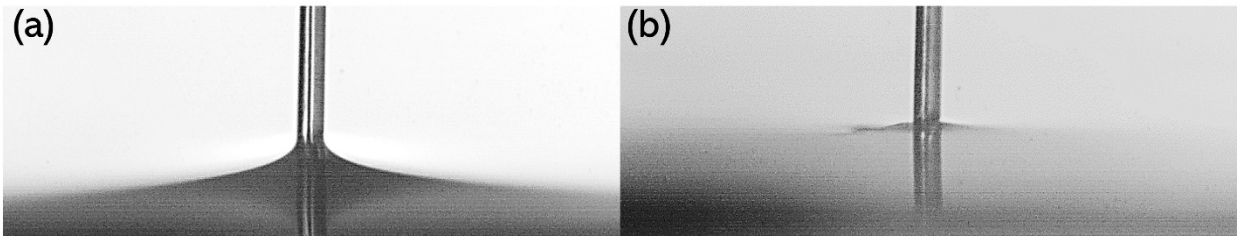

Fig. 2.24 (a) The fiber is withdrawn vertically from the water bath and makes a receding contact angle with a flat water surface at $56°$*, measured using the method in*

Ref[37]. (b) The meniscus is not observable during the advancing process, indicating the advancing contact angle is larger than $90°$.

The Basalt fiber is mounted on a special fiber holder (Fig. 2.25(a)); the gears on the holder allow us to rotate the fiber around its axis to check whether the drop wraps up the fiber or sits on a side of the fiber. A high-speed-motion camera (MotionProY4, Integrated Design Tools, Inc.) with the Olympus MVX10 microscope and a Halogen light source (F0–150, Fiberoptics Technology, Inc.) is used to observe the water droplets (see Fig. 2.25(b)).

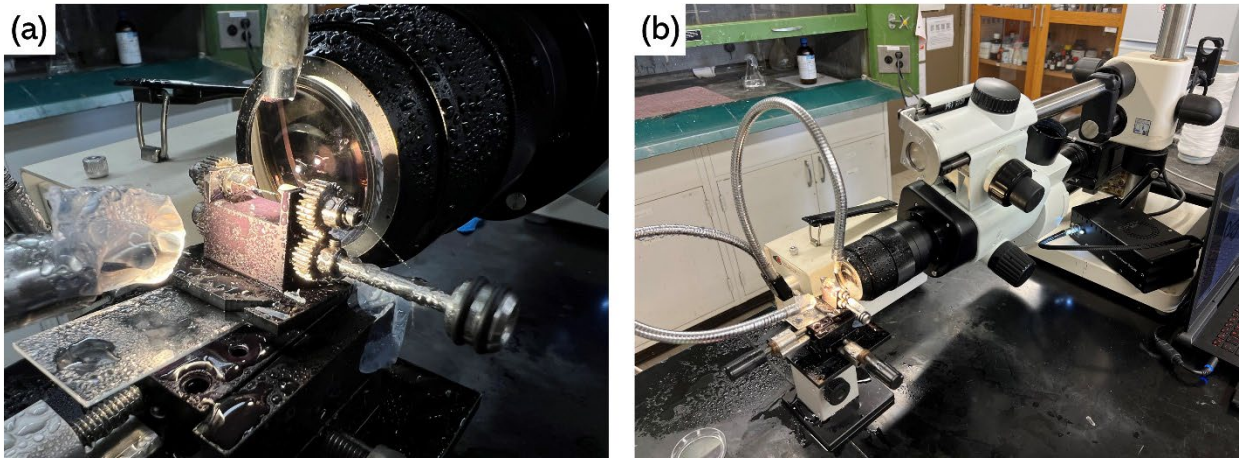

Fig. 2.25 (a) The Basalt fiber is mounted on the fiber holder. The gears on the holder allow us to rotate the fiber. (b) Actual experimental setup in the lab.

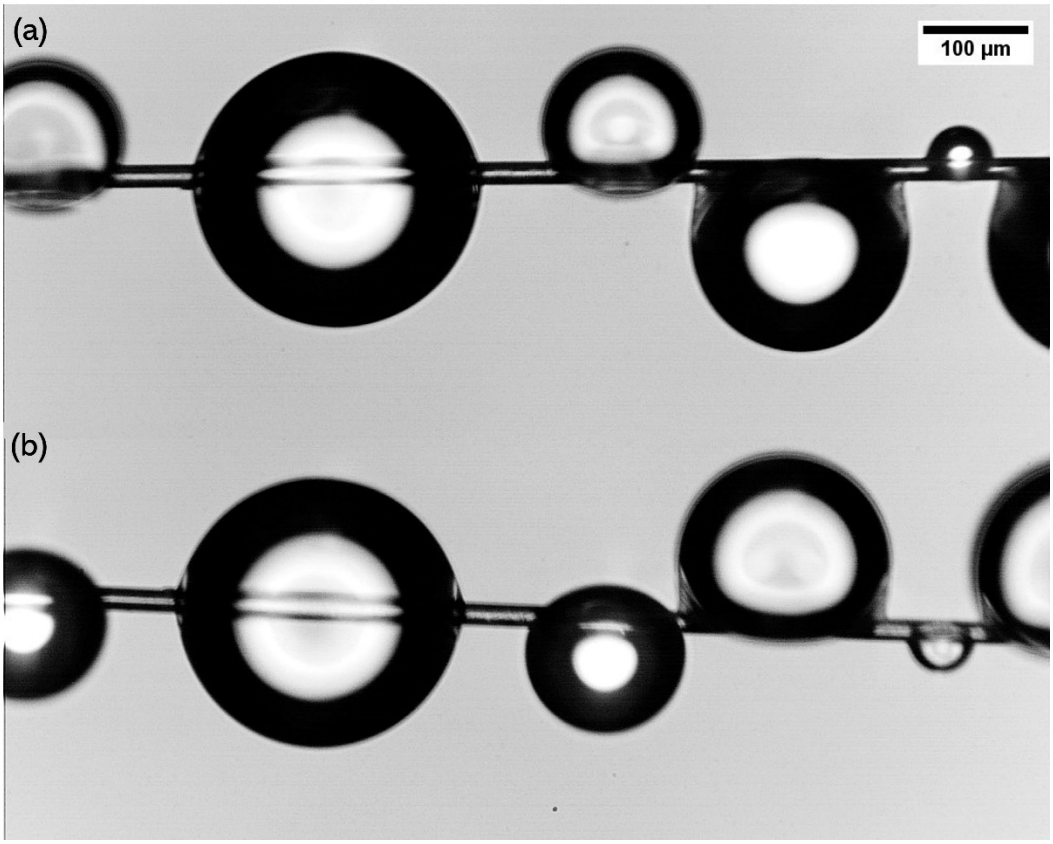

Fig. 2.26 (a) Droplets sprayed on the fiber. (b) The fiber was $180°$*rotated around the fiber axis.*

To obtain nodoidal drops on the fiber, we used a sprayer to deposit droplets on the fiber, and the camera recorded the process. Figure 2.26(a) shows a series of drops on the fiber after spraying water several times. Then we rotated the fiber about the fiber axis in $180°$ to check whether the drop wrapped up the fiber, see Fig. 2.26(b). Owing to the fact that the clamshell drop always rotate with the fiber, we can safely confirm that gravity plays no role in the phenomenon. Since the water drop in diameter of hundred microns

evaporated very fast during the experiments, we only analyzed the drop profile before the rotation.

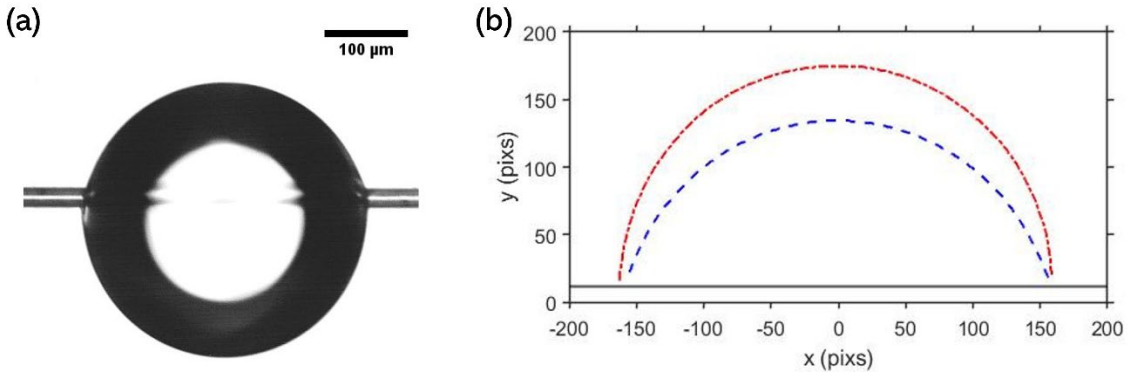

Fig. 2.27 (a) The suspicious nodoidal/unduloidal drop. (b) The red broken curve shows the drop profile of the bottom side, and the blue dashed curve shows the top profile. The black horizontal line is the fiber surface.

The LabView program "IMAQ Extract Contour VI" was used to extract the profile of the target droplet, then the profile of the top and bottom sides was loaded into the MATLAB for further analysis. For the convenience of the fitting process, the bottom side of the drop profile was flipped along the fiber axis. In Fig. 2.27(b), the red broken curve shows the flipped bottom of the drop, and the blue dashed curve shows the top profile. The black horizontal line is the fiber surface.

Take the red profile in Fig 2.27(b) for example. The R_{max} with respect to the fiber axis can be directly obtained from the extracted profile. And we also know that the R_{min} varies from the fiber axis to fiber radius, $0 < R_{min} < R_f$, where R_f is known. Fixing R_{max},

one can get a series of unduloids and nodoids by changing the R_{min} from 0 to R_f with different boundary conditions

$$\begin{cases} \gamma = \frac{\pi}{2}(y = R_{min}), \gamma = \frac{\pi}{2}(y = R_{max}), for\ unduloids \\ \gamma = -\frac{\pi}{2}(y = R_{min}), \gamma = \frac{\pi}{2}(y = R_{max}), for\ nodoids \end{cases} \tag{2.39}$$

And contact angle at the fiber surface can be obtained by substituting Eq. (2.13) and Eq. (2.14) into Eq. (2.15) for unduloids

$$\theta = \cos^{-1}\frac{R_f^2 + R_{max} * R_{min}}{R_f(R_{max} + R_{min})} \tag{2.40}$$

Or substituting Eq. (2.29) and Eq. (2.30) into Eq. (2.31) for nodoids

$$\theta = \cos^{-1}\frac{-R_f^2 + R_{max} * R_{min}}{R_f(R_{min} - R_{max})} \tag{2.41}$$

In Fig. 2.28(a), the black circles represent the bottom of the drop profile in Fig. 2.27, the dense red curves show all possible cases of unduloids, and the blue curves show all possible cases of nodoids. To evaluate whether the drop profile is a nodoid or a unduloid, we introduce a new parameter, the goodness of fit (gof) as: gof= $\frac{\sum_1^n \sqrt{\frac{X_i - x_i}{R_f}^2 + \frac{Y_i - y_i}{R_f}^2}}{n}$,where n is the number of data points extracted from the image, (Y_i, X_i) are the coordinates of experimental data, and (y_i, x_i) are the predicted coordinates of the nodoid or unduloid models. For each analyzed drop profile, the contact angle providing the smallest gof is considered the best-fit angle. Fig. 2.28(b) shows the gof as a function of contact angle, and the smallest gof is achieved when the drop profile is described by a nodoid function

with $\theta = 110.9°$. Further, the best-fit nodoid profile is represented in Fig. 2.28(c) with the drop profile. One can see that the nodoid profile perfectly covers the drop profile. Hence, we can confirm that this half drop is a nodoid. However, the top side of the drop in Fig 2.27 is fit by the unduloid function with $\theta = 54.9°$.

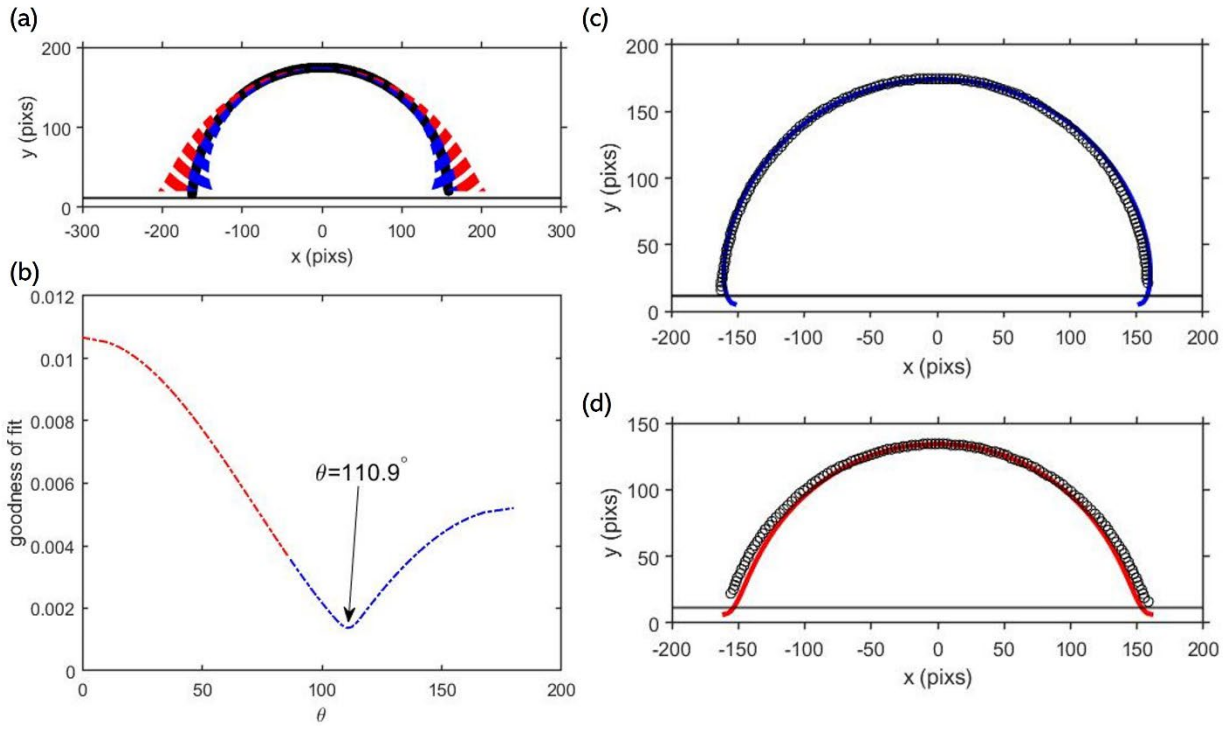

Fig. 2.28 (a) The black circles represent the broken red curve in Fig. 2.27(b), the dense red curves cover all possible cases of unduloids, and the blue curves cover all possible cases of nodoids. (b) The goodness of fit is plotted versus contact angle, and the smallest gof is achieved when the drop profile is described by a nodoid function with $\theta = 110.9°$*. (c) The best fit of the bottom profile of the drop in Fig. 2.27 is a nodoid making contact angle of* $110.9°$ *with the fiber. (d) The best fit of the top profile of the drop in Fig. 2.27 is an unduloid making contact angle of* $54.9°$ *with the fiber.*

Figures 2.29(a) to 2.29(c) show the process of spraying more droplets onto the fiber. In the beginning, an axisymmetric unduloidal drop formed on the fiber. The symmetry of

the drop is shown in Fig. 2.29(d) that the top profile (blue dashed curve) is nicely overlapped bottom profile (red broken curve). The best fit of the top profile is an unduloid with $\theta = 76.7°$, see Fig. 2.29(g). The best fit of the bottom profile is almost the same $\theta = 76.2°$.

Then we sprayed more water onto the existing droplets, the drop on the fiber evolved from Fig. 2.29(a) to Fig. 2.29(b). The drop is still highly axisymmetric, as shown in Fig. 2.29(e). Surprisingly, this spherical-like drop is still an unduloid but has a larger contact angle. Figure 2.29(h) shows the best-fit unduloid profile for the top side of the drop with $\theta = 82.8°$, and the best-fit contact angle for the bottom side is $82.5°$.

We sprayed one more time, and the axisymmetric drop suddenly lost its symmetry in Fig. 2.29(c). The top side of the drop is significantly larger than the bottom side, and the profiles of the top and bottom sides are represented in Fig. 2.29(f). Similar to the results for the drop in Fig. 2.27, but this time we have the top side fit with a nodoid with $\theta = 92.3°$ and the bottom side fit with a unduloid with $\theta = 62.9°$.

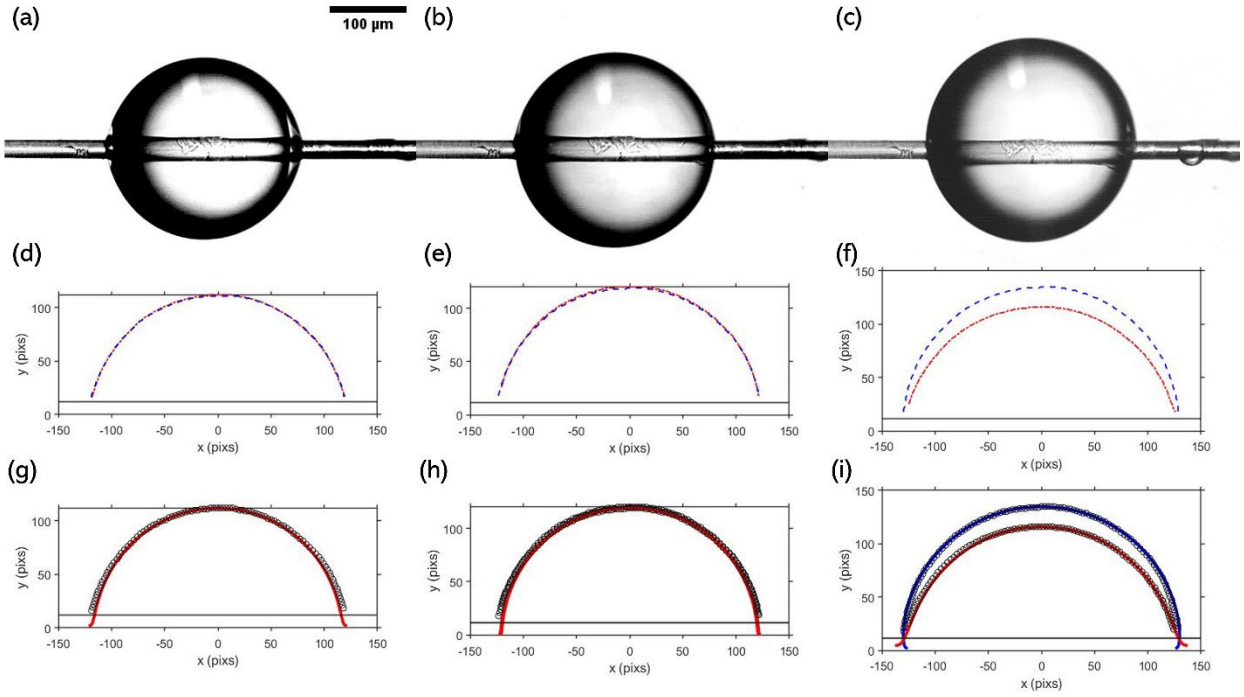

Fig. 2.29 (a)-(c) An axisymmetric unduloidal drop grew on fiber and eventually turned into a half unduloid-half nodoid shape. (d)-(e) show the top and bottom profile corresponding to (a)-(c), respectively. (g)-(i) show best-fit profiles corresponding to (d)-(f), respectively.

From the above validation experiments, we confirm the possibility of the existence of the nodoidal drop on the fiber; nevertheless, the drop is half unduloid and half nodoid. Compare the drop in Fig. 2.27(a) and Fig. 2.29(c), we can see that the half nodoidal drop can either form on the top side of the fiber or the bottom side. Indicating that the appearance of the nodoid is not due to gravity.

For curiosity, we also analyzed the hexadecane drop shape formed on the black fly larval silk which is naturally hydrophobic, and the image was taken by former students working in the group, Bochuan Sun and Tiffany Yeung. The black fly silk is about 5-10 μm

in diameter. Shown in Fig. 2.30(a), a huge symmetric hexadecane drop can form on the hydrophobic silk, the blue and red circles in Fig. 2.30(b) present the top and bottom profile of the drop, respectively, and the corresponding solid curves show the best fit unduloid profile. The best-fit angles are $67°$ and $74°$ for top and bottom respectively. More systematic study on the black fly larval silk will be done in the future.

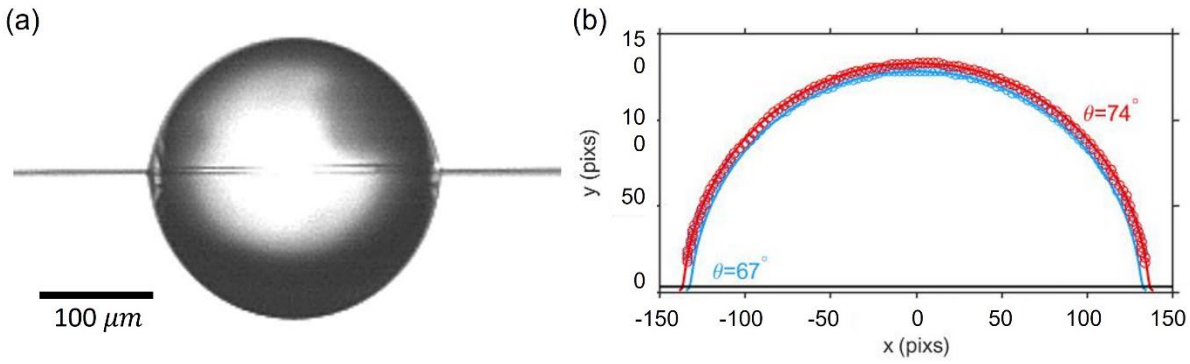

Fig. 2.30 (a) A hexadecane drop formed on the hydrophobic silk. (b) Profiles on both sides of the drop can be fitted by unduloidal function.

2.7 Conclusion

In this chapter, we theoretically analyzed all possible configurations of axisymmetric droplets on fibers. It is shown that the drops can be subdivided into two families, unduloidal and nodoidal droplets. The maximum drop radius R_{max}, capillary pressure ΔP, drop volume V and contact angle θ are the main parameters controlling the droplet shape. It is confirmed that axisymmetric droplets can be formed for the entire range of contact angles $0 < \theta < \pi$. This discovery opens up new avenue for development of fiber-based microfluidic devices for different applications.

2.8 References

1. Opell, B.D., et al., *Tuning orb spider glycoprotein glue performance to habitat humidity.* Journal of Experimental Biology, 2018. **221**(6).
2. Bai, H., et al., *Functional Fibers with Unique Wettability Inspired by Spider Silks.* Advanced Materials, 2012. **24**(20): p. 2786-2791.
3. Zheng, Y.M., et al., *Directional water collection on wetted spider silk.* Nature, 2010. **463**(7281): p. 640-643.
4. Koch, G.W., et al., *The limits to tree height.* Nature, 2004. **428**(6985): p. 851-854.
5. Dawson, T.E. and G.R. Goldsmith, *The value of wet leaves.* New Phytologist, 2018. **219**(4): p. 1156-1169.
6. Gotsch, S.G., et al., Life in the treetops: ecophysiological strategies of canopy epiphytes in a tropical montane cloud forest. Ecological Monographs, 2015. **85**(3): p. 393-412.
7. Sun, Y., et al., Making droplets from highly viscous liquids by pushing a wire through a tube. Physics of Fluids, 2022. **34**(3).
8. Eral, H.B., et al., Drops on functional fibers: from barrels to clamshells and back. Soft Matter, 2011. **7**(11): p. 5138-5143.
9. Ghosh, A., D. Bandyopadhyay, and A. Sharma, Micro-patterning of coatings on a fiber surface exploiting the contact instabilities of thin viscoelastic films. Physics of Fluids, 2018. **30**(11).
10. Keis, K., et al., Towards Fiber-Based Micro- and Nanofluidics,, in Nanoengineered Nanofibrous Materials, NATO Science Series II: Mathematics, Physics and Chemistry, S. Guceri, Y.G. Gogotsi, and V. Kuznetsov, Editors. 2004, Kluwer Publishing: New York. p. 175-182.
11. Marmur, A., *Measures of wettability of solid surfaces.* European Physical Journal-Special Topics, 2011. **197**(1): p. 193-198.
12. Marmur, A., et al., Contact angles and wettability: towards common and accurate terminology. Surface Innovations, 2017. **5**(1): p. 3-8.
13. Gennes, P.-G., F. Brochard-Wyart, and D. Quéré, *Capillarity and Wetting Phenomena: Drops, Bubbles, Pearls, Waves*. 2004, New York: Springer.
14. Bonn, D., et al., *Wetting and spreading.* Reviews of Modern Physics, 2009. **81**(2): p. 739-805.
15. Cassie, A.B.D., *Physics and textiles.* Reports on Progress in Physics, 1945. **10**: p. 141-171.
16. Miller, B., *The wetting of fibers*, in *Surface characteristics of fibers and textiles*, M.J. Schick, Editor. 1977, Marcel Dekker: New York. p. 417-445.
17. Duprat, C., *Moisture in Textiles.* Annual Review of Fluid Mechanics, 2022. **54**: p. 443-467.

18. Chou, T.H., et al., Equilibrium phase diagram of drop-on-fiber: coexistent states and gravity effect. Langmuir, 2011. **27**(7): p. 3685-92.

19. Xu, C.W., Z.Y. Lu, and L.R. Li, Surface Evolver Simulation of Droplet Wetting Morphologies on Fiber Without Gravity. Frontiers in Energy Research, 2022. **9**.

20. Gupta, A., et al., Effect of gravity on the shape of a droplet on a fiber: Nearly axisymmetric profiles with experimental validation. Physical Review Fluids, 2021. **6**(6).

21. Adam, N.K., *Detergent Action and its Relation to Wetting and Emulsification.* Journal of the Society of Dyers and Colourists, 1937. **53**(4): p. 121-129.

22. Plateau, J., Experimental and theoretical researches on the figures on equilibrium of a liquid mass withdrawn from the action of gravity, in Annual Report of the Board of Regents of the Smithsonian Institution 1863, Smithsonian Institution: Washington, DC. p. 207–285.

23. Rayleigh, L., *On the Capillary Phenomena of Jets.* Proceedings of The Royal Society of London, 1879. **29**: p. 71-97.

24. Thompson, D.W., *On growth and form*. 1945, New York Cambridge : University Press

25. Quere, D., *Fluid coating on a fiber.* Annual Review of Fluid Mechanics, 1999. **31**: p. 347-384.

26. Opell, B.D., *Water harvesting during orb web recycling.* Journal of Arachnology, 2020. **48**(3): p. 278-283.

27. Stellwagen, S.D., B.D. Opell, and M.E. Clouse, *The impact of UVB radiation on the glycoprotein glue of orb-weaving spider capture thread.* Journal of Experimental Biology, 2015. **218**(17): p. 2675-2684.

28. McHale, G. and M.I. Newton, *Global geometry and the equilibrium shapes of liquid drops on fibers.* Colloids and Surfaces A: Physicochemical and Engineering Aspects, 2002. **206**: p. 79-86.

29. McHale, G., M.I. Newton, and B.J. Carroll, *The shape and stability of small liquid drops on fibers.* Oil & Gas Science and Technology-Revue De L Institut Francais Du Petrole, 2001. **56**(1): p. 47-54.

30. Carroll, B.J., The Accurate Measurement of Contact-Angle, Phase Contact Areas, Drop Volume, and Laplace Excess Pressure in Drop-on-Fiber Systems. Journal of Colloid and Interface Science, 1976. **57**(3): p. 488-495.

31. Langbein, D.W., Capillary Surfaces: Shape - Stability - Dynamics, in Particular Under Weightlessness Springer Tracts in Modern Physics. 2002, New York: Springer.

32. Birdi, K.S., Handbook of surface and colloid chemistry. 2016.

33. McHale, G., et al., *Wetting of a High-Energy Fiber Surface.* J Colloid Interface Sci, 1997. **186**(2): p. 453-61.

34. Rebouillat, S., B. Letellier, and B. Steffenino, *Wettability of single fibres – beyond the contact angle approach.* International Journal of Adhesion and Adhesives, 1999. **19**(4): p. 303-314.

35. Carroll, B.J., Equilibrium conformations of liquid drops on thin cylinders under forces of capillarity. A theory for the roll-up process. Langmuir, 1986. **2**(2): p. 248-250.

36. McHale, G., M.I. Newton, and B.J. Carroll, *The shape and stability of small liquid drops on fibers.* Oil & Gas Science and Technology-Revue D Ifp Energies Nouvelles, 2001. **56**(1): p. 47-54.

37. Zhang, Z., F. Peng, and K.G. Kornev, The Thickness and Structure of Dip-Coated Polymer Films in the Liquid and Solid States. Micromachines, 2022. **13**(7): p. 982.

CHAPTER III

MORPHOLOGICAL TRANSITION OF DROP CONFIGURATIONS ON CYLINDRICAL FIBER

3.1 Introduction

When the weight $W = \rho V g$ of a small drop of volume V and density ρ suspended in the air is much smaller than the surface tension force $F = \sigma V^{1/3}$, i.e. the inequality $Bo = \frac{W}{F} = \frac{\rho V^{\frac{2}{3}} g}{\sigma} << 1$ holds true, the drop takes on spherical shape. The Bond number Bo therefore sets the conditions when the gravity g can be neglected. When the droplet in the small Bond number case, Bo "1, is brought in contact with a substrates, its shape is not fully defined by the surface tension, but it also depends on the contact angle that the drop makes with this substrate[1].

The drop can rest on cylindrical fiber either as an asymmetric clamshell or as an axisymmetric barrel-like drop[2]. The transition between these configurations is poorly understood but knowing conditions of this transition is crucially important for improving the performance of fiber-based microfluidic devices[3-11].

The mechanism of barrel-clamshell morphological transition was discussed by Carroll [12, 13] and his ideas have been accepted in the literature[10, 14-16]. In Ref.[13], Carroll presented the experimental method and theory describing this transition. Drops of oil soluble in an aqueous solution were placed on a fiber and initially formed the liquid barrels. Over time, the drop volume decreased as the oil dissolved in solution, and, at some critical volume, the drop changed its conformation from barrel to clamshell. Carroll

introduced a phase diagram plotting the transition boundary between barrel and clamshell in terms of the ratio of the radius R_d of the smallest barrel drop at its critical volume to the fiber radius R_f , $n = R_d/R_f$ versus contact angle (θ) that oil makes with the fiber[13]. This diagram, Fig. 3.1, was further studied extensively as theoretically as well as experimentally [10, 14-18].

Carrol proposed a metastability condition, the solid line in Fig. 3.1. McHale and Newton[14] noted that the metastability condition required that the drop should meet the fiber at the contact angle corresponding to the inflection point where the curvature of the generator of axisymmetric drop profile changes the sign from positive to negative[14, 19]. They proposed to replot the diagram in terms of the inflection contact angle, as shown by the dashed line in Fig 3.1.

To reexamine the phase diagram, McHale and Newton[20, 21] directly evaluated the surface free energy of the clamshell drops and the barreled drops by the finite element method using Brakke's Surface Evolver. For the given drop volume and contact angle, the drop conformation should be determined by the lowest possible surface free energy. The results of the numerical experiments were reported as the "absolute condition" in Ref.[21] and presented in Fig. 3.1 as the hollow circles.

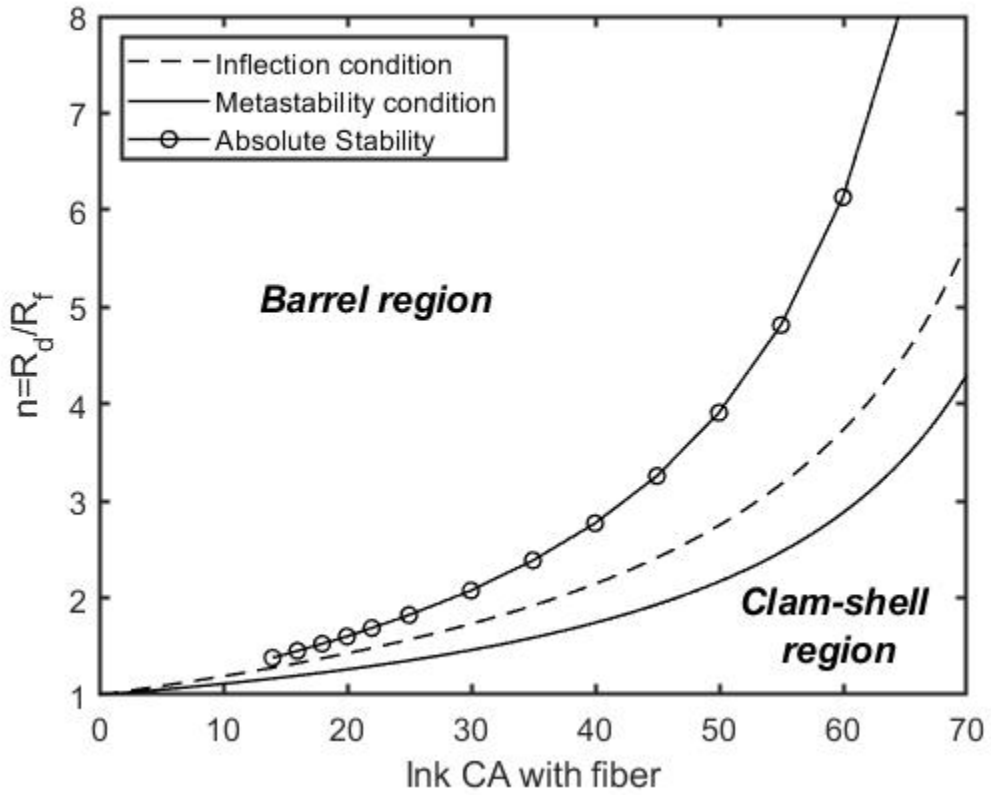

Fig. 3.1 The phase diagram shows the transition boundary between the barrel and clamshell drop: (1) metastability condition[13], (2) absolute stability[21], and (3) inflection condition[14].

The following conclusions can be drawn from these analyses: in the $Bo << 1$ regime, droplets of nonwetting fluids, $\theta > 90°$, cannot form barrels. For small contact angles and large droplet volumes, the barrel shape is energetically favorable: the fiber-droplet contact area is larger than that of the clamshells. In contrast, the clamshells are energetically favorable for large contact angles and small droplet volumes. The conformation between barreled and clamshell droplets can be changed by temperature [22] or electric potential [10].

Although the theory of drop transition on a single fiber has been extensively studied[12-14, 19-21, 23], experimental analysis of drop transition is limited from clamshell shape to barrel shape. Mugele's group conducted, probably, the most rigorous experimental analysis of the barrel-clamshell transitions of droplets on fibers[10]. They employed electrowetting phenomenon to change the contact angle in situ. They compared experiments and numerical modeling, to show that the barrel to clamshell transition and the clamshell to barrel transitions are governed by different mechanisms. On the phase diagram, they introduced meaningful bistable region and specified the barrel domains and clamshell domains.

In this chapter, we experimentally investigate the critical conditions for the barrel-clamshell transitions. In this investigation, liquids and fibers with distinguishing surface properties and methods of drop formation have been used. We noticed that at very small Bond numbers, no barreled drops that go from clamshells could be axisymmetric. Flipping droplets upside down, we noticed that the drop would follow the direction of fiber rotation and the larger side would go to the top and remain larger. These observations rule out any effect of gravity suggested recently for explanation of asymmetric shape of droplet at small Bond numbers [24]. We hypothesize that the contact angle hysteresis is responsible for the shape asymmetry.

We confirm observations of Mugele's group regarding two distinguishing scenarios of morphological transition of drop configurations on fibers[10]. While these observations were made using the electrowetting phenomenon, we question whether the same

boundary of barrel-to-clamshell transition could be obtained when one deposits droplets on fibers and when the droplets are formed by breaking up a coating layer on the fiber surface. Two types of experiments were carried out to determine the barrel-to-clamshell transition boundary.

3.2 Drop deposited on a fiber

In one scenario, we can grow a clamshell drop on a dry fiber by printing tiny droplets to the same mother droplet. When the size of the growing clamshell reaches its critical value, the drop spontaneously forms barrel (see Fig. 3.2). Since the drop is deposited on dry fiber, the contact line moves forward over the dry surface and drop forms with the fiber advancing contact angle. Figure 3.2 shows how the drop conformation changes as its volume increases. The zero second picture indicates the shape of the very first drop just after its deposition on the fiber. After that, the drop starts to grow fed by the impacting microdroplets. While growing it spreads over the fiber top side (0 S – 6 S in Fig. 3.2). Then, the clamshell propagates from the top to the fiber sides. When the drop volume reaches its critical value and the contact angle allows the clamshell to move at the fiber bottom, it will suddenly transform to a barrel drop. Finally, an axisymmetric barreled drop is formed on the fiber; at this moment the printing stops and the drop rests in this equilibrium configuration (57 s in Fig. 3.2).

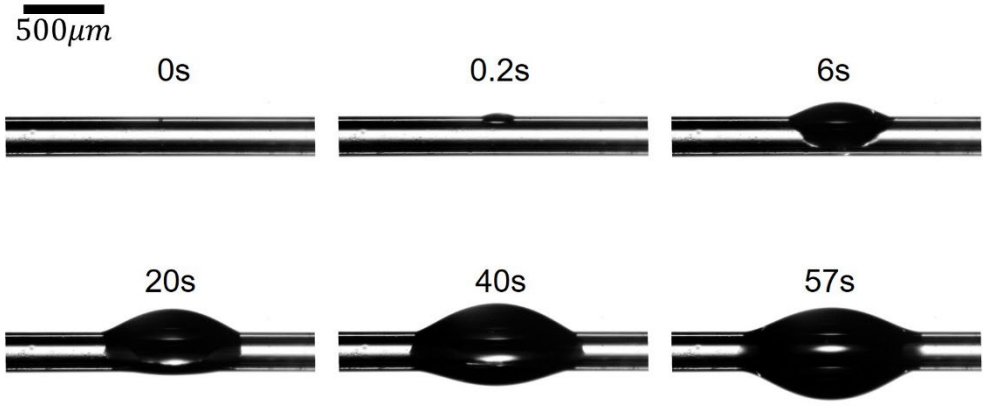

Fig. 3.2. A hexadecane drop grows on a capillary tube of $2R_f$ =250 μm diameter and finally transits from a clamshell to a barreled drop. Hexadecane makes 37° advancing contact angle and 28° receding contact angle with the tube.

3.2.1 Experiment

3.2.1.1 Experimental setup

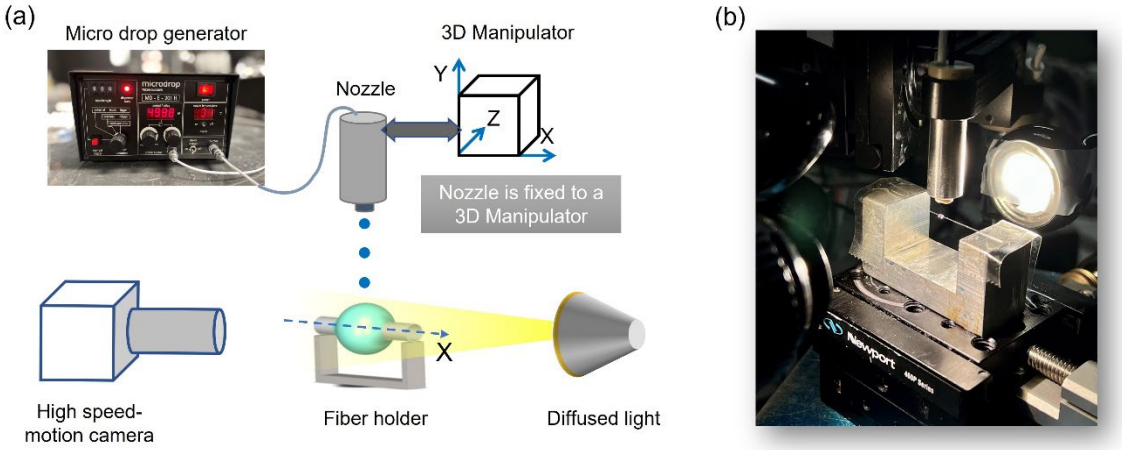

Fig. 3.3 (a)The setup consists of three main parts. (1) A single fiber is mounted on a U-shaped fiber holder to collect droplets. (2) A printing nozzle driven by a microdrop dispenser can deposit the precisely controlled droplets on the fiber. The nozzle is attached to a 3D manipulator. (3) A high speed-motion camera and a diffused light

source are used to record the drop conformation on the fiber. (b) The picture of the actual experimental setup.

The schematic of the experimental system for the drop deposition is shown in Fig. 3.3(a). The picture of the actual experimental setup is shown in Fig. 3.3(b). Firstly, the fiber was mounted on a U-shaped fiber holder along the fiber axis, X-axis, and the holder was attached to a two-dimensional (2D) linear stage. The printing nozzle of the microdrop dispenser (MD-E-201H, Microdrop Technologies) attached to the three-dimensional (3D) micromanipulator (MP-285 Shutter Instrument Company) was placed about 600 – 800 μm directly above the fiber. The microdrop dispenser was set to generate hexadecane drop of the radius as small as r =13.9 μm every $t_0 = 4950\ \mu s$. Each drop has a volume of about $V_{drop} = 1.13 \times 10^{-5}\ \mu L$. A high speed-motion camera (MotionProY4, Integrated Design Tools, Inc.) with a microscope (Navitar 1-60135) and a light source (InterTek 4002352) with a diffuser (a piece of invisible tape) were used to record the process of drop growth on the wire. The microdrop dispenser has to be calibrated before the experiments to ensure correct settings. The calibration procedure is detailed below.

3.2.1.2 Calibration of the microdrop dispenser

The microdrop dispenser produces single micro drops by applying a pulsed voltage to the piezo actuator inside the printing nozzle. The applied voltage and pulse length are adjusted to dispense microdroplets of the same diameter. The stroboscope (Fig. 3.4(a))

supplied with the microdrop dispenser is used to ensure that only a single drop per pulse is printed from the nozzle, see Fig. 3.4(b).

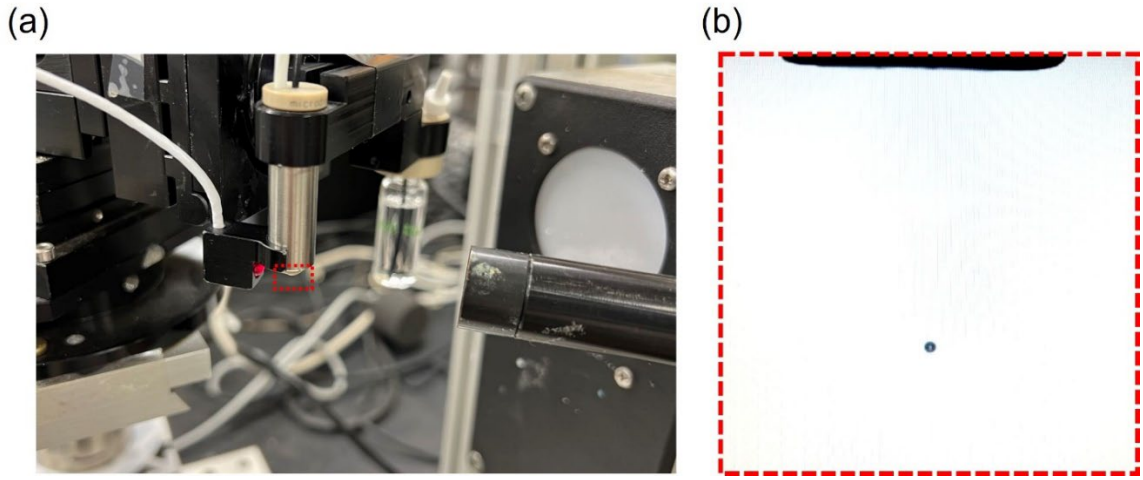

Fig. 3.4 (a) The stroboscope monitors the drop formation process. (b) One has to ensure that only a single drop per pulse is generated.

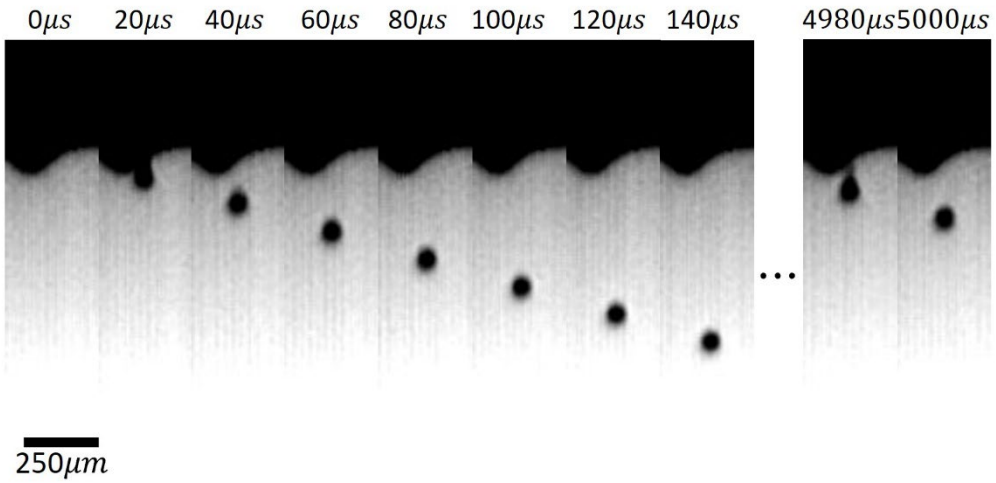

Fig. 3.5 High-speed image sequence shows how the drops are printed continuously from the nozzle.

After confirming that the microdrop dispenser is working as it is supposed to work, we record several videos at 50,000 frames per second to check the printing frequency, Fig. 3.5. Every 247.5 frames, a new droplet can be observed emerging from the nozzle, suggesting that the average printing period is about 4950 μs.

In Fig. 3.5, the image of droplets recorded at 50,000 fps are not crisp owing, i.e. to the drop velocity is too high. By decreasing voltage on the dispenser panel, we can significantly decrease the initial velocity of the printed droplets to grab the image of a single droplet for volume evaluation. Images in Fig. 3.6 show crisp pictures of single droplets moving in the air. ImageJ is used to measure the area (A) of each micro drop shown in the video, then the radius of each drop was calculated as $r = \sqrt{\frac{A}{\pi}}$ =13.9 $\pm$ 0.2 μm.

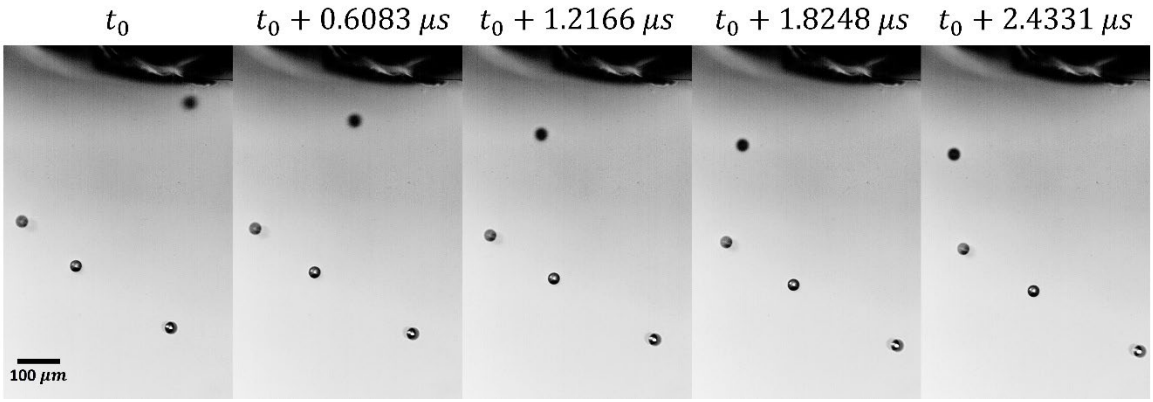

Fig. 3.6 Droplets printed at a low applied voltage at the same printing frequency.

3.2.1.3 Methods and materials

In order to deposit each micro drop on the fiber, the position of the printing nozzle was adjusted by the 3D micromanipulator in the XZ-plane with small steps closer to the fiber until we observed that the drop hit the top surface of the fiber. Then, the position of the nozzle was not changed anymore during experiments. Before each experiment, we moved fiber along the length of the fiber to find a clean area for the drop placement, then turn on the microdrop dispenser. Each experiment was repeated at least 5 times. Videos were recorded at 50 fps for those tubes with an advancing contact angle smaller than 40°. For experiments carried out with tubes with an advancing contact angle larger than 40°, the entire drop growing on the fiber was recorded at 25 fps. The transition process was recorded at 500 fps. When the transition from clamshell to barrel happened, we immediately stopped printing.

To confirm the validity of the models summarized in the phase diagram and understand dynamic transition of droplet on a single fiber, it is essential to have fibers with different surface energy, which can provide different dynamic contact angles with the tested fluids.

Two capillary glass tubes (Vitrocom) with $2R_f = 250\ \mu m$ and $2R_f = 80\ \mu m$ were used as substrates. Compared with polymer fibers or metal wires, the glass capillary tubes provide a smooth surface without any grooves or significant defects. To avoid the Influence of liquid evaporation during experiments with small droplets, hexadecane (TCL) was used as the fluid.

To change the surface energy of the tube, chemical vapor deposition (CVD) of silanes was employed.

The capillary tubes were equally cut into two pieces. Both open ends of the tube were sealed for further contact angle characterization. We cleaned uncoated samples in methanol for 5 mins to remove the finish. Then we placed dried samples in the plasma instrument (PLASMA CLEANER/STERILIZER, Harrick Scientific Corp, PDC-32G, Input power 100 W, Highest settings: 720V DC, 25 mA DC, Applied to 18 W) to activate the surface. First, we need to vacuumize the chamber with an external vacuum pump. When the millitorr vacuum gauge showed that the pressure inside the chamber was under 200 mTorr, we turned on the PLASMA CLEANER/STERILIZER and set it to High. The vacuum pump was still working. The plasma treatment would take 15 minutes. Then, we turned off both the plasma instrument and the vacuum pump and carefully aired the chamber.

The samples were taken out from the chamber of the plasma instrument and immediately put into 50 ml centrifuge tubes (CELLTREAT Scientific Products) with different silanes present. We left all samples in the sealed centrifuge tubes for CVD overnight for about 12 hours to graft silanes on the surface.

Four types of silanes were used to modify the tubes to provide different surface energies: 2-[Methoxy(Polyethyleneoxy)6-9propyl]trimethoxysilane, Methacryloxypropyltrimethoxysilane, n-Octyldimethylchlorosilane, (Tridecafluoro-1,1,2,2-Tetrahtdrooctyl)trimethoxysilane. The dynamic contact angles between coated

tubes with hexadecane were measured using the K100 Force Tensiometer(KRÜSS), and the results are shown in Table 3.1.

Table 3.1 Contact angle between hexadecane and capillary tubes

tube O.D.[mm]	silane	Advancing CA[°]	Receding CA[°]
0.25	2-[Methoxy(Polyethyleneoxy)6-9propyl]trimethoxysilane	22±2	18±3
0.25	Methacryloxypropyltrimethoxysilane	29±2	19±3
0.25	UNTREATED TUBES	35±2	27±1
0.08	n-Octyldimethylchlorosilane	44±2	34±2
0.08	(Tridecafluoro-1,1,2,2-Tetrahtdrooctyl)trimethoxysilane	62±2	24±3

Besides the capillary tubes, the Basalt fiber (FibreCoat GmbH) of about 21 microns in diameter is also used in this experiment. Since the wetting force acting on the fiber is too small to be detected by the force tensiometer, the receding/advancing contact angles between the fiber and the hexadecane were analyzed using meniscus shape from the image sequences of the fiber being withdrawn/immersed vertically from/in the hexadecane bath. Figure 3.7 demonstrates the results of best fitting of meniscus surface on the Basalt fiber using advancing contact angle $47 \pm 1°$. This angle remains the same after 3 repeats. Receding contact angle was measured to be $32 \pm 2°$ after 3 repeats.

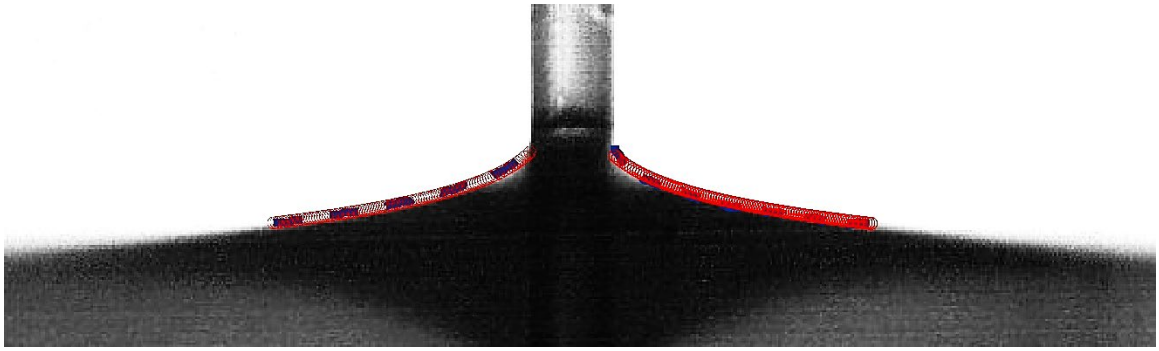

Fig. 3.7 The fiber that has been immersed vertically into hexadecane. The red curve shows the best-fit meniscus profile using the method of Refs. [25, 26]. The blue dashed curves show the extracted meniscus profile by the LabView program "IMAQ Extract Contour VI". These fitting provides $47°$ advancing contact angle with hexadecane on the left and 49° on the right sides.

3.2.2 Observation of drop-on-fiber

Different phenomena were observed depending on advancing contact angle formed between hexadecane droplets and the tubes. We will discuss these phenomena for different ranges of contact angles.

3.2.2.1 Small advancing contact angles, $\boldsymbol{\theta_{adv} = 22° \& 29°}$

When hexadecane drop forms with the tubes advancing contact angle smaller than 30°, very similar phenomena were observed for the drop transition. Figure 3.8 depicts the transition process of hexadecane drop on a single fiber with $22°$ advancing contact angle. The yellow arrows point the direction of liquid flow during the transition from clamshell to barrel.

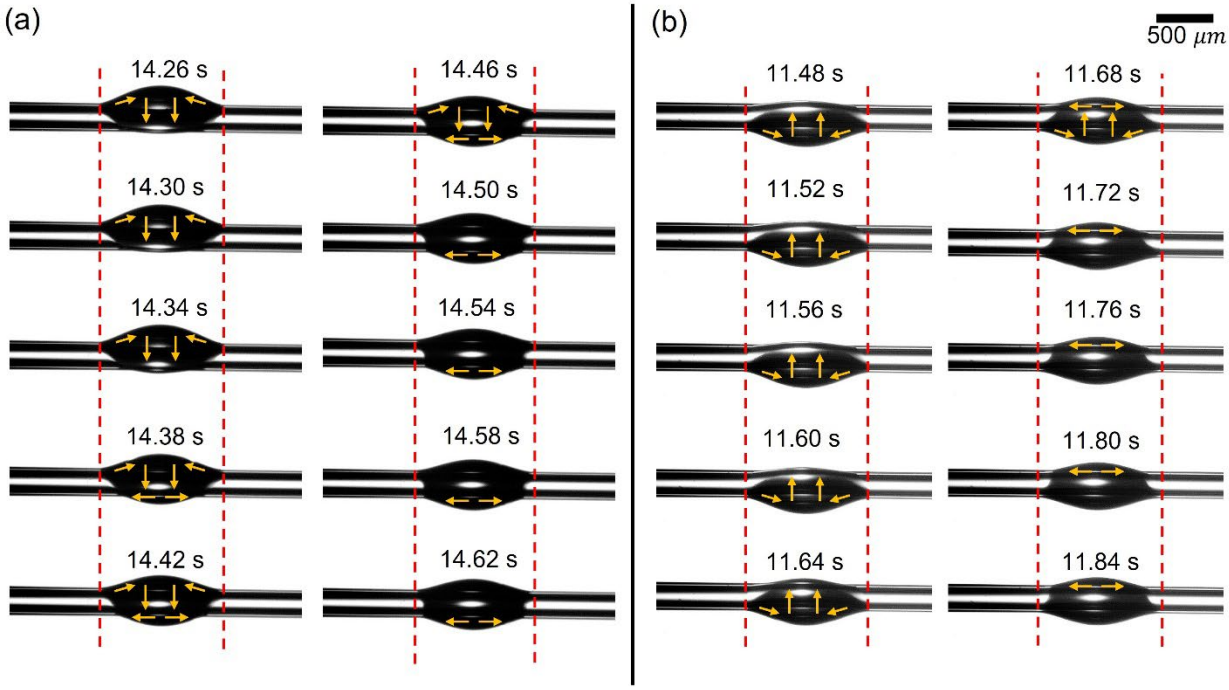

Fig. 3.8 (a) A hexadecane drop transit from clamshell to barrel on a capillary tube of $2R_f$ =250 μm diameter at 22°advancing contact angle. The clamshell drop was deposited from above of this tube and then transited to the barrel drop. (b) The clamshell drop was deposited from below of the same tube and then transited to the barrel drop.

In Fig. 3.8(a), the clamshell drop was deposited from above on the fiber top surface. The liquid in the drop suddenly speeded up to spread from the side surface to the dry bottom surface. Then the clamshell-barrel transition happened. As the arrows indicated, the half barrel drop was spreading on the bottom side of the tube while the other half barrel was gathering on the top side. The red dashed line shows that the contact line on the top was pinned during the transition; however, the contact line on the bottom significantly extended.

In the experiment shown in Fig. 3.8(b), we printed drops on the sidewall of the tube. In this case, when the clamshell grew further, it moved to the bottom of the tube. In the sequence of pictures shown in Fig. 3.8(b), the clamshell drop has already been formed at the tube bottom and we track the droplet movement after that moment on to illustrate transition from the clamshell to barrel drops. The phenomenon was similar to that shown in Fig. 3.8(a) but the flow occurred in the direction opposite to the direction of acceleration due to gravity, proving that gravity plays no role in this transition.

The transition in the case of $29°$ contact angle happens within about 0.34 s, which is 0.06 s faster than in the case of $22°$ contact angle. Thus, the greater the angle, the faster the clamshell-barrel transition.

3.2.2.2 Medium advancing contact angle, $\boldsymbol{\theta_{adv} = 35°}$

Different from the smaller contact angles, two different transition modes were observed when the contact angle increased. The transition process shown in Fig. 3.9(a) is similar to the phenomenon observed at smaller contact angles: the drop spreads on the bottom side of the tube and gathers on the top side. Compared with the small contact angle cases where the transition happened in 0.4 s - 0.34 s, the process shown in Fig. 3.9(a) was completed in 0.1 s.

A different transition mode could sometimes be observed during experiments with this capillary tube. This mode had never been observed in tubes with smaller contact angles. As shown in Fig. 3.9(b), from 50.00 s to 60.00 s, the clamshell rolled over the tube slowly and eventually sat on the bottom of the tube. One notices that the drop shapes at

50 s and 54 s in Fig 3.9(b) are very close to that at 56.94 s in Fig. 6(a), which is the first frame of the sequence in Fig 6(a). Instead of becoming a barrel drop immediately after rolling over the fiber, the clamshell on the bottom side kept growing for 5.08 s (60.00 s to 65.08 s in Fig. 3.9(b)), then suddenly transited to the barrel shape (65.08 s to 65.22 s in Fig. 3.9(b)). These observations suggest that the clamshell drop remains stable until it reaches a critical volume, even if one purposely wets the dry bottom of the clamshell drop.

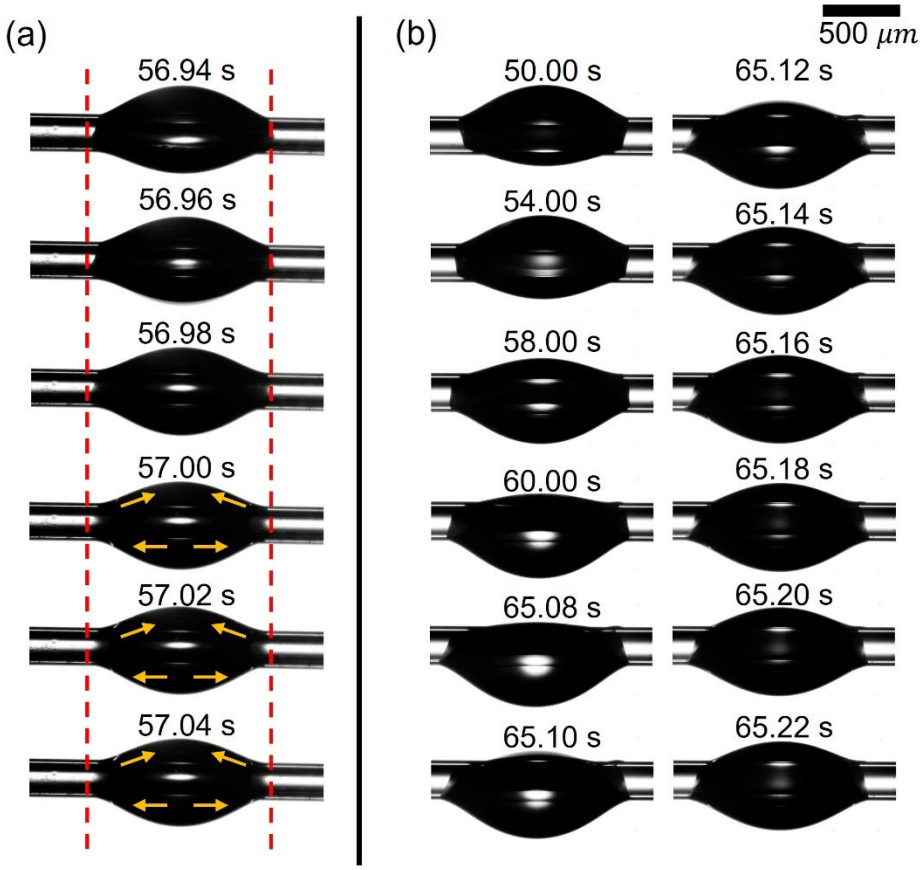

Fig. 3.9 (a) A hexadecane drop transit from the clamshell shape to the barrel shape on a capillary tube of $2R_f$ =250 μm diameter at 35° advancing contact angle. (b) The hexadecane clamshell drop was deposited from above on the tube top. Then the drop rolled from the top to the bottom of the tube and kept growing. The clamshell eventually became a barrel drop.

3.2.2.3 Intermediately large advancing contact angles, $\boldsymbol{\theta_{adv} = 44^{\circ} \& 47^{\circ}}$

According to the phase diagram shown in Fig. 3.1, when the contact angle is larger than 40°, we expect that the critical volume for the clamshell-barrel transition should significant increase. To reduce the influence of gravity, the 80 μm diameter capillary tubes were used for more hydrophobic coatings. What attracts our attention is that the size of the barrel-like drop at its critical volume was much larger than that predicted by the accepted phase diagram[15]. Figure 3.10 shows a normal transition from clamshell- to barrel. Similarly, the contact line was pinned during the transition indicated by the red dashed line. The transition in this case took only 0.014 s, which is one order of magnitude faster than the previous ones.

Figure 3.11 illustrates this transition on the Basslt fiber, which was finished in 4 ms. At the beginning of the transition, the contact lines were still pinned; however, the contact line slightly extended right before the transition finished in this case.

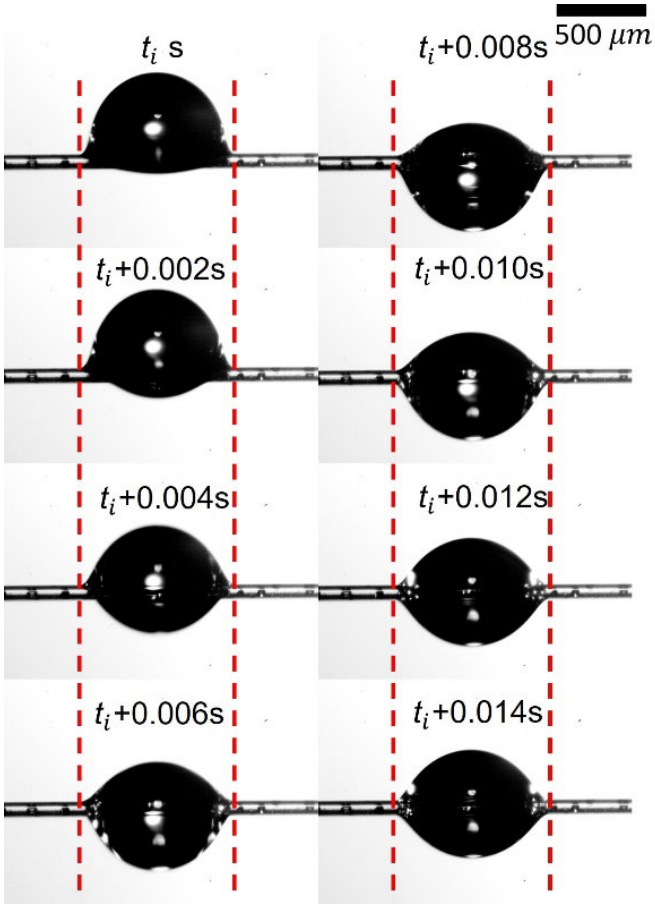

Fig. 3.10 A hexadecane drop transit from clamshell to barrel on a capillary tube of $2R_f$ =80 μm diameter at 44°advancing contact angle.

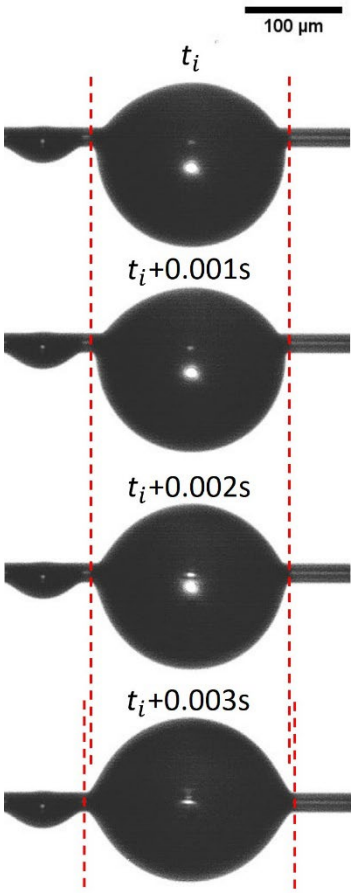

Fig. 3. 11 A hexadecane drop transit from clamshell to barrel on Basalt fiber of $2R_f$ =42 μm diameter at 47° advancing contact angle.

3.2.2.4 Large advancing contact angle, $\theta_{adv} = 62^\circ$

An exciting experimental result was discovered in this case. We tried growing drops at different positions along the 80 μm diameter tube, but no clamshell drop can transit to a barrel drop. Fig. 12(a) and Fig 12(b) were taken 5 minutes after we stopped printing any droplets on the fiber. As shown in Fig. 12(a), relatively large clamshell drops can stably sit on the top of the tube surface. There is no bridge connecting the adjacent clamshell

drops (one on the top surface and the other on the bottom surface), meaning that the bottom side of the clamshell drop is completely dry. To further prove that the bottom side of a clamshell drop is dry, we grew some drops on the top of the clamshell, as shown in the zoom-in picture in Fig. 12(b). The fact that these tiny droplets can stay on the surface but not be absorbed by the adjacent clamshell drop supports our statement.

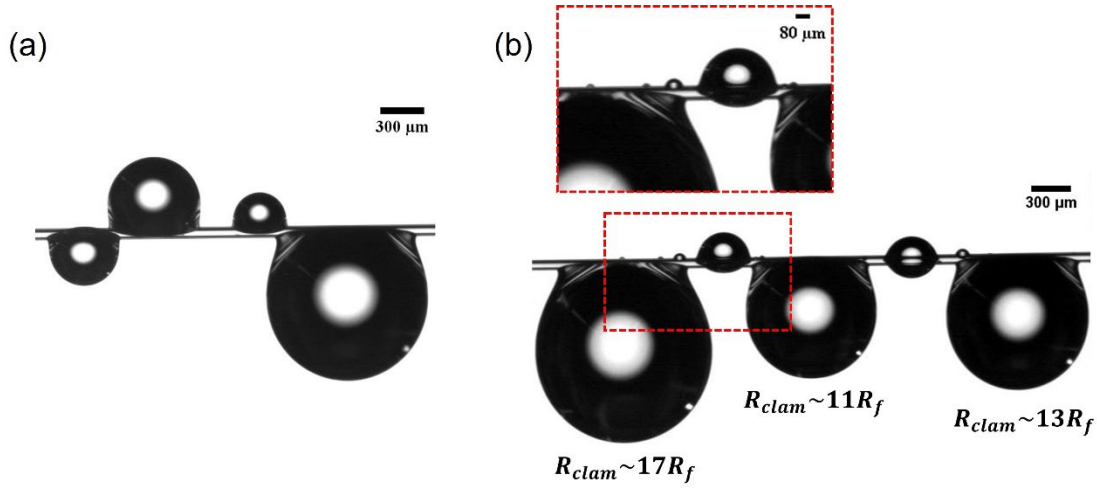

Fig. 3.12 (a)Clamshell is the only drop conformation observed when hexadecane makes 62° advancing contact angle with the tube. (b) Some tiny drops were purposely placed on the bottom side of the clamshell drop, and none of them disappeared later.

3.2.3 Results and discussions

Glass tubes and fibers making advancing contact angles of 22°, 29°, 35°, 44°, 47° with hexadecane allowed us to investigate characteristic features of clamshell-barrel transition. As the critical barrel drop, we consider the first barrel drop after the clamshell-barrel transition is completed for the first time. The volume of that drop is the critical volume required for a clamshell drop to transit to the barrel drop. Figure 3.13 summarizes the

critical barrel drop making different contact angles on tubes/fibers. The critical barrel-like drop size relative to the fiber size increases apparently with the increase of the contact angle.

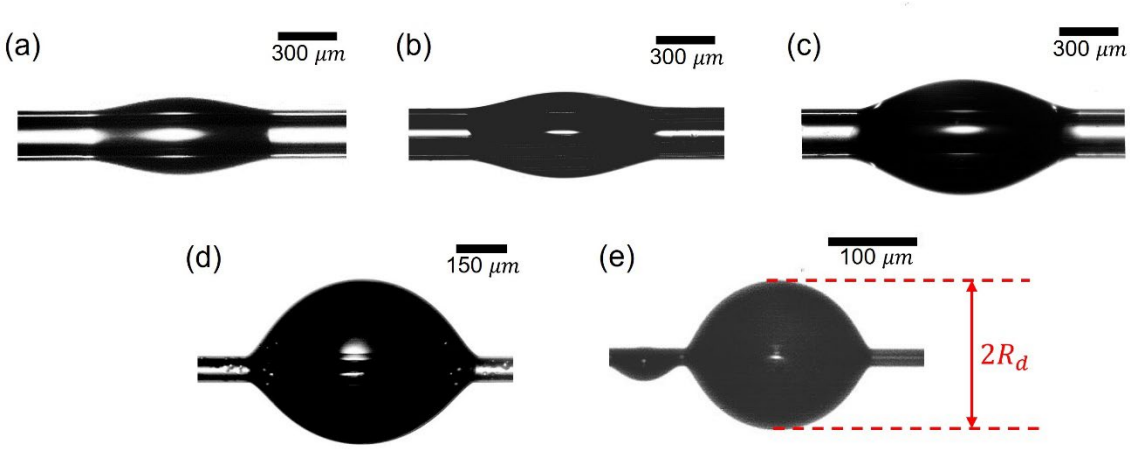

Fig. 3.13 The first critical barrel drops formed from clamshells on fibers at different advancing contact angles. (a) $\theta_{adv} = 22°$, $\theta_{rec} = 18°$. *(b)* $\theta_{adv} = 29°$, $\theta_{rec} = 19°$. *(c)* $\theta_{adv} = 35°$, $\theta_{rec} = 27°$. *(d)* $\theta_{adv} = 44°$, $\theta_{rec} = 34°$.*(e)* $\theta_{adv} = 47°$, $\theta_{rec} = 32°$.

To investigate the Influence of the contact angle in the clamshell-barrel transition, we calculate the critical ratio[13] n from all critical barrel drops in the experiments. It is notable that the barrel drops formed from clamshell drops are always slightly asymmetric. We redefine the barrel radius as $R_d = \frac{maximun\ distance}{2}$ (illustrated in Fig. 3.13(e)), thus the ratio $n = R_d/R_f$ can be calculated.

The experimental results are added to the phase diagram. In Fig. 14, the relation between the critical ratio n and measured advancing contact angles is shown by blue crosses, with the error bars calculated as the half-value width of their standard deviation

measured in experiments. Additionally, the red shadow area in Fig. 3.14 indicates the region where there is no transition from clamshell to barrel. Surprisingly, while the method of drop formation assumes that the barrel should be formed from clamshells, most of our data for small and medium contact angles follow the inflection point criterion [13] but the barrels at larger contact angles appeared above the absolute stability boundary[21]. The experimental results reveal that the deposited drop will never form barreled droplets when the advancing contact angle is greater than $62°$. According to the trend of blue crosses showing a steep increase of the borderline for barreled droplets, we would not be surprised to see the non-barrel region starting from the smaller advancing contact angles of about $50°$-$60°$.

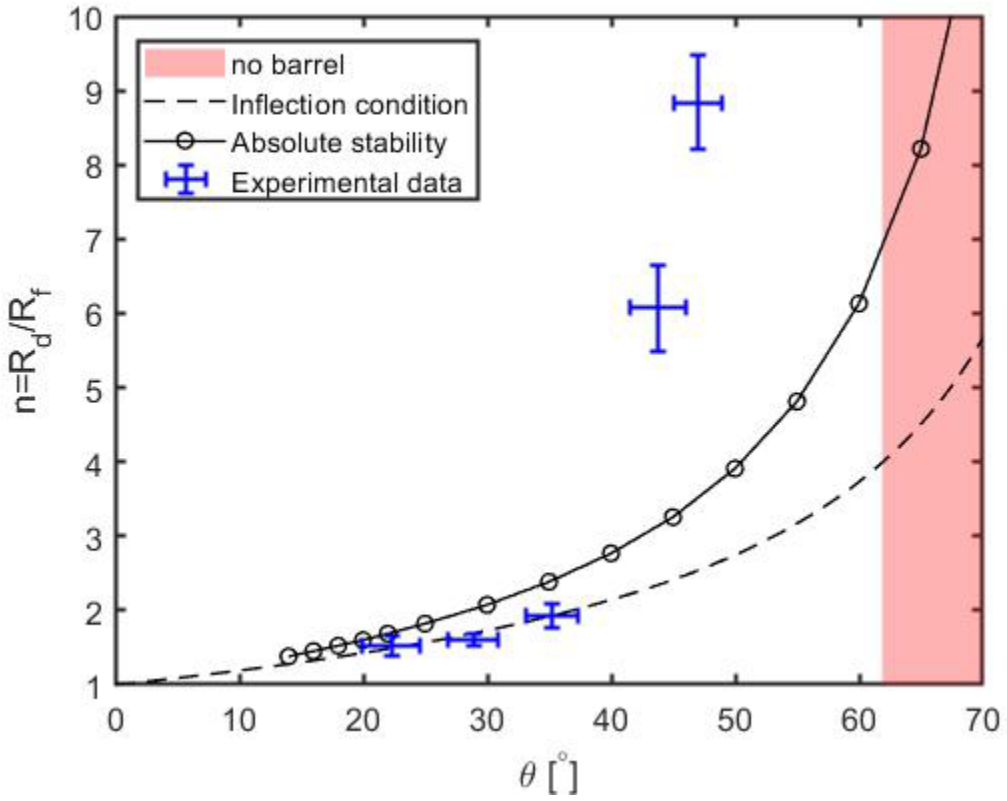

Fig. 3.14 The phase diagram showing the transition boundary between the barrel and clamshell drop: (1)The dashed curve represents the inflection point condition[14], (2)the circles represent the absolute stability criterion[21], and (3)the blue crosses formed by the error bars show the experimentally observed dimensionless radius n of the critical barreled drop. The red shadow area indicates the no barreled drop region.

Table 3.2 shows the estimated Bond number, $Bo = \frac{\rho g R_d^2}{\sigma}$, where ρ is the density of hexadecane, σ is the surface tension of hexadecane, R_d is the radius of critical barreled drop indicating the clamshell-barrel transition. We can see that the Bond number for all barrel-like drops during the experiments is much smaller than 1, meaning that the gravity should play no role during the transition process reported in this dissertation.

Table 3.2 Bond numbers formulated with R_d and R_f for critical barreled drops

Surface	Advancing CA[°]	Bond Number $Bo = \frac{\rho g R_d^2}{\sigma}$	$Bo = \frac{\rho g R_f^2}{\sigma}$
1	22 (2)	0.010	4.4×10^{-3}
2	29(2)	0.011	4.4×10^{-3}
3	37(2)	0.016	4.4×10^{-3}
4	44(2)	0.016	4.3×10^{-4}
5	47(2)	0.002	2.7×10^{-4}

The critical drop volume required for the transition can be evaluated as follows $V = V_d \times t_{transit} \times f$, where V_{drop} is the volume of a single drop printed by the nozzle, $t_{transit}$ is the time counted from the first drop printed to the capillary tube to the moment the transition is finished, and f is the printing frequency. Fig. 3.15 plots the dimensionless critical transition volume, $V^{\frac{1}{3}}/R_f$, versus advancing contact angle.

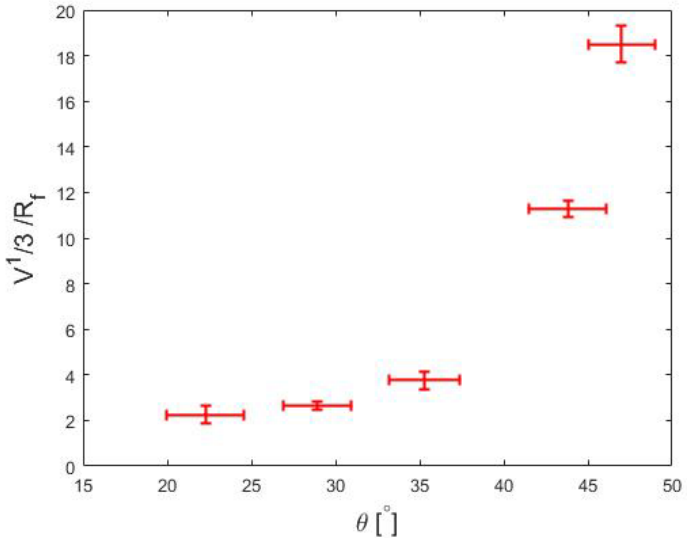

Fig. 3.15 Dimensionless critical transition volume versus advancing contact angle

The experiments reveal that the transition phenomena are virtually different due to the magnitude of the contact angles. When the contact angle is small, the transition from clamshell to barrel needs more time. A large contact angle brings in a new observation of the "rolling over" effect which has never been observed at small contact angles.

Investigating all barrel drops in Fig. 3.13, we notice that the barreled drops are always slightly asymmetric, in accord with the results reported in Refs. [17, 24]. In the recent publication[24], the authors suggested that the nearly asymmetric barrel drops can be explained be perturbation of axisymmetric droplets by gravity. Although the explanation was confirmed on experiments with the polyalphaolefin (PAO4) on fibers with the radii of 128, 221, and 600 μm, we can not completely agree with this explanation. The authors limited themselves only to the zero contact angle case (no explanation on how they measured this angle were provided). To follow their definition of the Bond number, we added the column $Bo = \rho g R_f^2/\sigma$ in Table 3.2. Our experiments were conducted at the Bond numbers much smaller than those in the Ref[24]. According to the theory, the smaller the Bond number, the smaller should be the drop asymmetry[24]. Thus, our experiments with extremely small Bond numbers should show less asymmetry. However, in in Fig 3.13(d) and Fig 3.13(e) we see that the more asymmetric drops correspond to the smaller Bond numbers. Thus, the required trend is not there. Moreover, if the gravity causes this asymmetry, then the bottom side of the asymmetric drop should be always

greater than the top side, which is clearly not true in our experiments in Fig. 3.10 and Fig. 3.11.

It is instructive to see that in all cases, the contact line of the clamshell drop was pinned during the clamshell-barrel transition. The liquid moved from clamshell to cover the dry side of the tube while the initial clamshell shrank to form another half of the barrel drop. The observation of the coexistence of spreading and gathering behavior of droplet with the pinned contact line suggests that the contact angle hysteresis should be responsible for this asymmetry.

In order to prove that, we investigated the contact angles of the top half and bottom half of the critical barreled drop. Fitting the drop profile next to the contact line with a second-order polynomial function, as shown in Fig. 3.16 we than inferred the contact angles.

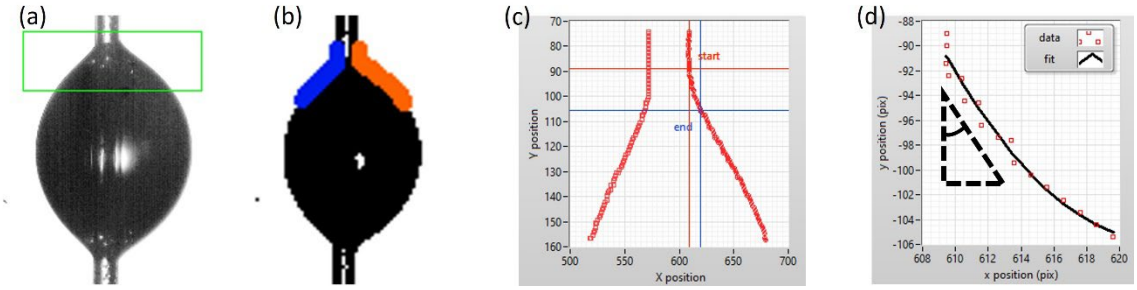

Fig. 3. 16 (a)Selected region at the contact line. (b)Binarized image and extracted meniscus profiles. (c)The position of contact line has been specified and 10 pixels wide band for profile fitting was determined. (d)The second polynomial is applied to fit the profile and its derivative at the contact line gives the best-fit angle of $47°$.

In Table 3.3, we collect the measured contact angles for the top and bottom sides of droplets. For convenience, we specify the fiber side where the clamshell was sitting before the transition. Compared to the contact angle values measured by K100 Force Tensiometer and the image analysis, we conclude that the top side of the barreled drop always shows the contact angle close to the advancing contact angle, while the bottom side shows the contact angle close to the receding contact angle. This confirms that the contact angle hysteresis contributes to the drop asymmetry.

Table 3.3 Contact angles measured on both sides of the asymmetric barrel drop.

silane	Advancing CA[°]	Top CA[°]	Receding CA[°]	Bottom CA[°]
2-[Methoxy(Polyethyleneoxy)6-9propyl]trimethoxysilane	22±2	23±2	18±3	17±2
Methacryloxypropyltrimethoxy silane	29±2	31±1	19±3	19±2
UNTREATED TUBES	35±2	33±2	27±1	22±2
n-Octyldimethylchlorosilane	44±2	46±2	34±2	36±2
Basalt fiber	47±1	47±2	32±2	37±3

3.3 Drop formation from liquid films coating the fiber

In another scenario, we coat the fiber with a thin film of the wetting liquid (0 s in Fig. 3.17). The liquid film will first form a "dumbbell" (1.5 s in Fig. 3.17) due to the Plateau-Rayleigh instability[27-29], and then two sides of the "dumbbell" gather into a zero contact angle barrel drop (3.4 s in Fig. 3.17). The transition from a barrel-like drop to a

clamshell drop (3.4 s to 20.0 s in Fig. 3.17) was observed due to a small liquid volume or a large contact angle. The transition will not happen with a larger volume or small receding contact angle. In contrast to the scenario of drop deposition, the drop is formed from the liquid film and when it forms, it keeps contracting; therefore, the receding contact angle is reported in this scenario.

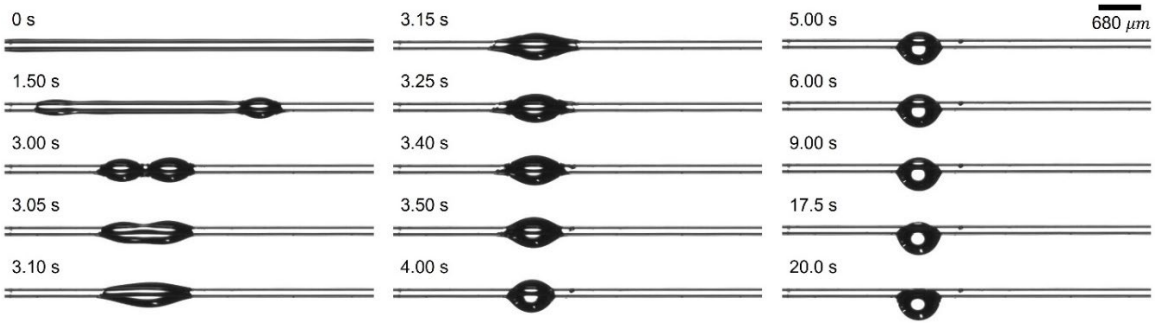

Fig. 3.17 A glycerol thin film is deposited on a capillary tube of $2R_f = 170\ \mu m$ *diameter. Then the film undergoes the Plateau-Rayleigh instability leading to formation of a barreled drop. The drop keeps gather the liquid from the film until the film breaks. Finally, the barreled drop is collected at the bottom as a clamshell. Glycerol makes* $60°$ *receding contact angle with the capillary tube.*

3.3.1 Experimental setup

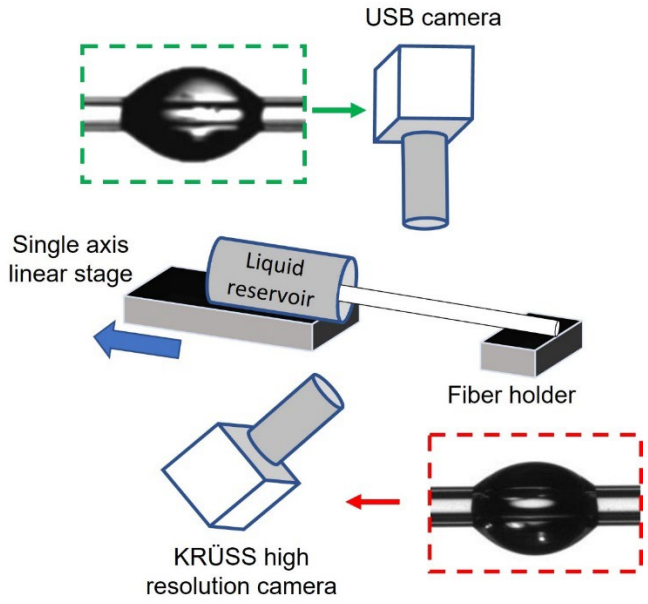

Fig. 3.18 Schematic of the experimental setup for fiber coating experiments.

The experimental setup for studying the second scenario is sketched in Fig. 3.18. A capillary tube was fixed on the stage to be withdrawn horizontally from the liquid reservoir attached to a single-axis linear stage (SMC Pollux Microstep Controller). To deposit a liquid film that is thick enough for formation of a big liquid barrel, we used pure viscous glycerol (Glycerin 99.7%, Laboratory Reagent, VWR Chemicals BDH®). The inner surface of the reservoir was chosen wettable, allowing us to trap the liquid inside it when we kept the tube horizontal. The high-resolution camera of KRÜSS Drop shape analyzer was used to record the drop formation and its transition to clamshell (the red box in Fig. 3.18), while a USB camera (Neewer® digital microscope) was set to confirm the shape

from another perspective (shown as the green box in Fig. 3.18). The receding contact angles between coated tubes and glycerol were measured using the K100 Force Tensiometer (KRÜSS) at a constant low speed of 0.3 mm/min to eliminate the effect of viscous force. The results are given in Table 3.4.

Table 3.4 The contact angle between glycerol and capillary tubes.

tube O.D.[mm]	**Silane**	**Receding CA[°]**
0.25	2-[Methoxy(Polyethyleneoxy)6-9propyl]trimethoxysilane	25 ± 2
0.25	UNTREATED TUBES	28 ± 2
0.25	Methacryloxypropyltrimethoxy silane	38 ± 1
0.25	(3-Glycidyloxypropyl)trimethoxysilane	40 ± 3
0.17	n-Octyldimethylchlorosilane	60 ± 2

3.3.2 Results and discussions

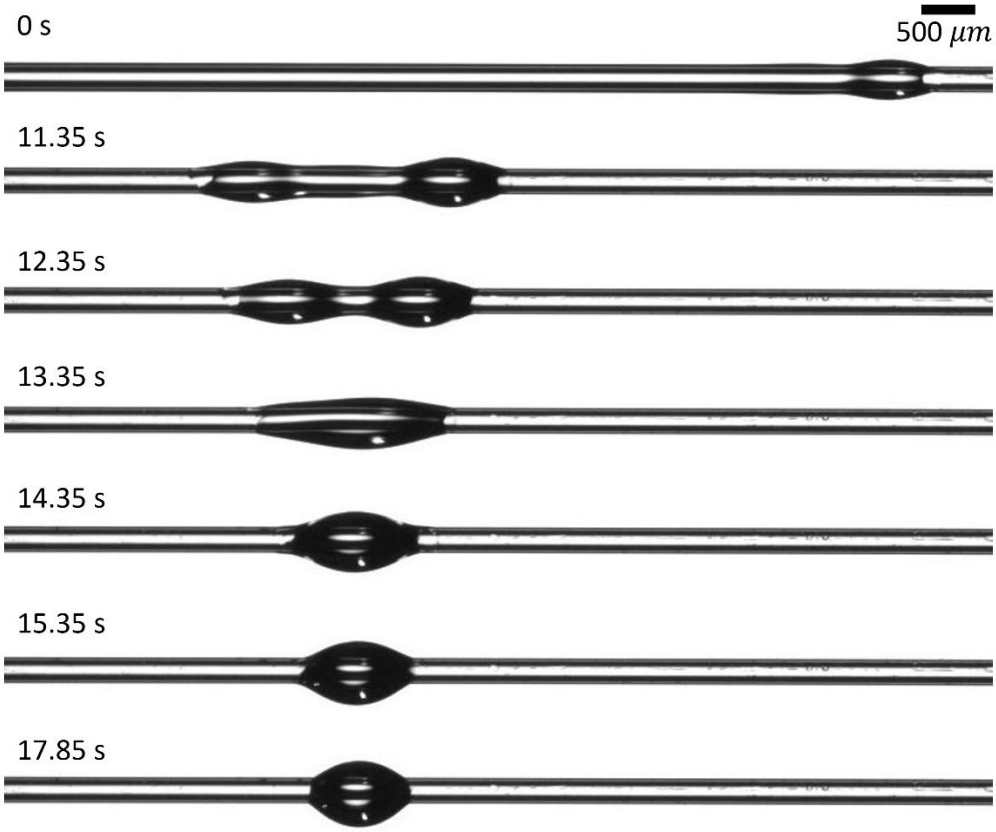

Fig. 3.19 A glycerol film is deposited on a capillary tube of $2R_f$ =250 μm diameter. Then the film forms a barreled drop. Glycerol makes $40°$ receding contact angle with the capillary tube.

Figure 3.19 illustrates the dynamics of drop formation from a thin glycerol film. We noticed that all deposited liquid would be collected in the drop without visible residue on the tube. The coating process was conducted at constant speed of a constant coating speed of V = 3.15 mm/s. The same fiber should provide the same coating thickness h. By decreasing the coating distance at constant coating velocity V, we can decrease the

amount of deposited liquid on the fiber. For example, if the coating length is L, the expected volume of the barreled drop would be $2\pi R_f\ L\ h$. Thus, starting from the largest barrel, we decreased the coating length by moving the fiber through the liquid filled tube to a shorted distance, decreasing the coating length by e=300 microns each time. Thus, we will obtain a series of barreled droplets of volumes reduced by $2\pi R_f(L-e)\ h$ each time. Figure 3.20 shows the drop configuration on the fiber at a receding contact angle of $40°$. Dimensionless drop size R_d/R_f decreases from 2.786 to 2.454 as the coating length decreases from 11.5 mm to 7.9 mm. The clamshell drop will be obtained when the coating distance is smaller than 7.9 mm. In Fig. 3.21, each observed barreled drop is marked as a red hollow circle.

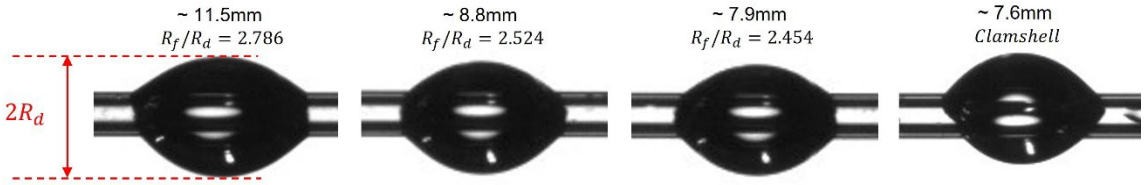

Fig. 3. 20 Liquid body configuration varies on the fiber as the coating distance decreases. The last drop is about to turn in a clamshell

The results of these experiments are summarized in the phase diagram in Fig. 3.21. For each receding contact angle, the data point with the lowest n where the barreled drop can be found refers to the transition boundary. Figure 3.22 summarizes the shape of the barreled drops obtained from the film coating experiments. In these experiments,

the shape of the barreled drops is much more symmetric, suggesting that the effect of contact angle hysteresis can be neglected.

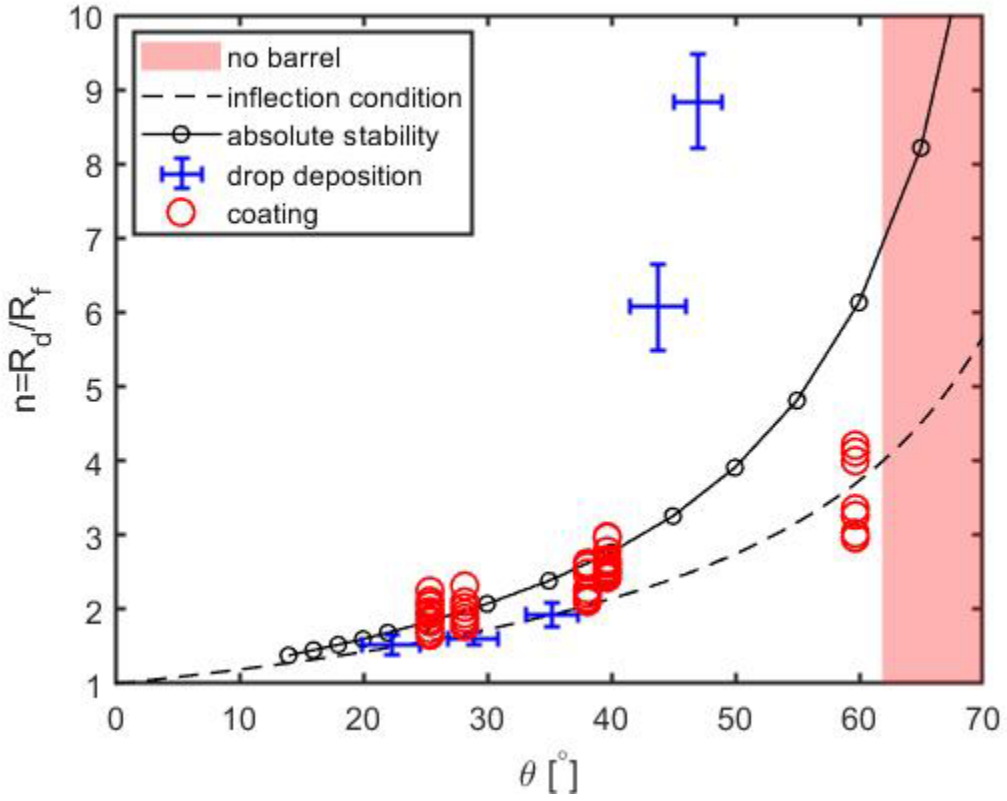

Fig. 3.21 The phase diagram showing the transition boundary between the barrel and clamshell drop: (1)The dashed curve represents the inflection point condition[14], (2)the circles represent the absolute stability criterion[21], and (3)the blue crosses formed by the error bars show the experimentally observed dimensionless radius n of the critical barreled drop. (4) The boundary of barreled drops observed in the fiber coating experiments. The red shadow area indicates the no-barreled-drop-region.

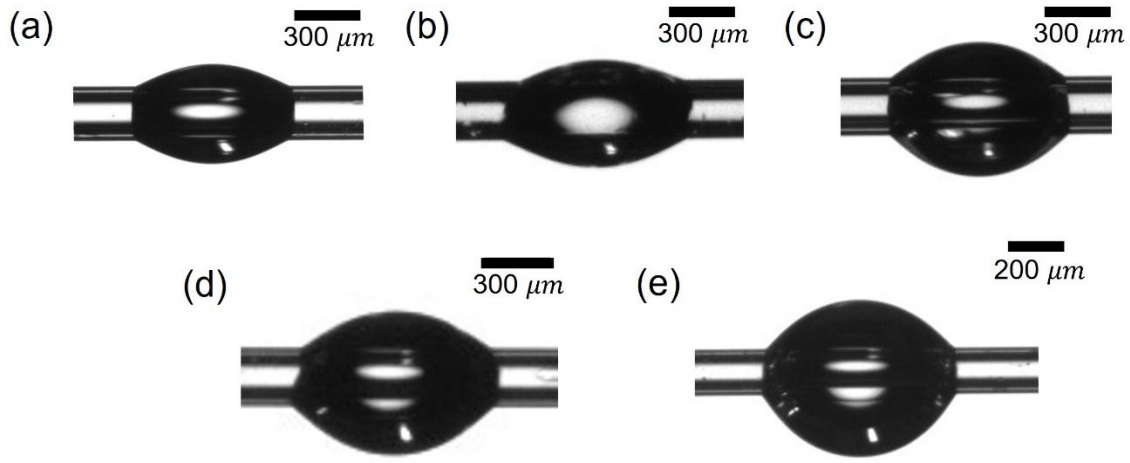

Fig. 3.22 Barreled drops formed on tubes at different receding contact angles. (a) $\theta_{rec} = 25°$. *(b)* $\theta_{rec} = 28°$. *(c)*$\theta_{rec} = 38°$. *(d)* $\theta_{rec} = 40°$.*(e)* $\theta_{rec} = 60°$.

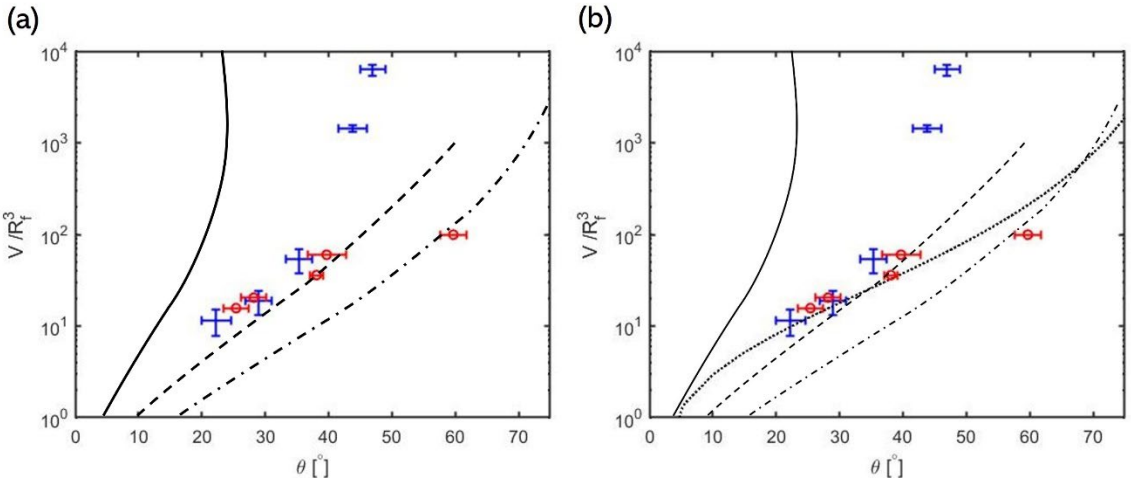

Fig. 3.23 (a)Three boundaries are roughly superimposed from Ref[10]: (1) solid curve, numerically determined stability limit of the clamshell. (2) broken curve, numerically determined the barrel shape stability limit. (3) dashed line, the condition of equal absolute energy of both states. Blue crosses are experimental data of drop deposition on fiber recalculated from Fig. 3.15. Red circles with the error bar are calculated using the equation (2.26) with known contact angle and ratio ɳ (the lowest red circle for each angle in Fig. 3.21). (b) The dots added to Fig. 3.23(a) show the boundary calculated at the inflection condition.

Comparing the data from the drop deposition experiment with the coating experiment in Fig. 3.21, we observe two distinguishing boundaries for clamshell-barrel transition and barrel-clamshell transition, which was first reported by Mugele's group[10]. In Fig. 3.23, we reproduce the diagram from Ref[10]; our data are added to the diagram for cross-comparison. The solid curve indicates the stability limit of the clamshell determined by Mugele's group numerically with Surface Evolver, which was confirmed by their experimental data. The broken curve indicates the numerically determined stability limit of the barrel shape. The dashed line indicates the condition of equal absolute energy of both states, which was also confirmed by their electrowetting experiments. Different from the reported phase diagram, our data suggest that these two scenarios coincide at small contact angles ($< 40°$) and then begin deviating from one another. We suspect that the difference is caused by the applied potential difference and buoyancy in the experiments conducted in Ref[10].

3.4 Conclusion

In this chapter, we experimentally studied the transition between clamshell and barreled drops on fibers. It is shown that critical conditions of transition from clamshell drop to barrel drop deviated from all the existing predictions. When the advancing contact angle is larger than $40°$, the clamshell drop requires significant volume to turn into a barrel drop, and the transition cannot happen when the contact angle is larger than $60°$. Investigating the transition process and analyzing the contact angles on the transited asymmetric barreled drops, we proposed that the contact angle hysteresis is responsible

for the drop asymmetry. On the other side, the drops formed from the coating films, undergo transition to clamshells when the inflection point criterion is satisfied. The barreled drops show nice symmetry in this case. The drop radius R_d, advancing contact angle θ_{adv} and receding contact angle θ_{rec} are the main parameters controlling the droplet shape.

3.5 References

1. Adamson, A.W. and A.P. Gast. *Physical chemistry of surfaces*. 1997.
2. Adam, N.K., *Detergent Action and its Relation to Wetting and Emulsification.* Journal of the Society of Dyers and Colourists, 1937. **53**(4): p. 121-129.
3. Cassie, A.B.D., *Physics and textiles.* Reports on Progress in Physics, 1945. **10**: p. 141-171.
4. Miller, B., *The wetting of fibers*, in *Surface characteristics of fibers and textiles*, M.J. Schick, Editor. 1977, Marcel Dekker: New York. p. 417-445.
5. Duprat, C., *Moisture in Textiles.* Annual Review of Fluid Mechanics, 2022. **54**: p. 443-467.
6. Quere, D., *Fluid coating on a fiber.* Annual Review of Fluid Mechanics, 1999. **31**: p. 347-384.
7. Opell, B.D., *Water harvesting during orb web recycling.* Journal of Arachnology, 2020. **48**(3): p. 278-283.
8. Opell, B.D., et al., *Tuning orb spider glycoprotein glue performance to habitat humidity.* Journal of Experimental Biology, 2018. **221**(6).
9. Stellwagen, S.D., B.D. Opell, and M.E. Clouse, *The impact of UVB radiation on the glycoprotein glue of orb-weaving spider capture thread.* Journal of Experimental Biology, 2015. **218**(17): p. 2675-2684.
10. Eral, H.B., et al., *Drops on functional fibers: from barrels to clamshells and back.* Soft Matter, 2011. **7**(11): p. 5138-5143.
11. Seeber, M., et al., *Surface grafting of thermoresponsive microgel nanoparticles.* Soft Matter, 2011. **7**(21): p. 9962-9971.
12. Carroll, B.J., The Accurate Measurement of Contact-Angle, Phase Contact Areas, Drop Volume, and Laplace Excess Pressure in Drop-on-Fiber Systems. Journal of Colloid and Interface Science, 1976. **57**(3): p. 488-495.
13. Carroll, B.J., Equilibrium conformations of liquid drops on thin cylinders under forces of capillarity. A theory for the roll-up process. Langmuir, 1986. **2**(2): p. 248-250.

14. McHale, G., et al., *Wetting of a High-Energy Fiber Surface.* J Colloid Interface Sci, 1997. **186**(2): p. 453-61.

15. McHale, G. and M.I. Newton, *Global geometry and the equilibrium shapes of liquid drops on fibers.* Colloids and Surfaces A: Physicochemical and Engineering Aspects, 2002. **206**: p. 79-86.

16. McHale, G., M.I. Newton, and B.J. Carroll, *The shape and stability of small liquid drops on fibers.* Oil & Gas Science and Technology-Revue De L Institut Francais Du Petrole, 2001. **56**(1): p. 47-54.

17. Chou, T.H., et al., Equilibrium phase diagram of drop-on-fiber: coexistent states and gravity effect. Langmuir, 2011. **27**(7): p. 3685-92.

18. Xu, C.W., Z.Y. Lu, and L.R. Li, Surface Evolver Simulation of Droplet Wetting Morphologies on Fiber Without Gravity. Frontiers in Energy Research, 2022. **9**.

19. Rebouillat, S., B. Letellier, and B. Steffenino, *Wettability of single fibres – beyond the contact angle approach.* International Journal of Adhesion and Adhesives, 1999. **19**(4): p. 303-314.

20. McHale, G., M.I. Newton, and B.J. Carroll, *The shape and stability of small liquid drops on fibers.* Oil & Gas Science and Technology-Revue D Ifp Energies Nouvelles, 2001. **56**(1): p. 47-54.

21. McHale, G. and M.I. Newton, *Global geometry and the equilibrium shapes of liquid drops on fibers.* Colloids and Surfaces A: Physicochemical and Engineering Aspects, 2002. **206**(1-3): p. 79-86.

22. Seeber, M., et al., *Surface grafting of thermoresponsive microgel nanoparticles.* Soft Matter, 2011. **7**(21): p. 9962-9971.

23. Carroll, B.J. and J. Lucassen, *Effect of surface dynamics on the process of droplet formation from supported and free liquid cylinders.* Journal of the Chemical Society, Faraday Transactions 1: Physical Chemistry in Condensed Phases, 1974. **70**(0): p. 1228-1239.

24. Gupta, A., et al., Effect of gravity on the shape of a droplet on a fiber: Nearly axisymmetric profiles with experimental validation. Physical Review Fluids, 2021. **6**(6).

25. Zhang, Z., F. Peng, and K.G. Kornev, The Thickness and Structure of Dip-Coated Polymer Films in the Liquid and Solid States. Micromachines, 2022. **13**(7): p. 982.

26. Alimov, M.M. and K.G. Kornev, *Meniscus on a shaped fibre: singularities and hodograph formulation.* Proceedings of the Royal Society a-Mathematical Physical and Engineering Sciences, 2014. **470**(2168).

27. Plateau, J., Experimental and theoretical researches on the figures on equilibrium of a liquid mass withdrawn from the action of gravity, in Annual Report of the Board of Regents of the Smithsonian Institution 1863, Smithsonian Institution: Washington, DC. p. 207–285.

28. Rayleigh, L., *On the capillary phenomena of jets.* Proc. R. Soc. Lond. A, 1879. **29**: p. 71-97.

29. Haefner, S., et al., Influence of slip on the Plateau-Rayleigh instability on a fibre. Nat Commun, 2015. **6**: p. 7409.

CHAPTER IV

DROP-ON-DEMAND PRINTING USING A WIRE-IN-A-TUBE

4.1 Introduction

4.1.1 Introduction to the traditional inkjet printing techniques

Inkjet printing of materials is viewed as a versatile manufacturing technique, which has been widely used in applications ranging from graphic products to manufacturing of ceramics and tissue engineering[1-13]. The number of journal articles that mention "inkjet" is steadily increasing: 363 articles were published in 2002, and 3609 articles were published in 2015[14]. There are two conventional techniques of printing, generally known as extrusion[15, 16] and drop-on-demand (DOD) printing[17-22].

Though both extrusion/continuous inkjet printing (CIJ) and drop-on-demand (DOD) printing technologies, one can generate droplets with diameter from 10 to 150 μm. The DOD method offers smaller 10 to 50 μm diameter droplets[19]. In the most widely used DOD technologies, thermal or piezoelectric actuators[14] are employed, Fig. 4.1(a) and (b). The physical idea behind both thermal and piezoelectric actuation is the same: these generators aim to generate a pressure pulse and velocity transient to eject a short jet out of the nozzle. In thermal DOD printing, a heater (the red part in Fig. 4.1(a)) can heat the ink above its boiling temperature to make a bubble pushing the ink out of the nozzle. In a piezoelectric DOD generator, the impulse current forces the piezoelectric actuator (the green part in Fig 4.1(b)) to expand, compressing the ink inside the reservoir and pushing

the ink out from the nozzle[19, 23]. Both methods of drop ejection rely on the developed pressure gradient. Like a piston in a syringe pushing the liquid column (shown in Fig. 4.1(c)), either the nucleated bubble or piezoelectric crystal push the liquid from the cavity.

The Hagen-Poiseuille model[24] can be employed to estimate the pressure ΔP required to print highly viscous ceramic precursors of viscosity η from a cylindrical nozzle of radius r and length L:

$$Q = \frac{\pi r^4 \Delta P}{8\eta L} \quad . \tag{4.1}$$

In this application of the Hagen-Poiseuille law, Q is the rate of drop formation, which is the drop volume $V = \left(\frac{4}{3}\right)\pi R^3$ times the printhead frequency f, $Q = V \cdot f$. If one wants to print a highly concentrated ceramic precursor of viscosity $\eta = 10\ Pa \cdot s$, with a standard printhead having nozzle radius $r = 10\ \mu m$, nozzle length $L = 500\ \mu m$, at printing frequency $f = 20\ Hz$ and drop radius is about R~33μm, the required pressure drop is $\Delta P \sim 38\ atm$. This estimate reveals the problems of the existing DOD technologies with highly viscous inks, the printheads cannot generate such a big pressure over milliseconds. The greater the viscosity, the greater the required pressure. Thus, to print polymeric droplets or ceramic slurries, one needs to apply an extremely strong pressure drop. In some applications where a low viscous fluid is delivered at a very low flow rate but requires further atomization[21], traditional DOD techniques fail to produce droplets as needed.

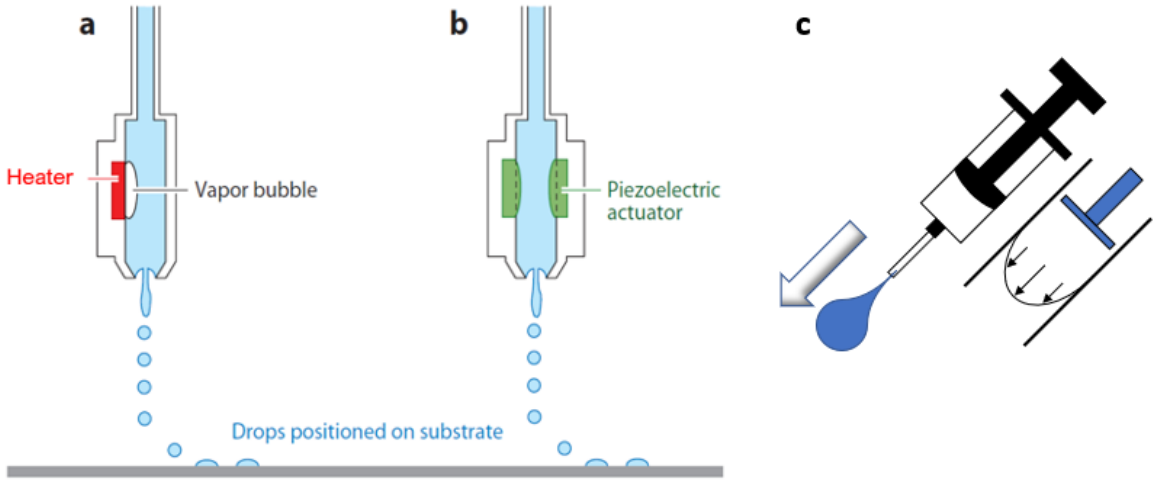

Fig. 4.1 Schematic diagram showing the working principles of the DOD inkjet printheads when the drops are ejected by a pressure pulse generated by (a) a nucleating bubble formed by the heater, (b) by a piezoelectric pusher - actuator[19]. c) A drop of ink is ejected by either a growing bubble or a deformed crystal. In both cases, the ink is displaced from the nozzle in a way similar to that of a pushing piston displacing an ink from a syringe[25]. (Reproduced from Ref[25], with the permission of AIP Publishing)

To speed up the printing process and increase printing resolution, electric-field assisted DOD printing has recently attracted interest [26-28]. The effect of electric field on drop detachment, flight, and spreading has not been studied systematically, especially in applications of printing of ceramics; however, an apparent interest to this field of remote-controlled manipulation of droplets and films generated a series of fascinating results [29-38]. The challenges with electroprinting of microdroplets of complex fluids have been summarized by Fenn in his Nobel Laureate Lecture [39].

4.1.2 Introduction to the drop formation process

Understanding the drop formation process is critical to improve the DOD techniques. With the help of a high-speed camera and the short duration (20 ns) flash illumination technique, one can observe the reproducible process of drop formation after a short jet has been ejected from the nozzle. One forms not a single drop but a drop and a liquid bridge connecting it with the ink reservoir, Fig. 4.2(a). A liquid bridge breaks up into several droplets when the drop leaves the nozzle. The breakup of the liquid bridge is caused by the surface tension[40], which is caused by the attraction of the particles in the surface tending to shrink into the minimum surface area. The liquid bridge is the key feature of conventional DOD inkjet printing and is inevitable for all these DOD inkjet printers[41]. Though some droplets formed after the bridge breakup have a trend to fly back to the reservoir, the others will follow the mother drop and land on the target, negatively affecting the sharpness of the print stamp. Therefore, the liquid bridge has to be broken on-demand, and satellite droplets deflected to achieve high-quality printing.

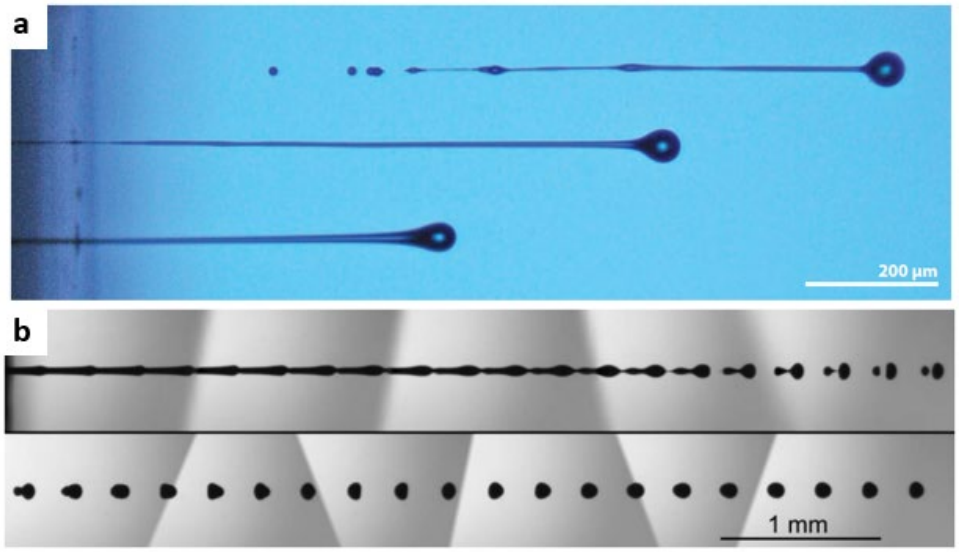

Fig. 4.2 (a) A high-speed photograph showing three drops ejected from three DOD printheads with a fixed short time delay illustrating different stages of drop formation through breakup of the liquid bridge[23]. (b) Composite stroboscopic image showing the breakup of a continuous jet traveling from left to right, the lower image being a continuation of the upper image[23].

In recent years, the breakup of different liquid materials has been studied, mostly focusing on the collapse of a filament of viscous and viscoelastic materials[42, 43]. For example, Fig. 4.2(b) displays a continuous ink jet being forced to break up into regular drops following the Plateau-Rayleigh scenario for the breakup of low viscous jets[40, 44]. The spatial periodicity of resulting droplets is very attractive for engineering applications. As the complexity and multi-functionality of the ink materials increase, the existing theories and engineering practices fall short of predicting the drop formation phenomena. Therefore, understanding of the breakup process of complex liquid materials becomes important.

4.1.3 Limitation of traditional DOD printing

In the DOD printing, the parameters of interest are the drop detachment speed V and the drop radius R. As mentioned earlier, fluid viscosity η and fluid surface tension σ influence both parameters V and R for the DOD printing. Intuitively, the high viscosity of the ink may hinder printability, resulting in low V, while the low surface tension of the ink may cause the appearance of satellites preventing sharp distribution of R.

To summarize the feasibility to print materials using DOD printing, the following metric has been introduced: the Weber number, defined as $We = \frac{\rho R V^2}{\sigma}$, where ρ is the ink density and the Reynolds number $Re = \frac{\rho R V}{\eta}$. The Weber number describes the effect of inertia in relation to surface forces and the Reynolds number describes the effect of fluid inertia in relation to viscous forces[14, 19]. The derivative of the Weber and Reynolds numbers, the Ohnesorge number, defined as $Oh = \frac{\sqrt{We}}{Re} = \frac{\eta}{\sqrt{\rho R \sigma}}$ is sometimes more convenient to deal with.

The conditions for liquid printability have been studied theoretically and experimentally[18, 19, 45, 46]. When the inequalities $We > 1$ and $Re < 1$ hold, the surface tension is believed to be less important than inertia, and inertial forces are less important than the viscous ones. When Oh is too small ($Oh < 0.1$), the formation of satellites in low viscous fluids has been reported implying that the surface forces defeat the viscous ones. When Oh is too large ($Oh >> 1$), the viscous force hinders the formation of a short jet (as illustrated in Fig. 4.2(a)). For instance, if we want to print a

drop of $2R = 100\ \mu m$ in diameter with the ink of $\eta = 5\ Pa \cdot s$, $\rho = 1000\ kg/m^3$ and $\sigma = 30\ mN/m$, then $Oh \approx 90$, which is far away from the printable range for the existing DOD printheads, Fig. 4.3(a). Different formulations of inks are summarized in Fig. 4.3(b) and Table 4.1.

In summary, all existing DOD inkjet printheads are limited to the low-viscosity inks (see Fig. 4.3(a) and Fig 4.3(b))[19], while the demand for the sol printing and polymer printing is increasing significantly. Neither extrusion nor DOD printing technology is capable of printing all range of liquids. For example, the DOD printing is limited to the low viscous fluids with the 3.5-12 $\mathrm{mPa \cdot s}$ viscosity range[19, 22, 47]. In contrast, micro-extrusion requires highly viscous fluids with viscosity ranging from $30\ \mathrm{mPa \cdot s}$ to > $6 \times 10^7\ \mathrm{mPa \cdot s}$[48].

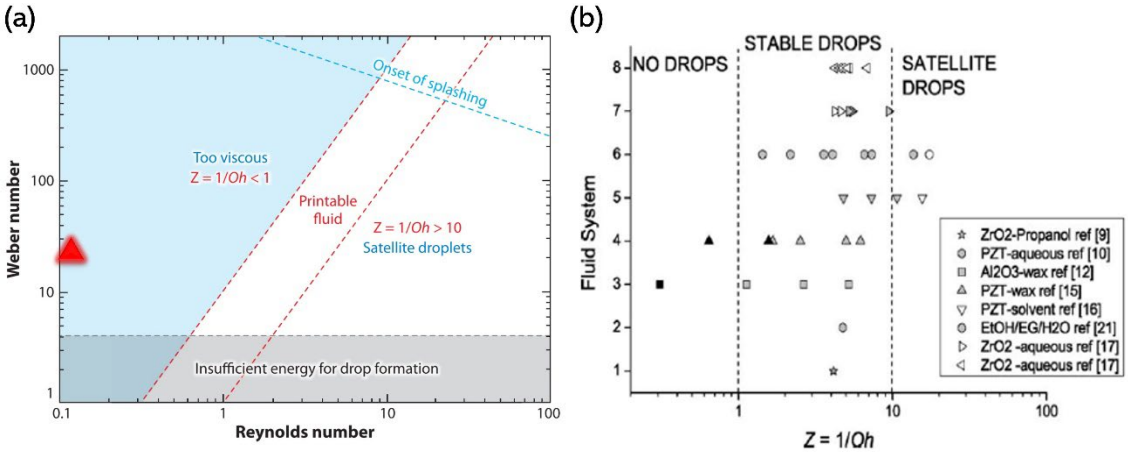

Fig. 4.3 (a) The printability diagram for different regimes of ink behavior in DOD inkjet printing. The red triangle specifies the range of parameters where we want to print with. (Adapted from Ref[19], with the permission of ANNUAL REVIEWS.) (b) The Fromm's parameter[45], $Z = 1/Oh$ is an important factor for the DOD printing materials. The dashed boundaries are the limits for material printability as proposed in

Ref[46]. The grey symbols correspond to successfully printed materials, the black symbols indicate that no drops can be produced, and the white symbols indicate the presence of satellites. (Adapted from Ref[18], with the permission of Elsevier.)

Table 4.5 Summary of physical properties and dimensionless numbers for each liquid. (Adapted with permission from Ref[49]. Copyright 2009 American Chemical Society.)

solvent type (volume fraction)	density (Kg/m^3)	viscosity (mPa·s)	surface tension (mN/m)	Reynolds number (N_{Re})	Weber number (N_{We})	inverse (Z) of Ohnesorge number (Oh)
ethylene glycol (0.15) + water (0.85)	1059	3.11	54.8	51.08	8.69	17.32
ethylene glycol (0.25) + ater (0.75)	1068	3.69	47.8	43.42	10.07	13.68
ethyl alcohol (0.75) + ethylene glycol (0.25)	866	4.83	28.9	26.89	13.47	7.32
ethylene glycol (0.5) + water (0.5)	1094	7.61	45.8	21.56	10.76	6.57
ethylene glycol (0.75) + water (0.25)	1106	12.3	45.6	13.49	10.91	4.08
glycerol (0.66) + Water (0.33)	1172	16.05	56.2	10.95	9.37	3.57
diethylene glycol (0.5) + water (0.5)	1111	22.0	41.4	7.58	12.08	2.17
diethylene glycol	1118	35.1	44.8	4.78	11.23	1.43

[a] Droplet diameter and its travel velocity are assumed to be 50 μm and 3 m/s, respectively.

4.1.4 Wire-in-a-tube idea

A new electroprinting principle has been developed, replacing a nozzle-based DOD generator with a wire-in-a-nozzle drop generator[28, 50]. Compared with the traditional needle-based DOD generator, the developed device can print single droplets ranging from 50 to 500 μm using the same nozzle with different wires. In the original wire-in-a-nozzle drop generator published in Ref[28], the authors used a syringe pump as the driving force of the fluid delivery system. Instead of printing the drop immediately after the drop formation, a weak-bias electric field was applied to deliver the drop to the end of the wire first, and then the drop was pulled toward the target by the electric field. The following has been proven true according to the observations of the authors: using a fine wire as the printhead instead of a relatively large needle to detach the drop, one can efficiently avoid nozzle clogging caused by high viscosity of the ink and the satellites owing to the

low surface tension of some inks. The results also indicate that the size of the wire is very critical to the printing[28].

4.1.5 Motivation

The most challenging task for the existing technologies, especially in polymer, biomaterials printing[51, 52], and ceramic printing[15], is to print single microdroplets of a viscous fluid with a narrow drop-size distribution. Many scientific and industrial applications require DOD generation of a droplet with the size starting from 50 μm and ending at 1000 μm. However, none of the existing conventional printing technologies, extrusion/continuous inkjet printing (CIJ) and drop-on-demand (DOD), can print highly viscous materials in the form of drops. To address this challenge, a new wire-in-a-tube electroprinting principle has been developed where the electric field is proposed to detach and guide the drop to a target. The existing prototype can print single droplets of complex fluids. For instance, we succeeded in printing single droplets of pure glycerin having a surface tension comparable to that of water and viscosity of about 1000 times greater than that of water; the droplets range in diameters from 14 μm to 440 μm.

4.2 Materials characterizations

4.2.1 Shear viscosity

In the study of the surface phenomenon and fluid dynamics, such as droplet formation and droplet transition, the physical properties of the fluid are particularly important: density ρ, fluid surface tension σ, viscosity η. The characterization of these properties is always the first thing that needs to be finished prior to any other experiments. What's

more, these values are essential for material scientists and engineers to estimate the feasibility of microfluidic devices for a given material.

For the convenience of analysis, we usually model and describe the phenomenon in scalable systems by introducing dimensionless numbers. The following characteristic numbers play crucial roles in studying droplet manipulations throughout the whole dissertation[14, 19].

Figure 4.4 shows the relation between shear viscosity (η) and strain rate ($\dot{\gamma}$) for Newtonian and non-Newtonian fluids described by the formula $\eta = m\dot{\gamma}^{n-1}$ where m is the consistency of the material and n is the power low index; m and n are constants for a given polymer at a specific temperature. For shear-thinning fluids, viscosity decreases as the strain rate increases; for shear-thickening fluids[53, 54], viscosity increases as the strain rate increases.

The knowledge of the correct dependence of viscosity on specific strain rate at the given temperature is critical for designing inks for materials engineering applications.

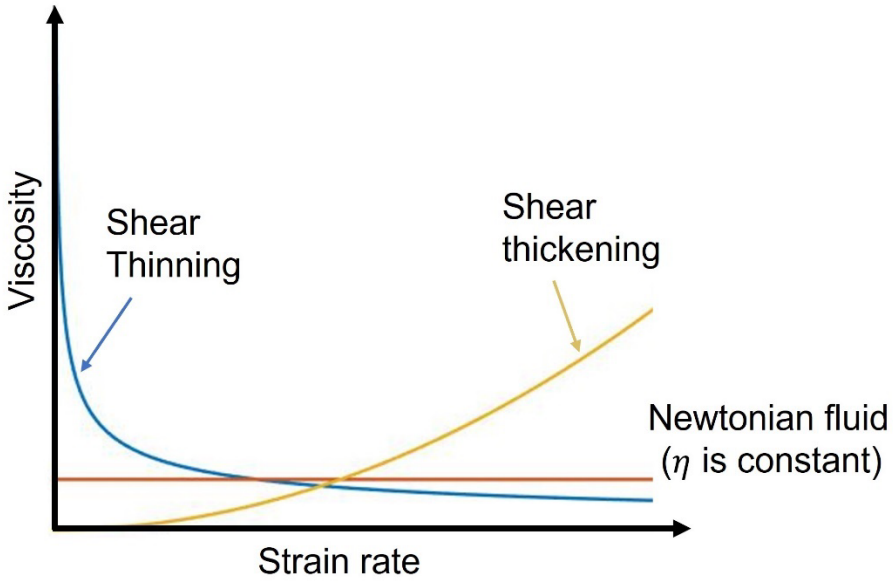

Fig. 4.4 Relation between viscosity and strain rate for Newtonian and non-Newtonian fluids: viscosity is constant for Newtonian fluids; the two other curves show shear-thinning and shear-thickening behavior of non-Newtonian fluids.

Since the shear viscosity of fluids is sensitive to the strain rate and temperature, special care needs to be taken to characterize the rheological properties of these complex materials. In the following, we use the Ba-Ce-Fe (BCF) sol, an advanced ceramic precursor recently developed in Dr.F.Peng group [55], as a working example to show the complexity of real materials. The density of this sol was measured at 1.28 g/cm^3 and the surface tension was determined at 37.4 mN/m with KRÜSS 10 drop shape analyzer at room temperature. The highly concentrated BCF sol was prepared by the following procedure.

The molar ratio between metal ions and 2,4-pentanedione (ACAC) was 1:4. All materials in Table 4.2 were added to a boiling flask and were dissolved in acetic acid at

room temperature by vigorously stirring for 30 minutes. The solution was then refluxed at 90^{o}C for 5 hours in an oil bath. After cooling down to room temperature, 36 ml DI water was added into the solution for hydrolysis. The pH of the obtained solution was then adjusted to 2.10 by HNO_3, and then set in an 80^{o}C oven until viscous sols were obtained. The viscosity of the sol was tested over time. In this dissertation, the highly viscous BCF sol was obtained by concentrating the solution in the 80^{o}C oven for 65 hours.

Table 4.6 Composition list of Ba-Ce-Fe-based solution

Amount	Chemicals	Supplier
50 ml	Acetic acid, Glacial Reagent	Aqua Solutions, Inc.
7 ml	Ammonium hydroxide solution, 28.0-30.0% NH3 basis	Sigma-Aldrich
4.04 ml	2,4-Pentanedione, 99%	Alfa Aesar
19 ml	DI water	N/A
0.01 mol (2.554 g)	Barium acetate	Alfa Aesar
0.005 mol (1.7214 g)	Cerium (III) acetate sesquihydrate, 99.9%	Alfa Aesar
0.005 mol (2.02 g)	Iron (III) nitrate nonahydrate, 98+%	Alfa Aesar

The shear viscosity of this sol was measured using the Brookfield DV3T cone-plate Rheometer. We first ran the measurement at room temperature without the water circulation bath. The measured shear viscosity drops with the shear rate suggested materials shear thinning behavior (see red line in Fig. 4.5(a)).

Since BCF is a newly developed material, the rheological properties were unknown before our measurements. To ensure the accuracy of the first report on this advanced ceramic cursor, we introduced a real temperature monitor system to the shear viscosity

measurement, as shown in Fig. 4.6. The thermocouple was connected with the water circulator via a T-shaped tube (see Fig. 4.6(a)) to obtain the most accurate temperature of the sample by measuring the real-time temperature of the outlet circulating water of the sample cup (Fig. 4.6(b)).

With the water circulation bath connected to the rheometer and the thermocouple, we can eliminate the influence of temperature change on the results. Measurements with controlled sample temperature showed that the shear viscosity remains constant (see the black line in Fig. 4.5(a)). Changing the temperature and running experiments multiple times, one observes that even a slight increase of temperature (up to 8 ℃) results in almost one order of magnitude drop of viscosity (from 11000 $mPa \cdot s$ to 2800 $mPa \cdot s$). We suggest that the viscous dissipation is responsible for heating up the liquid during rheological experiments leading to an apparent shear thinning behavior (see Fig. 4.5(b)).

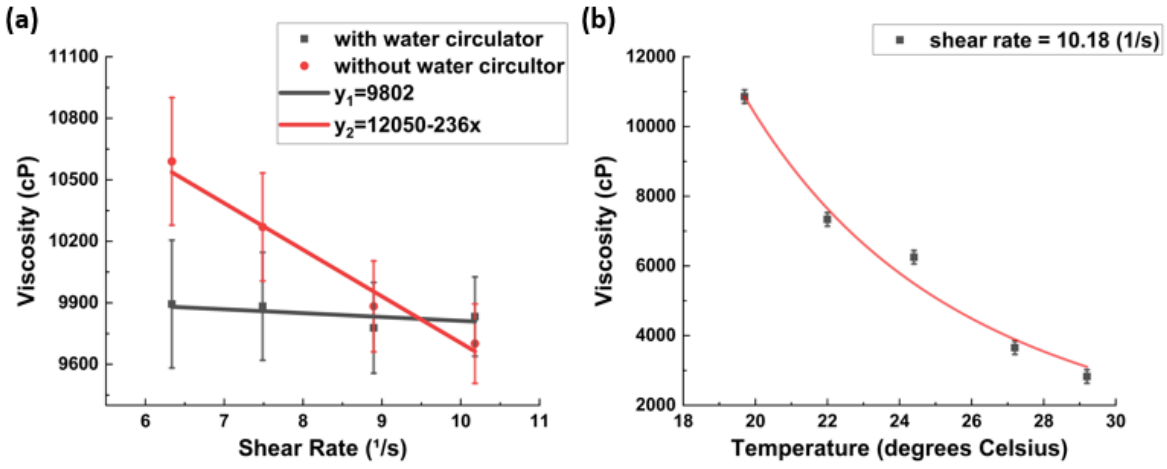

Fig. 4.5 Every single point represents the average of one series of viscosity measurements: (a) viscosity of BCF versus shear rate; (b) viscosity of BCF versus temperature at a fixed shear rate of 10.18 s^{-1}.

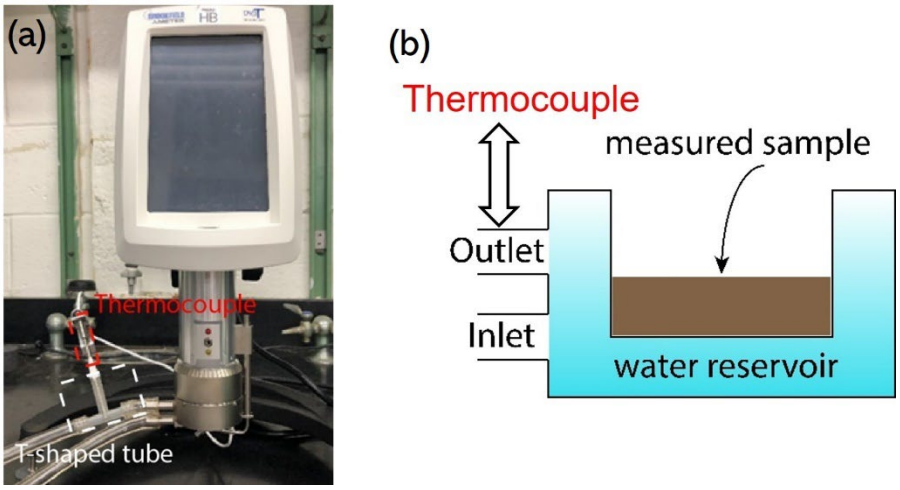

Fig. 4.6 (a) DV3T rheometer with a thermocouple. (b) Schematic of the two-layer sample cup.

4.2.2 Extensional rheology

The image sequences in Fig. 4.7 show the drop detachment process, which is the key step of the printing process, indicating that the neck formation is caused by a diverging flow of material from the neck to the periphery of the liquid bridge. This is the pure extensional deformation, and we model it by stretching the liquid drop placed between two disks of a magnetic stretcher following the evolution of the radius change of the resulting liquid bridge, as sketched in Fig. 4.8. Fig. 4.9 shows the liquid bridge breakup of the pure glycerol solution, and Fig 4.10 shows the liquid bridge breakup of the BCF sol.

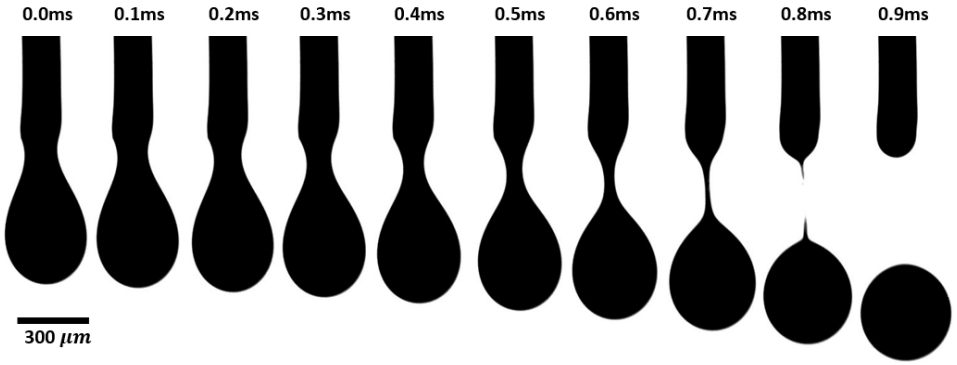

Fig. 4.7 An image sequence filmed at 10000 fps illustrates the detachment of a BCF droplet pulled by the electrostatic field.

For Newtonian viscous fluids, the neck of the liquid bridge decreases linearly with time[43]. For viscoelastic Maxwell fluids, fluid elasticity stabilizes cylindrical filament over the time comparable with the relaxation time τ_r. The radius of the cylindrical filament decreases exponentially with time, and the decay constant is proportional to the relaxation time of the liquid[56].

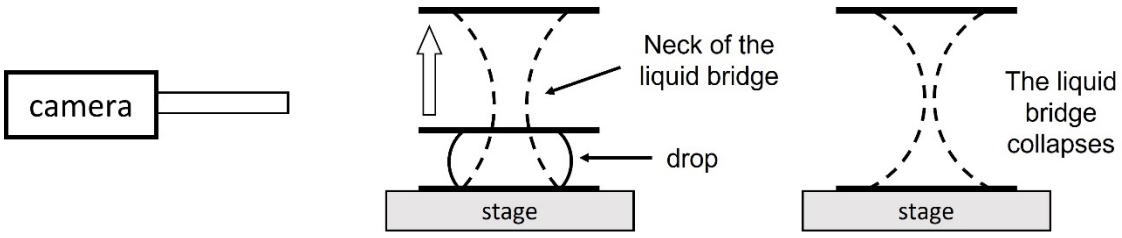

Fig. 4.8 Schematic of experiment on the breakup of the liquid bridge. The drop is placed between two disks and the upper magnetic disk is lifted up by applying a magnetic field. This way, the drop is stretched, forming a liquid bridge.

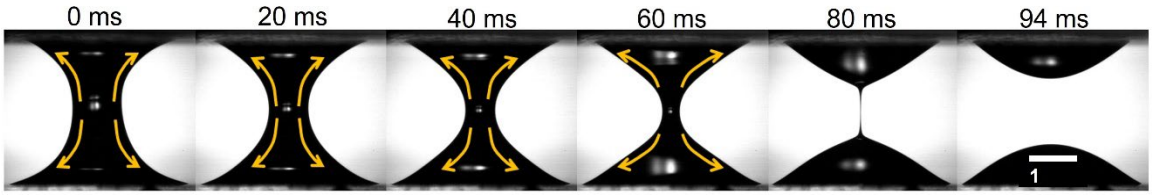

Fig. 4.9 evolution of the liquid bridge of pure glycerol with time. Yellow arrows indicate the direction of the flow inside the liquid bridge

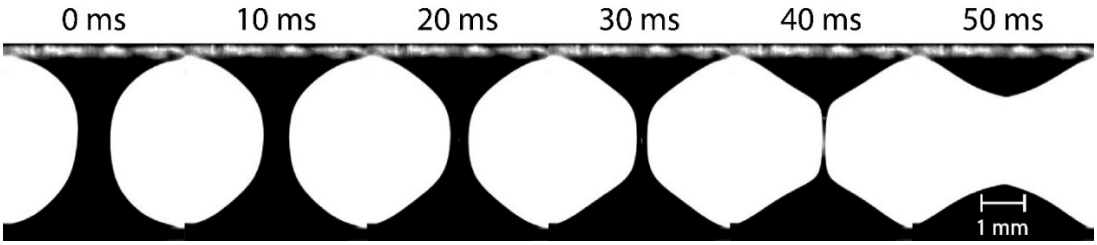

Fig. 4.10 evolution of the liquid bridge of BCF with time

The radius of the neck can be extracted using a LabView program. For a Newtonian ink, the relation between the neck radius and time is given by the following equation[43],

$$R = R_0 - 0.0709\frac{\sigma}{\eta}t \tag{4.2}$$

Where, R_0 is the initial radius, t is the collapse time, and η is the extensional viscosity.

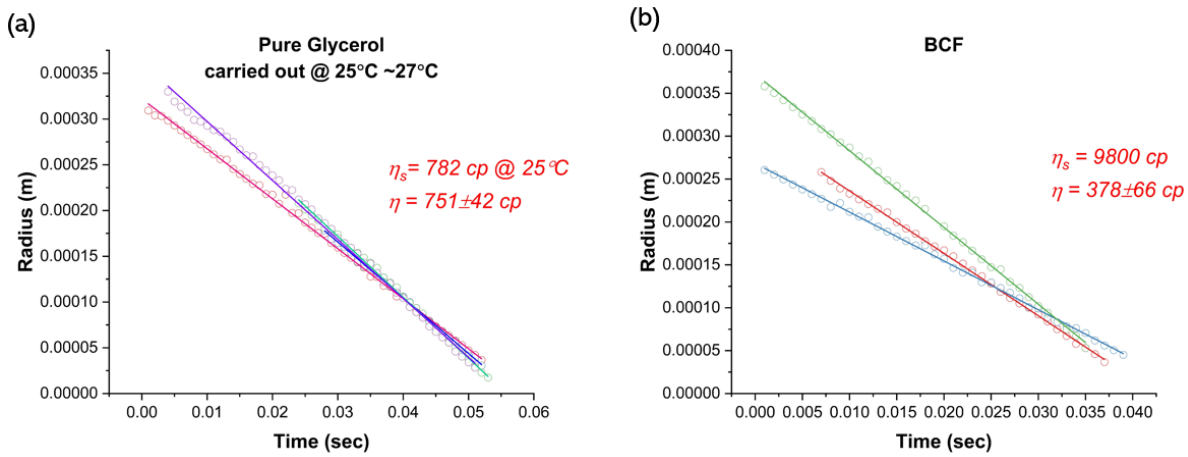

Fig. 4.11 Neck radius as a function of time: (a) shows the fitting results for pure glycerol, the extensional viscosity is $751 \pm 42\ mPa \cdot s$*; (b) shows the average fitting for BCF, the extensional viscosity is* $378 \pm 66\ mPa \cdot s$*.*

As shown in Fig. 4.11 (a), the glycerol as a standard Newtonian viscous solution follows the theoretical prediction that the extensional viscosity ($751 \pm 42\ mPa \cdot s$) is equal to the shear viscosity (782 $mPa \cdot s$). Surprisingly, the linearity of radius vs. time dependence for BCF (see Fig. 4.11(b)) indicates that the BCF sol behaves as a purely viscous fluid, yet its extensional viscosity drops significantly compared to its shear viscosity, from the shear viscosity of 9800 cp to the extensional viscosity of 378 $mPa \cdot s$. The working hypothesis for the deviation from the theoretical prediction is that the sol forms some internal network of bonds that break upon the liquid bridge's significant stretching.

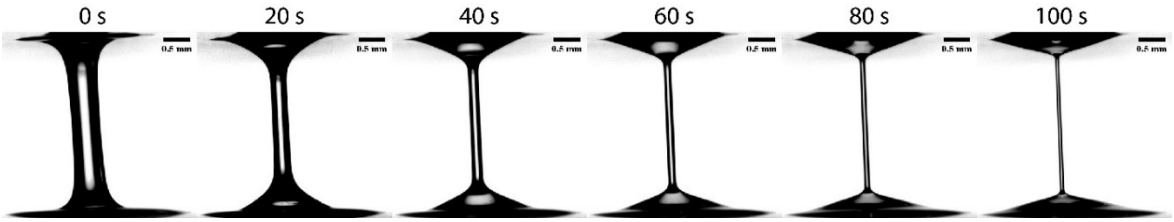

Fig. 4.12 Cylindrical filament variation with time

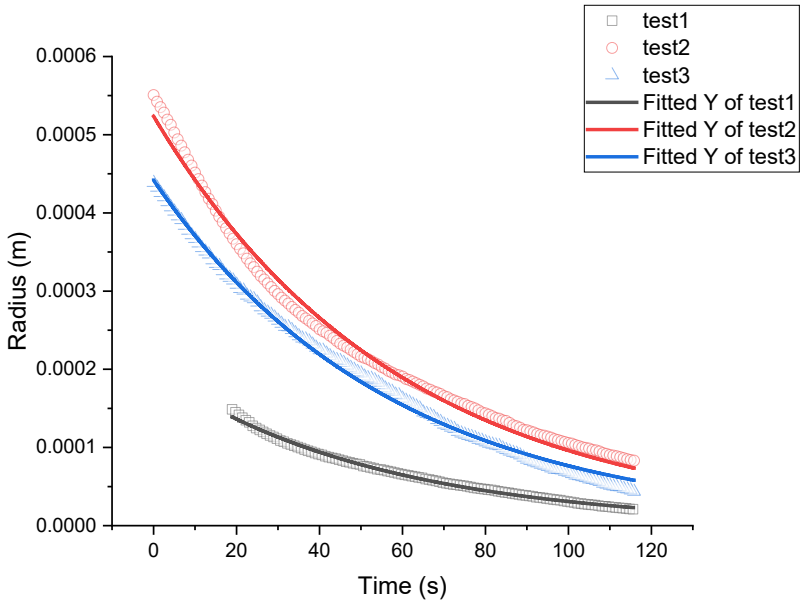

Fig. 4.13 Radius as a function of time

We ran the extensional viscosity measurement with a 20 wt.% solution of polybutadiene (Aldrich) in hexadecane (Sigma-Aldrich). Due to the high viscoelasticity of the solution, the thinning of a perfect cylindrical filament was observed during the experiments, as shown in Fig. 4.13. For viscoelastic Maxwell fluids, the radius of the cylindrical filament decreases exponentially with time, of which relation obeys the following equation,

$$R = R_0 \cdot exp\left(\frac{-t}{3\tau_r}\right) \tag{4.3}$$

Where, R_0 is the initial radius of the cylindrical filament, t is the collapse time, and τ_r is the relaxation time.

Figure 4.13 plots the extracted radius of cylindrical filament as a function of time using the hollow symbols, and the solid curve corresponds to the best fit of the Maxwell model

to the experimental data. The average stress relaxation time of this polymer solution was determined at $18.88 \pm 0.87\ s$.

4.3 Prototype of the wire-in-a-tube drop generator

The design details of the printhead of the current wire-in-a-tube drop generator is shown in Fig. 4.14, and the photograph of the experimental setup is shown in Fig. 4.15(a). A tungsten wire (Advent Research Materials Ltd) with a mechanical pusher driven by a programmable power supply (Instek PSS-2005 GP) and a pulse generator (BNC Model 505 pulse/delay generator) are the key components of the drop generator. The tail of the wire is connected to the positive pole of a D.C. high voltage supply (GLASSMAN HIGH VOLTAGE, INC) while the collector is connected to the ground. As shown in Fig. 4.15(b), to protect the control system and magnets from the high voltage source, a cone filled with epoxy serving as an insulator connects the tungsten wire to the shaft. Refer to Fig. 4.14, two induction coils (part 2), a permanent magnet (part 3), a spring (part 4), and a shock absorber (part 5) are mounted on a frame (part 1). The slide way (part 6) can ensure that the tungsten wire (part 9) is moving vertically with the needle (or shaft, part 7). The permanent magnet is held above two induction coils holding the wire. The frame is mounted to a 3-dimensional linear stage.

The current flows through the coils when the pulse generator sends a single rectangular pulse. Meanwhile, the magnet is pulled downwards and moves the wire through the ink-filled tube, which is embedded in the center of a Teflon plate serving as the reservoir. The wire remains its stick-out status until the signal turns from pulse peak

to trough, which is controlled by the input pulse repetition rate and pulse width. A spring (part 4 in Fig. 4.14) pulls the wire with the magnet back to its original position as soon as the current flow stops. The moving speed of the wire can be controlled by varying the output voltage of the power supply, i.e., the average speed is about 500 $\mathrm{mm/sec}$ when we keep the output voltage at 7 volts during the experiment.

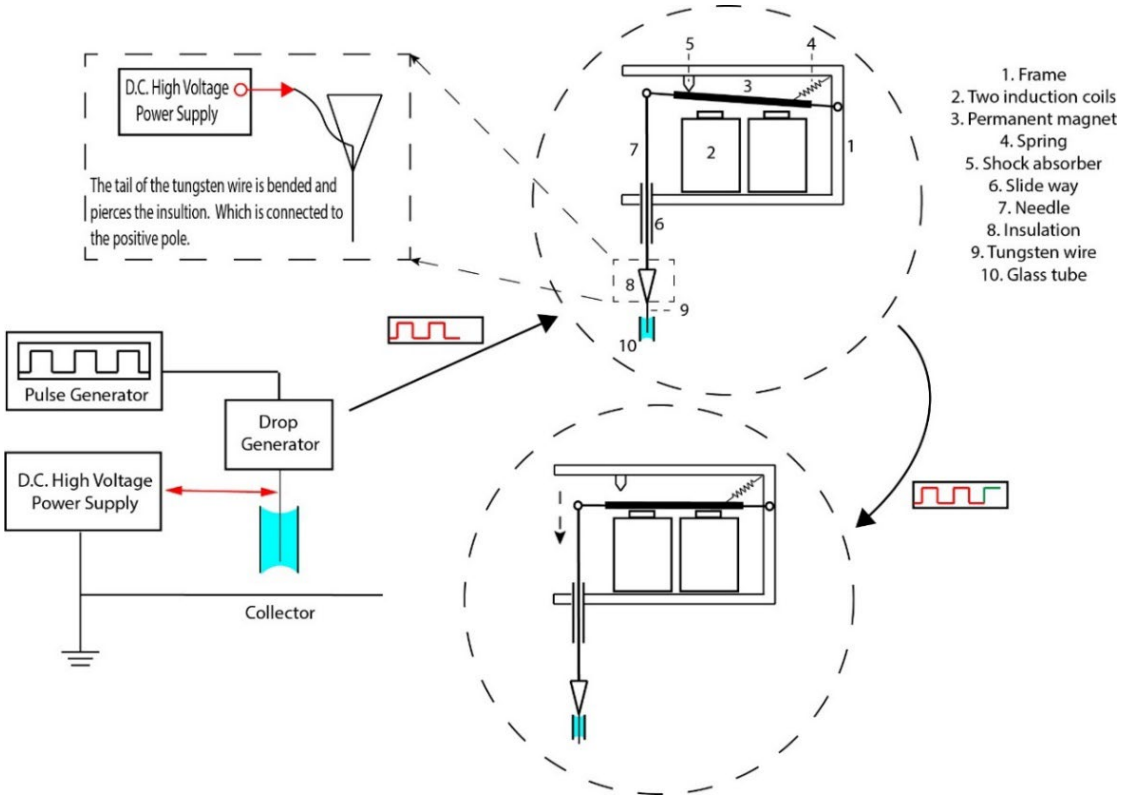

Fig. 4.14 Schematic of the printhead of the wire-in-a-tube drop generator, which is controlled by the pulse generator. Two induction coils (part 2), a permanent magnet (part 3), a spring (part 4), and a shock absorber (part 5) are mounted on a frame (part 1). The slide way (part 6) can ensure that the tungsten wire (part 9) is moving vertically with the needle (or shaft, part 7).

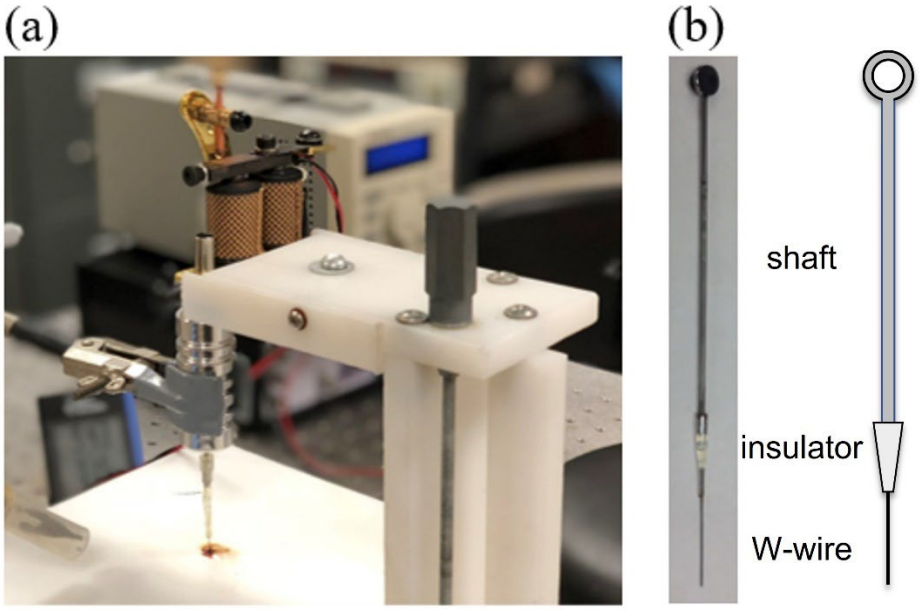

Fig. 4.15 (a) The wire-in-a-tube drop generator in the lab; (b) a tungsten wire is attached to a shaft by an insulator.

Fig. 4.16 shows the integrated wire-in-a-tube electroprinting system. The stability of the electric field is vital to the quality of print patterns in our drop generation system. Specifically, since the tip of a fine tungsten wire is used as the positive pole of the electric field, any joggling of the wire will change the trajectory of the flying droplets significantly and then cause the drop point off the prescribed position. To reduce the influence of wire vibration during printing, we only move the position of the collector(substrate) to obtain designed patterns instead of moving the wire-in-a-tube drop generator. On the other side, the stability of the electric field can be enhanced by improving the electrical insulation performance of the experimental setup. Therefore a sizeable Teflon plate is chosen to

hold the tube instead of a regular clamp to keep the tungsten wire away from any conductive material which may affect the electric field.

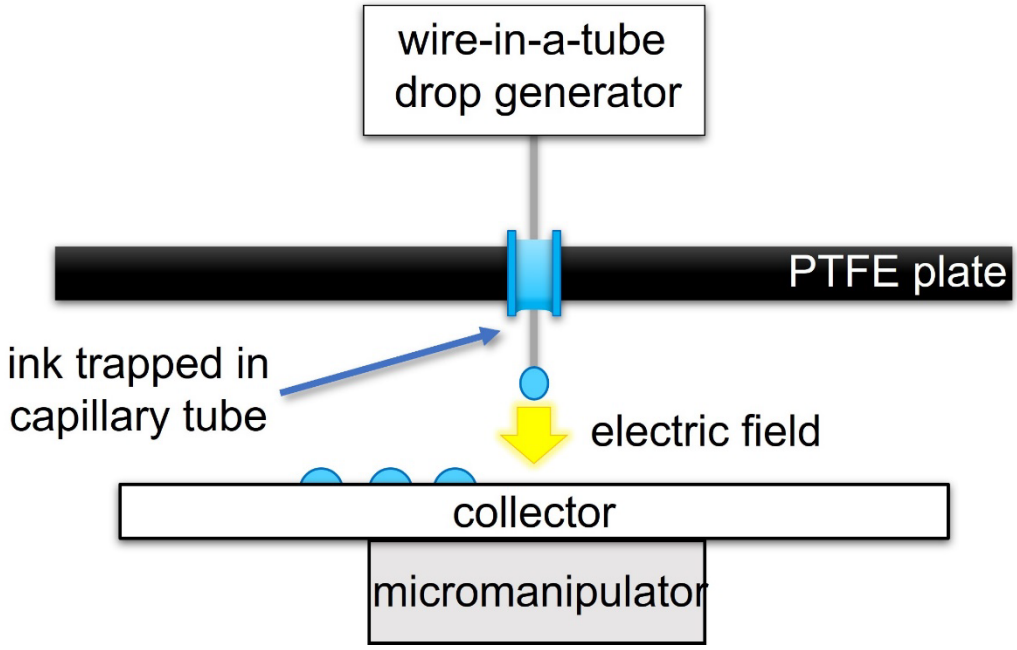

Fig. 4.16 Schematic of the integrated wire-in-a-tube electroprinting system: the wire-in-a-tube drop generator keeps printing droplets to the fixed position with the assistance of a stable electric field; users can obtain different print patterns by programming the micromanipulator.

4.4 Experimental results

4.4.1 Working principle of the wire-in-a-tube drop generator

Schematic of the experimental system is shown in Fig 4.17. It consists of a tube filled partially with the ink, a tungsten wire (Advent Research Materials Ltd) with a mechanical pusher driven by a programmable power supply (Instek PSS-2005 GP), and a pulse generator (BNC Model 505 pulse/delay generator). Both ends of the tube are open, so that the wire can move freely through the tube. A high speed-motion camera

(MotionProY4, Integrated Design Tools, Inc.) with a microscope (Navitar 1-60135) and a Halogen light source (F0-150, Fiberoptics Technology Inc) were used to record the process of drop formation on the wire.

The pusher moves the wire on demand with the frequency controlled by the pulse generator. Each cycle of the drop generation consists of four steps schematically pictured in Fig 4.17. In the initial position, the wire is secured inside the tube with its lower end completely submersed and positioned far away from the lower meniscus.

In the second step, the wire is forced to move out of the tube. On its way through the tube, the wire picks up the ink. When the wire reaches its terminal position, it is stopped there. The wire part that remains outside the tube introduces a very important design parameter which we call the stick-out length. The second step ends when a liquid cone connecting the wire tip with the tube edge forms.

In the third step, the wire remains in the same place and does not move. The liquid cone collapses first to form a cylindrical film. Then, due to the Plateau-Raleigh instability[57], this film is gathered into a single drop. When the drop forms, the third step ends.

In the fourth step, one can apply some force to remove the drop from the wire. For example, a D.C. voltage can be applied to the wire, forcing the drop nearest to the tip of the wire to move to the tip and then jump to the target[28]. When the drop leaves the wire, the fourth step ends.

After the end of the fourth step, the wire is pulled back to the initial position, and the cycle is repeated to generate the second drop and so on.

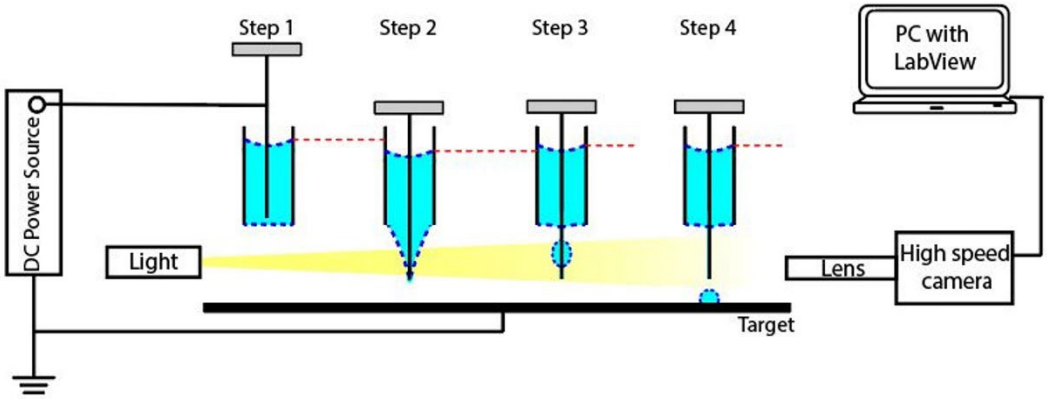

Fig. 4.17 The four main steps of drop formation. The first step: the wire is secured inside the tube, the second step: the wire moves out forming a liquid cone, the third step: the drop forms, and the fourth step: the drop is pulled from the wire by an applied electric field; the drop moves toward the target. (Reproduced from Ref[25], with the permission of AIP Publishing)

4.4.2 Critical voltage

In many electric-field-assisted printing methods, the electric field is applied to adjust the position of printed droplets or speed up the printing process; without electric field, these printers can still work. However, the D.C. field plays a much more critical role in our wire-in-a-tube DOD generator since the electrostatic force pulls the drop from the wire and attracts it to the target. Our DOD generator cannot print any droplets without applying electric field!

When the drop forms on the stick-out wire, a D.C. field of appropriate strength is needed to print the drop to the target. If the D.C. field is not strong enough, the drop comes to the wire end but does not necessarily leave the wire. If the D.C. field is too strong,

the Taylor cone[58] forms and further causes the failure of printing a single drop on demand. To get a single droplet printed on demand, one must apply a voltage slightly above a critical value to detach the drop from the wire.

The critical voltage is defined as the smallest voltage required to pull the drop from the wire. Decreasing the voltage about 0.1 kilovolts lower than the critical voltage, one guarantees that the drop will not leave the wire.

To investigate the critical voltage using in the wire-in-a-tube DOD generator, experiments were conducted with pure glycerol (Glycerin ≥99.7%, Laboratory Reagent, VWR Chemicals BDH®) and tungsten wires of five different diameters. Tungsten wires of diameters $d = 150\ \mu m, 100\ \mu m, and\ 50\ \mu m$ were purchased from Advent Research Materials Ltd, and the tungsten wires of diameters $d = 30\ \mu m, and\ 4\ \mu m$ were electropolished in the lab using the method of Ref[59]. The surface tension of glycerol was measured using KRÜSS DSA 10 and found to be $\sigma = 63.32 \pm 0.15\ mN/m$; Viscosity was measured by Brookfield DV3T Rheometer and found to be $\eta = 894.5 \pm 10.24\ mPa \cdot s$.

Fig. 4.18 illustrates the drop detachment process when we rose the D.C. voltage from a voltage 0.1 kV lower than the critical voltage to the critical voltage. The distance from the wire tip to the target was fixed at 1.0 cm. Fig. 4.18(a) and (b) show the static pendant drop at the tip when 2.2 kV was applied to the wire. The surface tension force working along the contact line was trying to keep the pendant drop at the tip; meanwhile, the electrostatic force acting on the drop was trying to pull the drop off the wire. Fig. 4.18(a)

and (b) clearly show that the drop did not move under the electric field. Immediately after, we rose the voltage to 2.3 kV, and then the drop started moving, as shown in Fig. 4.18(b)-(d). The red dashed line indicates the movement of the droplet. Eventually, in Fig. 4.18(e) and Fig. 4.18(f), the hanging drop detached from the wire and formed a spherical drop.

We notice that the second tiny drop may form on the wire next to the mother drop with a finer wire (the diameter of the wire is 100 μm Fig. 4.18). Whether the second drop will move with the first is a fatal application problem. The experiments reveal that the second unduloidal drop could hold its original position when the electric field forced the mother drop to leave the wire, see the blue dashed line in Fig. 4.18.

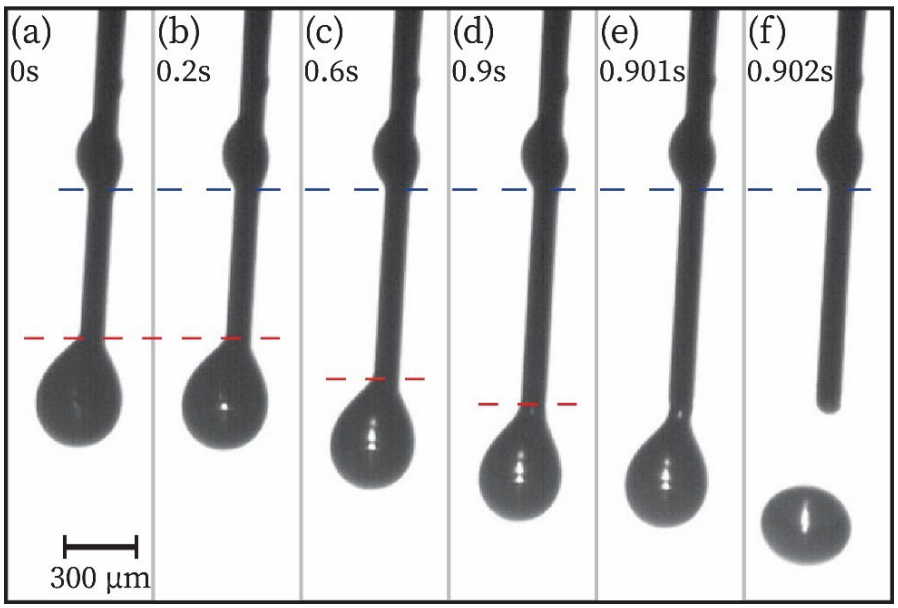

Fig. 4.18. (a) to (b) The pendant drop was at its critical condition when the applied voltage was 2.2kv. (b) to (f) when one rose the voltage to 2.3 kV, the pendant drop started moving and eventually detached from the wire. The distance from wire tip to target was 1.0 cm.

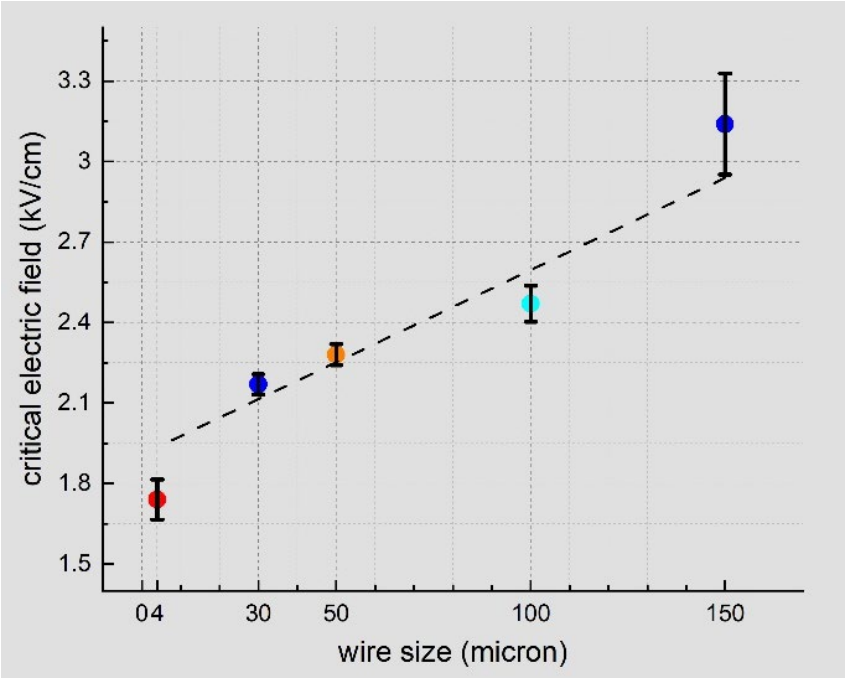

Fig. 4.19 The relation between the wire size and critical electric field

The strength of the critical electric field was tabulated as critical voltage (kV) divided by the distance from the end of the wire to the target plate (cm). A summary of experiments is given in Fig. 4.19. The graph suggests that the larger the wire diameter, the greater the critical electric field for the drop detachment, and a linear relationship can be observed.

4.4.3 How to control the size of droplets

We found that the printed drop size significantly changed with different wire diameters. In Fig. 4.20, we summarize the features of drop detachment from five different wires. The finer the wire the smaller the drop it generates. Fig. 4.20(a) to (d) show a

sequence of images recorded at 10,000 frames per second when the drop completely detached from the wire of diameter $d = 150\ \mu m, 100\ \mu m, 50\ \mu m, 30\ \mu m$, under critical electric fields. Since the shape of the flying drop is very close to spherical, we apply ImageJ to extract the area of the flying drop and then apply the formula $A = \frac{\pi d^2}{4}$ to estimate the drop diameter d. For the finest wire of diameter $d = 4\ \mu m$, the flying drop could not be filmed clearly due to the limitation of the lens. In such a case, we estimated the size of the flying droplet by fitting the tiny bulge with a circle (circled in Fig. 4.20(e)).

The results are concluded in Fig. 4.21 and suggest that the drop diameter linearly increases as the wire size increases. The slope of this linear fitting is close to 3. Furthermore, the standard deviation of the distribution of the drop sizes for each wire is relatively small, indicating that our DOD technology is reliable and capable of generating droplets in a narrow range of size distribution.

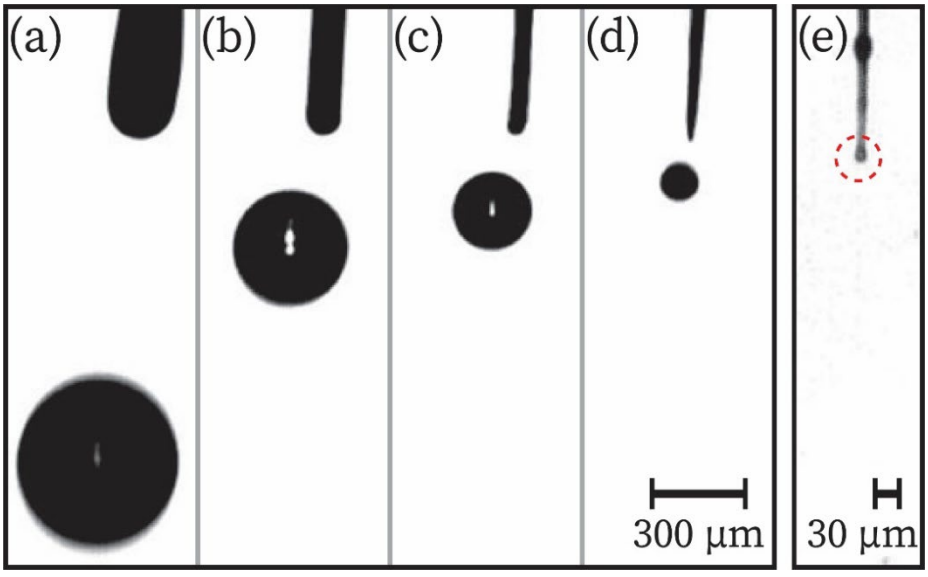

Fig. 4.20 (a) to (d) The moment when drop completely detached from the wire of 150 μm, 100 μm, 50 μm, 30 μm under critical electric fields. Videos were recorded at 10,000 fps. (e) The last moment before the drop detached from the wire of 4 μm radius. The droplet at the tip is estimated about 14 microns in diameter. Videos were recorded at 20,000 fps.

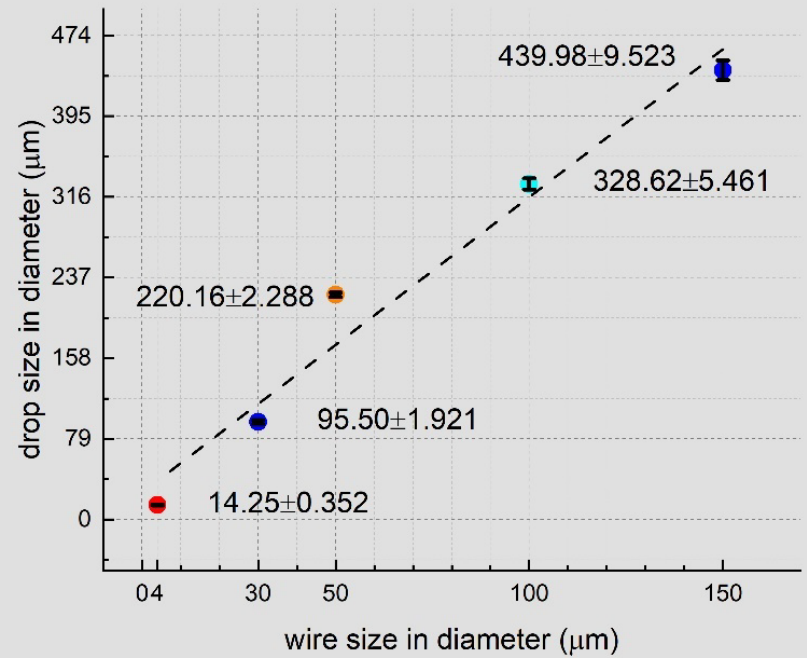

Fig. 4.21 Printed drop size versus wire size.

4.4.5 Printed patterns

To prove that the proposed wire-in-a-tube drop generator is sufficiently flexible for different applications, several patterns were printed using the BCF sol. Either a piece of tape or a silicon wafer was placed on a large metal plate connecting to the ground. The plate was mounted on a stage of a programmable micromanipulator (MP-285 Shutter instrument company). Before printing, we preset the moving route of the stage and the

moving speed to match the working frequency of the wire-in-a-tube DOD generator. Then the pattern in Fig. 4.22(a) and Fig. 4.22(b) were printed automatically. The diameter of droplets printed in Fig. 4.22(a) was smaller than 100 μm before impacting the substrate. Since the tape surface was not smooth, the dots in Fig. 22(a) were not perfectly circular. The printed pattern on a smooth silicon wafer was much more well-aligned, as shown in Fig. 4.22(b).

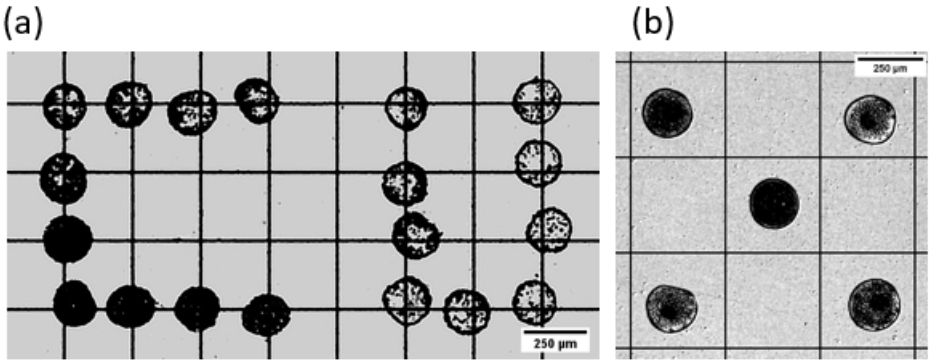

Fig. 4.21 (a) "CU" pattern printed from BCF sol on a tape; (b) five BCF dots printed on a silicon wafer.

4.5 Conclusion

In this chapter, we describe the challenges of the existing DOD techniques and introduce a novel wire-in-a-tube DOD generator. The video analysis results reveal a linear relationship between the critical electric field and the wire size and a linear relationship between the drop size and the wire size. Furthermore, the printing results show that our DOD technology is reliable for generating micron-size droplets with the narrow size distribution. Using this technique, we can print single droplets on demand from high viscosity ink. The estimation of the characteristic Ohnesorge number indicated that this

technique could be used to extend the regime of printability for existing DOD printers to the currently unreachable limits. For example, if we want to print a glycerol drop of $2R = 100\ \mu m$ in diameter, we have $\eta = 900\ cp$, $\rho = 1.258\ g/cm^3$ and $\sigma = 63.21\ mN/m$, then $Oh \approx 14.27$, which is considered non-printable for the existing DOD print-heads summarized in ref[18, 60].

4.6 References

1. Calvert, P., *Inkjet printing for materials and devices.* Chemistry of Materials, 2001. **13**(10): p. 3299-3305.
2. Williams, C., *Ink-Jet printers go beyond paper.* Physics World, 2006. **19**(1): p. 24-29.
3. Bharathan, J. and Y. Yang, Polymer electroluminescent devices processed by inkjet printing: I. Polymer light-emitting logo. Applied Physics Letters, 1998. **72**(21): p. 2660-2662.
4. Hayes, D.J., D.B. Wallace, and W.R. Cox, *MicroJet printing of solder and polymers for multi-chip modules and chip-scale packages.* 1999 International Conference on High Density Packaging and Mcms, Proceedings, 1999. **3830**: p. 242-247.
5. Seerden, K.A.M., et al., *Ink-jet printing of wax-based alumina suspensions.* Journal of the American Ceramic Society, 2001. **84**(11): p. 2514-2520.
6. Sirringhaus, H., et al., High-resolution inkjet printing of all-polymer transistor circuits. Science, 2000. **290**(5499): p. 2123-6.
7. Setti, L., et al., An amperometric glucose biosensor prototype fabricated by thermal inkjet printing. Biosens Bioelectron, 2005. **20**(10): p. 2019-26.
8. de Gans, B.J. and U.S. Schubert, *Inkjet printing of well-defined polymer dots and arrays.* Langmuir, 2004. **20**(18): p. 7789-7793.
9. Nakamura, M., et al., Biocompatible inkjet printing technique for designed seeding of individual living cells. Tissue Eng, 2005. **11**(11-12): p. 1658-66.
10. Murphy, S.V. and A. Atala, *3D bioprinting of tissues and organs.* Nature Biotechnology, 2014. **32**(8): p. 773-785.
11. Tekin, E., P.J. Smith, and U.S. Schubert, Inkjet printing as a deposition and patterning tool for polymers and inorganic particles. Soft Matter, 2008. **4**(4): p. 703-713.
12. Boland, T., et al., *Drop-on-demand printing of cells and materials for designer tissue constructs.* Materials Science & Engineering C-Biomimetic and Supramolecular Systems, 2007. **27**(3): p. 372-376.

13. Cui, X.F. and T. Boland, Human microvasculature fabrication using thermal inkjet printing technology. Biomaterials, 2009. **30**(31): p. 6221-6227.

14. Guo, Y., et al., Inkjet and inkjet-based 3D printing: connecting fluid properties and printing performance. Rapid Prototyping Journal, 2017. **23**(3): p. 562-576.

15. Chen, Z., et al., *3D printing of ceramics: A review.* Journal of the European Ceramic Society, 2019. **39**(4): p. 661-687.

16. Roy, M., et al., Composite Reinforcement Architectures: A Review of Field-Assisted Additive Manufacturing for Polymers. Journal of Composites Science, 2020. **4**(1).

17. de Gans, B.J., P.C. Duineveld, and U.S. Schubert, *Inkjet Printing of Polymers: State of the Art and Future Developments.* Advanced Materials, 2004. **16**(3): p. 203-213.

18. Derby, B., *Inkjet printing ceramics: From drops to solid.* Journal of the European Ceramic Society, 2011. **31**(14): p. 2543-2550.

19. Derby, B., Inkjet Printing of Functional and Structural Materials: Fluid Property Requirements, Feature Stability, and Resolution. Annual Review of Materials Research, 2010. **40**(1): p. 395-414.

20. Basaran, O.A., Small-scale free surface flows with breakup: Drop formation and emerging applications. Aiche Journal, 2002. **48**(9): p. 1842-1848.

21. De Bartolomeis, A. and A. Shokrani, Electrohydrodynamic Atomization for Minimum Quantity Lubrication (EHDA-MQL) in End Milling Ti6Al4V Titanium Alloy. Journal of Manufacturing and Materials Processing, 2020. **4**(3).

22. Raut, N.C. and K. Al-Shamery, *Inkjet printing metals on flexible materials for plastic and paper electronics.* Journal of Materials Chemistry C, 2018. **6**(7): p. 1618-1641.

23. Martin, G.D., S.D. Hoath, and I.M. Hutchings, *Inkjet printing - the physics of manipulating liquid jets and drops.* Journal of Physics: Conference Series, 2008. **105**.

24. Sutera, S.P. and R. Skalak, *The history of Poiseuille's law.* Annual review of fluid mechanics, 1993. **25**(1): p. 1-20.

25. Sun, Y., et al., Making droplets from highly viscous liquids by pushing a wire through a tube. Physics of Fluids, 2022. **34**(3).

26. Choi, J., et al., Drop-on-demand printing of conductive ink by electrostatic field induced inkjet head. Applied Physics Letters, 2008. **93**(19).

27. Nguyen, V.D. and D. Byun, Mechanism of electrohydrodynamic printing based on ac voltage without a nozzle electrode. Applied Physics Letters, 2009. **94**(17).

28. Andrukh, T., B. Rubin, and K.G. Kornev, *Wire-in-a-nozzle as a new droplet-on-demand electrogenerator.* Langmuir, 2011. **27**(6): p. 3206-10.

29. Collins, R.T., et al., Electrohydrodynamic tip streaming and emission of charged drops from liquid cones. Nature Physics, 2008. **4**(2): p. 149-154.

30. Basaran, O.A., H.J. Gao, and P.P. Bhat, *Nonstandard Inkjets*, in *Annual Review of Fluid Mechanics, Vol 45*, S.H. Davis and P. Moin, Editors. 2013. p. 85-113.

31. Arscott, S., *Electrowetting and semiconductors.* Rsc Advances, 2014. **4**(55): p. 29223-29238.

32. Espin, L., A. Corbett, and S. Kumar, *Electrohydrodynamic instabilities in thin viscoelastic films - AC and DC fields.* Journal of Non-Newtonian Fluid Mechanics, 2013. **196**: p. 102-111.

33. Hwang, W., et al., Electrospray deposition of polymer thin films for organic light-emitting diodes. Nanoscale Research Letters, 2012. **7**.

34. Jones, T.B., *An electromechanical interpretation of electrowetting.* Journal of Micromechanics and Microengineering, 2005. **15**(6): p. 1184-1187.

35. Mugele, F., M. Duits, and D. van den Ende, *Electrowetting: A versatile tool for drop manipulation, generation, and characterization.* Advances in Colloid and Interface Science, 2010. **161**(1-2): p. 115-123.

36. Nganguia, H., et al., Equilibrium electro-deformation of a surfactant-laden viscous drop. Physics of Fluids, 2013. **25**(9).

37. Roberts, S.A. and S. Kumar, *AC electrohydrodynamic instabilities in thin liquid films.* Journal of Fluid Mechanics, 2009. **631**: p. 255-279.

38. Zhu, T.J., et al., Electrospray Dense Suspensions of TiO2 Nanoparticles for Dye Sensitized Solar Cells. Aerosol Science and Technology, 2013. **47**(12): p. 1302-1309.

39. Fenn, J.B., *Electrospray wings for molecular elephants (Nobel lecture).* Angewandte Chemie-International Edition, 2003. **42**(33): p. 3871-3894.

40. Rayleigh, L., *On the capillary phenomena of jets.* 1879. **29**: p. 27.

41. Tyler, D.J., *Textile Digital Printing Technologies.* Textile Progress, 2005. **37**(4): p. 1-65.

42. McKinley, G.H. and T. Sridhar, *Filament-stretching rheometry of complex fluids.* Annual Review of Fluid Mechanics, 2002. **34**: p. 375-415.

43. McKinley, G.H. and A. Tripathi, How to extract the Newtonian viscosity from capillary breakup measurements in a filament rheometer. Journal of Rheology, 2000. **44**(3): p. 653-670.

44. Broedersz, C.P., et al., *Cross-Link-Governed Dynamics of Biopolymer Networks.* Physical Review Letters, 2010. **105**(23): p. 4.

45. Fromm, J.E., *Numerical-Calculation of the Fluid-Dynamics of Drop-on-Demand Jets.* Ibm Journal of Research and Development, 1984. **28**(3): p. 322-333.

46. Reis, N., C. Ainsley, and B. Derby, *Ink-jet delivery of particle suspensions by piezoelectric droplet ejectors.* Journal of Applied Physics, 2005. **97**(9).

47. Jang, D., D. Kim, and J. Moon, *Influence of Fluid Physical Properties on Ink-Jet Printability.* Langmuir, 2009. **25**(5): p. 2629-2635.

48. Ebrahimi Orimi, H., et al., Drop-on-demand cell bioprinting via Laser Induced Side Transfer (LIST). Sci Rep, 2020. **10**(1): p. 9730.

49. Jang, D., D. Kim, and J. Moon, *Influence of fluid physical properties on ink-jet printability.* Langmuir, 2009. **25**(5): p. 2629-35.

50. Vekselman, V., L. Sande, and K.G. Kornev, *Fully magnetic printing by generation of magnetic droplets on demand with a coilgun.* Journal of Applied Physics, 2015. **118**(22).

51. Chia, H.N. and B.M. Wu, *Recent advances in 3D printing of biomaterials.* J Biol Eng, 2015. **9**: p. 4.

52. Ligon, S.C., et al., *Polymers for 3D Printing and Customized Additive Manufacturing.* Chem Rev, 2017. **117**(15): p. 10212-10290.

53. Fried, J., *Polymer Science and Technology*. 2003: Pearson Education.

54. Larson, R.G., The structure and rheology of complex fluids. Vol. 150.

55. Zhao, Z.Y., et al., Novel twin-perovskite nanocomposite of Ba-Ce-Fe-Co-O as a promising triple conducting cathode material for protonic ceramic fuel cells. Journal of Power Sources, 2020. **450**.

56. Bazilevsky, A.V., V.M. Entov, and A.N. Rozhkov, *Breakup of a liquid bridge as a method of rheological testing of biological fluids.* Fluid Dynamics, 2011. **46**(4): p. 613-622.

57. Yarin, A.L., A. Oron, and P. Rosenau, *Capillary instability of thin liquid film on a cylinder.* Physics of Fluids A: Fluid Dynamics, 1993. **5**(1): p. 91-98.

58. Gaskell, S., *Electrospray: Principles and practice.* JOURNAL OF MASS SPECTROMETRY, 1997. **32**(12): p. 1378-1378.

59. Kulakov, M., I. Luzinov, and K.G. Kornev, Capillary and surface effects in the formation of nanosharp tungsten tips by electropolishing. Langmuir, 2009. **25**(8): p. 4462-8.

60. Derby, B., Inkjet Printing of Functional and Structural Materials: Fluid Property Requirements, Feature Stability, and Resolution, in Annual Review of Materials Research, Vol 40, D.R. Clarke, M. Ruhle, and F. Zok, Editors. 2010. p. 395-414.

CHAPTER V

THE MECHANISM OF DROP FORMATION OF WIRE-IN-A-TUBE DOD GENERATOR

5.1 Introduction

As illustrated in **Chapter 4**, a new electroprinting principle has been developed replacing a nozzle-based DOD generator with a wire-in-a-tube drop generator[1, 2]. In the existing prototype of the drop generator, a mechanical pusher moves a tungsten wire through the reservoir to pick up the ink. Due to its high viscosity, the ink is spontaneously deposited on the moving wire like a plum on a thumb of a little boy that sticks his thumb in a pie and pulls it out. Thus, we take advantage of the ink high viscosity resulting in its high stickiness to the wire. When a film of the ink is deposited on the wire, it cannot stay there as a coating film: its surface tension forces the layer to collapse into a drop due to the Plateau-Rayleigh instability[3, 4]. Once the droplet is formed, one can detach it either mechanically, for example, by shaking or spinning the wire, or using electric field by charging the drop[1]. The existing prototype can print single droplets of inks having a surface tension comparable to that of water and viscosity of about 10000 times greater than that of water; the droplets range in diameters from 14 μm to 440 μm.

In this chapter, we discuss the mechanisms of drop formation in the wire-in-a-tube drop generators. These mechanisms couple unique fluid mechanics, capillarity and wetting phenomena providing a new platform that can be used in different microfluidic applications.

5.2 The mechanism of the shear-induced ink pickup

Compared to the pressure-driven drop generators[5], the developed wire-in-a-tube drop generator takes advantage of the viscosity of inks. The ink can be deposited on the wire even

without applying a pressure drop to the ink. The high-speed image sequences recorded at 10,000 fps indicate that the process of drop formation could be divided into two stages: 1) ink pickup and film formation, Fig. 5.1(a)-(b), and 2) drop formation on the wire, Fig. 5.1(c)-(e). The physics of drop detachment and its placement on the target can be separated from that of the drop formation[6-10]. As will be shown below, the limiting stage of the developed technology is the drop formation stage. Therefore, we primarily concentrate our attention on the physics of drop formation.

Fig. 5.1 (a)- (e) Illustration of different stages of drop formation from pure glycerol on the wire of $2R_0$ =150 μm diameter in the tube of internal diameter $2R_1 = 1100$ μm. (a) When the wire moves out from the tube, it displaces the ink from the tube into the cone as illustrated with pure glycerol. (b) The cone collapses into a slender cylindrical finger connecting the wire tip with the tube edge and forming a film on the wire. (c)-(e) A drop nucleates and grows owing to the ink that is squeezed out from the film. Some liquid from the film flows back to the tube and some into a drop. (e) A single droplet forms on the wire. (Reproduced from Ref[11], with the permission of AIP Publishing)

In the first stage, when the wire of radius R_0 moves forward with velocity u, the ink, sticking to the wire surface, moves together with it forming a cone as shown in Fig. 5.1(a) and schematically in Fig. 5.2(a). During this motion, the length l of the wire outside the tube changes with time t as $l = ut$, counting from the moment when the tip of the wire reaches the tube edge

for the first time. This length defines the height of the liquid cone formed at time moment t. The base of this cone is equal to the diameter of the tube bore, $2R_1$.

Having a liquid cone at the end of the pusher stroke is critical for this technology: the dynamics of cone collapse determines the droplet size and its position on the wire. Figures 5.2(d)-(i) illustrate the cone effect showing its influence on the development of Plateau-Rayleigh instability[3, 4, 12, 13]. These experiments demonstrate a striking difference between the drop formation from a collapsing cone and the Plateau-Rayleigh features of drop formation from a coating film.

According to Plateau and a rigorous mathematical analysis of instabilities of cylindrical surfaces [3, 12, 14], one expects that a drop should appear when the stick-out length becomes greater than the Plateau length[3, 14] $l_{Plateau} = 2\pi R_0$. Taking into account the flow in the liquid cylinder, Rayleigh[4] corrected the Plateau factor as $l_{Rayleigh-Plateau} = 2\sqrt{2}\pi R_0$. This criterion also works for thin films of wetting fluids that are prone to form droplets on wires [13, 15, 16]. As the wire length increases beyond $l_{Plateau}$, more droplets should appear on the wire, provided that the length of each drop is about $l_{Plateau}$. Thus, we would expect to have at least two droplets for $l = 8\pi R_0 \cong 2.8 l_{Rayleigh-Plateau}$. As shown in Fig. 5.2(h), this prediction does not work: the capillary suction by the liquid column inside the tube is so strong that it prevents formation of any undulation behind the mother nucleus. The droplet is nucleated closer to the apex of collapsing cone and the nucleus increases in size fed by the liquid films that squeeze the liquid due to capillary action. The smaller the stick-out length, the stronger the influence of the capillary action of the liquid menisci that formed at the tube edge and inside the tube, and the smaller the

droplets size. Only when the stick-out length increases to $l = 9\pi R_0 \cong 3.1 l_{Rayleigh-Plateau}$, a secondary droplet nucleus shows up, Fig. 5.2(i). These observations suggest that the drop formation, in our case, cannot be described by the classical Plateau-Rayleigh instability[3, 4, 12, 13]. The formation of meniscus at the tube edge significantly influences the dynamics of cone collapse.

Therefore, the problem of ink deposition is different from the problem of a wire coating from a tube [17] when the fiber actually pierces the meniscus and moves through it, leaving behind a liquid film. If the cone were pierced by the wire, multiple droplets could appear due to the Plateau-Rayleigh instability. This happens even without the cone piercing when the stick-out length increases as shown in Fig. 5.2(i) and in a series of pictures Fig. 5.3. We leave this complex fluid mechanics problem for future theoretical analysis. For each tube-wire pair, one can experimentally select the stick-out length that would provide a single drop. The rule of thumbs is that one has to avoid the cone "piercing" by the wire on its way out to keep a liquid cone at the end of the pusher stroke. The requirement for cone formation sets on some limitations on the tube-wire pair that we discuss below.

Both ends of the tube are open to the atmosphere, therefore, displacing the liquid from the tube, one simultaneously forms meniscus inside the tube, Fig. 5.2(a). This meniscus meets the internal wall of the tube at contact angle θ_1, and the wire surface at the contact angle θ_0, Fig.5.2(a). To hold the ink inside the tube, one should make the tube wall and the wire wall wettable by the given ink, therefore, $\theta_0, \theta_1 < \pi/2$. The force balance for the meniscus inside the tube is given by the following equation[18-20]:

$$\pi\left({R_1}^2 - {R_0}^2\right)(P_l - P_{atm}) = -\sigma(2\pi R_1 cos\theta_1 + 2\pi R_0 cos\theta_0). \quad (5.1)$$

where P_l is the pressure in the liquid under the meniscus, P_{atm} is the atmospheric pressure, and σ is the surface tension of the liquid. The ink wets the tube and wire surfaces, therefore, the right-hand side of Eq. (5.1) is always negative. Thus, the pressure drop $P_l - P_{atm}$ is also negative suggesting that the meniscus inside the tube always pulls the ink backward. Thus, the suction pressure of meniscus resists the ink displacement setting up an engineering challenge to design not only the wire-in-a-tube system, but the conventional printheads as well. In Ref[10], the effect of the ink backflow into the nozzle of a conventional printhead was studied using Finite Element Method for Navier-Stokes equation with a free boundary where the collapse of internal meniscus was modeled by a phenomenological 1D velocity profile. From one side, the tube-wire system should allow to passively hold the ink inside the tube, and from the other side, it should not significantly resist the ink displacement and cone formation on the wire.

Therefore, there are at least two possible flow scenarios. In one case, the velocity of liquid particles is co-directed with the wire velocity. In another case, the direction of velocity of liquid particles may change inside the liquid layer: closer to the wire some liquid layer will move together with the wire while the rest of the liquid will move in the opposite direction driven by the capillary action of internal meniscus in the tube. We are set to analyze the conditions for such scenarios to occur.

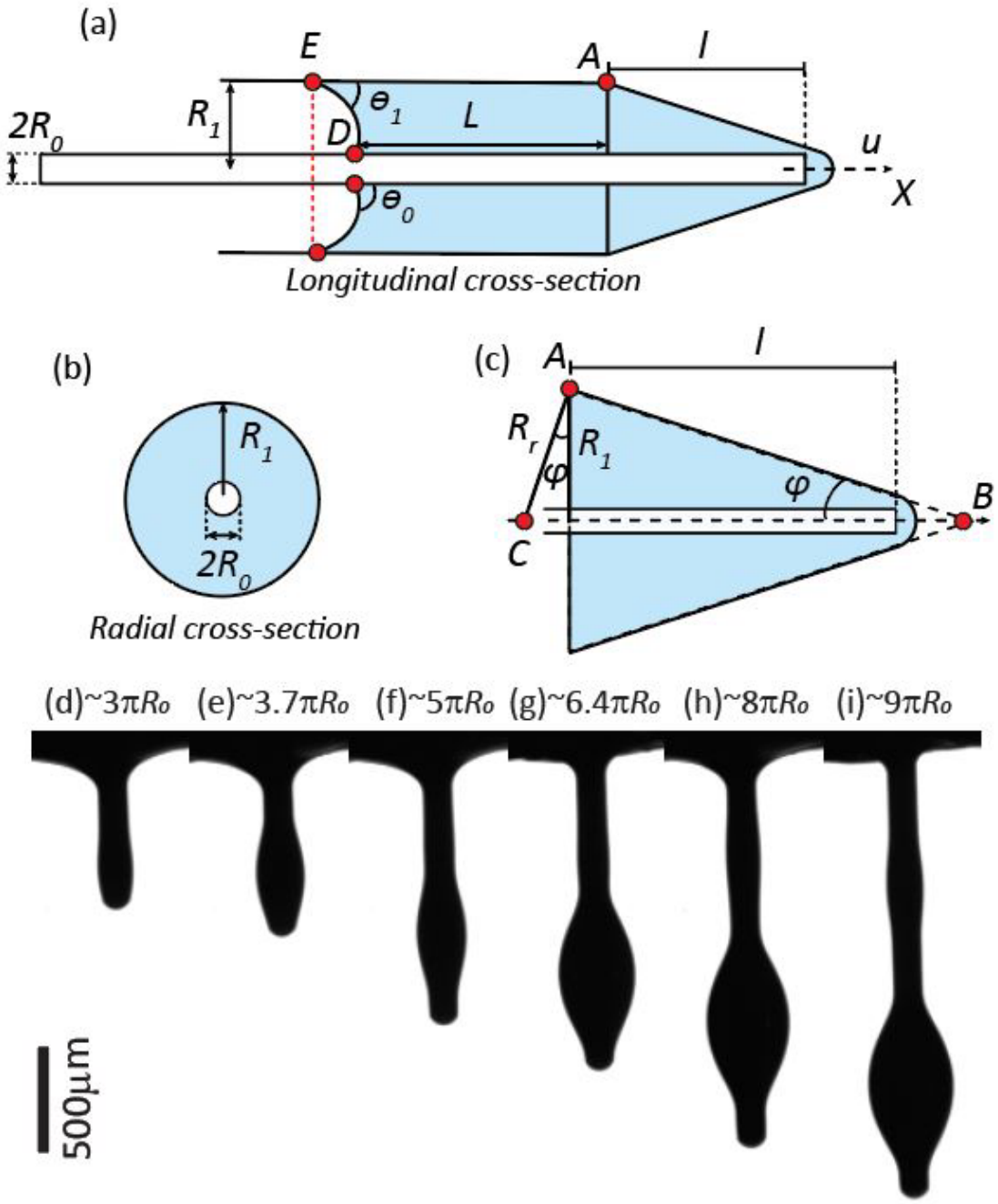

Fig. 5.2 (a) Longitudinal cross-section of the liquid column formed when a wire of radius R_0 moves through the tube of radius R_1 partially filled with a liquid. The wire velocity u is directed in the positive x-direction. At time moment t, the wire piece of length l has moved out of the tube while a liquid column DA of length L is left inside the tube and a cone-like meniscus is formed outside the tube. This liquid cone is stretched between the wire tip and the tube edge A.

Inside the tube, the meniscus forms two contact lines E at the tube wall and D at the wire. Meniscus meets the internal wall of the tube at contact angle θ_1, and the wire surface at the contact angle θ_0. (b) Radial cross-section of the liquid column inside the tube. (c) The radius R_r of curvature of a cone at the edge A of the tube is obtained by drawing perpendicular AC to the cone surface AB. The point C is sitting at the axis of symmetry x and the point B is obtained by drawing line AB along the cone surface until it intersects the x-axis. The angle ABC is the cone angle φ. (d)- (i) Illustration of the effect of stick-out length on the drop formation of pure glycerol on the wire of $2R_0$ =150 μm diameter in the tube of internal diameter $2R_1 =$ 1100 μm. All 6 frames were taken 2 s after the wire has stopped moving.(d) stick-out length $l =$ 700 μm. (e) stick-out length l =870 μm. f) stick-out length l =1175 μm. g) stick-out length l =1500 μm. (h) stick-out length l =1875 μm. (i) stick-out length l =2125 μm. (Reproduced from Ref[11], with the permission of AIP Publishing)

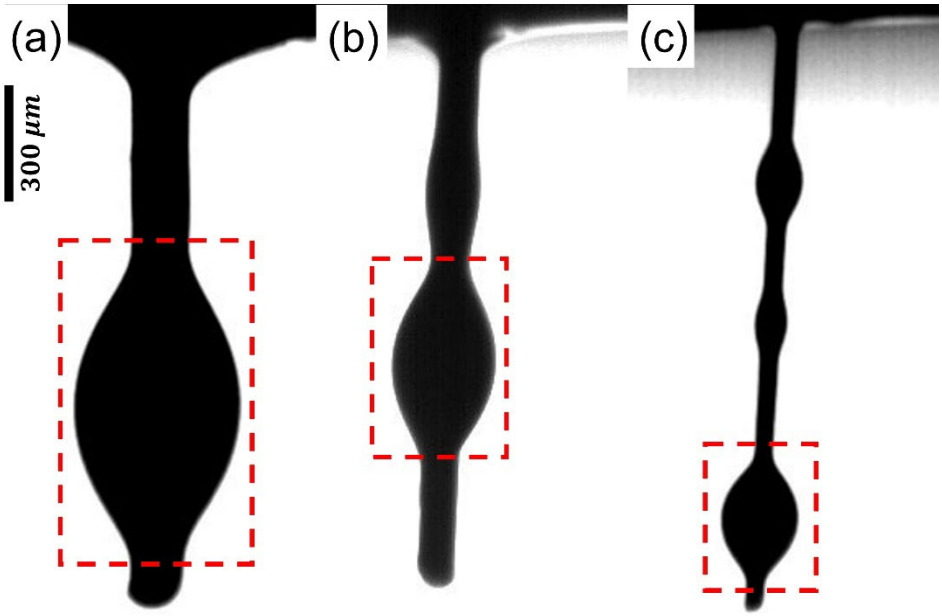

Fig. 5.3 Droplets of pure glycerol formed on different wires in the tube of internal radius $2R_1 = 1100\ \mu m$. (a) A solitary drop formed on the 150 μm wire. (b) A drop with a satellite are formed on the 100 μm wire. (c) Three droplets are formed on the 50 μm wire. For cases when more than one drop formed on the wire, only the largest main drop in the red square was studied. (Reproduced from Ref[11], with the permission of AIP Publishing)

5.2.1 Fluid mechanics of ink displacement from the tube. Problem formulation

Assuming that the liquid column inside the tube is very long, $L \gg R_1$, we can neglect the flow features at the edge of the tube A and at the contact lines E and D. The meniscus width $|ED|$ is assumed much smaller than the column length, $|ED| \ll L$; therefore, the meniscus position is measured with accuracy $|ED|/L$. The flow is modeled as a steady flow parallel to the x-axis. In cylindrical coordinates, this flow is described by the Stokes equation[21] as

$$\frac{\eta}{r}\frac{d}{dr}\left(r\frac{dv}{dr}\right) = \frac{dP_l}{dx}, \tag{5.2}$$

where $v(r)$ is the fluid velocity at the radial coordinate r inside the liquid layer, η is the ink viscosity, P_l is the pressure in the liquid The no-slip boundary conditions on the moving wire and on the non-moving tube wall are written as

$$v_0(\mathrm{R}_0) = u; \quad v_0(\mathrm{R}_1) = 0. \tag{5.3}$$

Differentiating Eq. (5.2) with respect to x and applying the continuity condition, $dv/dx = 0$, one infers that the pressure gradient in the tube is constant, $dP_l/dx = const = (P_{cone} - P_l)/L$, where P_l is the pressure under meniscus in the tube, this pressure is given by Eq. (5.1), and P_{cone} is the pressure under the cone-like meniscus at the edge of the tube A, and L is the length of the liquid column left inside the tube.

The pressure P_{cone} depends on the features of the ink flow in the liquid cone; therefore, it is difficult to estimate this pressure without solving a complex boundary value problem of fluid mechanics. The contribution of the Laplace pressure P_L to the total pressure in the cone P_{cone} can be estimated with the help of Fig. 5.2(c). Introducing the cone angle φ as shown in Fig. 5.2(c) ($\tan\varphi = R_1/l$), we have for the pressure at the tube edge

$$P_L - P_{atm} = \sigma\left(\frac{1}{R_g} + \frac{1}{R_r}\right) = \sigma\left(\frac{1}{\infty} + \frac{\cos\varphi}{R_1}\right) \cong \frac{\sigma}{R_1\sqrt{1 + \left(\frac{R_1}{l}\right)^2}} = \frac{\sigma}{R_1}\frac{1}{\sqrt{\left(\frac{R_1}{ut}\right)^2 + 1}}, \qquad (5.4)$$

where R_g is the radius of curvature of the cone generator, i.e., the straight line, hence $R_g = \infty$. One observes that the pressure differential (5.4) is positive, $P_L - P_{atm} > 0$. Thus, the capillary pressure P_L due to surface tension of the cone is greater than the atmospheric pressure. Therefore, in addition to the suction pressure of meniscus $P_l - P_{atm}$ inside the tube, Eq. (5.1), the capillary pressure of the cone pushes the liquid back to the tube. The magnitude of the pressure in the liquid at the tube edge is always smaller than that at the meniscus inside the tube given by (5.4). The smaller the stick-out length l, $R_1/ut \gg 1$, the smaller the pressure differential $P_L - P_{atm}$. And the smaller the pressure differential $P_L - P_{atm}$, the weaker the capillary action forcing the cone to deform, the more stable the cone is.

Using these inequalities $R_1/ut \gg 1$ and $R_1 \gg R_0$ as a prerequisite for the cone stability, we can limit ourselves to the case $P_L \sim P_{atm}$. In the limit $R_1/ut \gg 1$, the cone surface does not significantly deviate from the flat one and, therefore, we assume that, at these conditions, the velocity inherits its profile from the tube interior. In the unidirectional flow governed by Eq. (5.2) and (5.3), the viscous contribution to the normal stress disappears, $\sigma_{nn} \sim \sigma_{xx} \propto \eta dv/dx = 0$. Thus, in the limit $R_1/ut \gg 1$ we have at the cone surface $P_{cone} \approx P_L \approx P_{atm}$. And the pressure gradient in Eq. (5.2) is obtained as

$$\frac{dP_l}{dx} = \frac{2\sigma(R_1 cos\theta_1 + R_0 cos\theta_0)}{\left(R_1^2 - R_0^2\right)L}, \qquad (5.5)$$

where $L(t)$ is the length of the liquid column inside the tube at the given time moment t.

In order to neglect the capillary pressure in the liquid cone, we evaluate the condition when the capillary pressure under the internal meniscus given by Eq. (5.1) is greater than that of the cone, Eq. (5.5):

$$\frac{\sigma}{R_1\sqrt{1+\left(\frac{R_1}{l}\right)^2}} < \frac{2\sigma(R_1 cos\theta_1 + R_0 cos\theta_0)}{{R_1}^2 - {R_0}^2}, \tag{5.6}$$

We rewrite the inequality (5.6) in the following form

$$\left(\frac{R_1}{l}\right)^2 > F, F = \left[\frac{2(cos\theta_1 + (R_0/R_1)cos\theta_0)}{1-(R_0/R_1)^2}\right]^{-2} - 1. \tag{5.7}$$

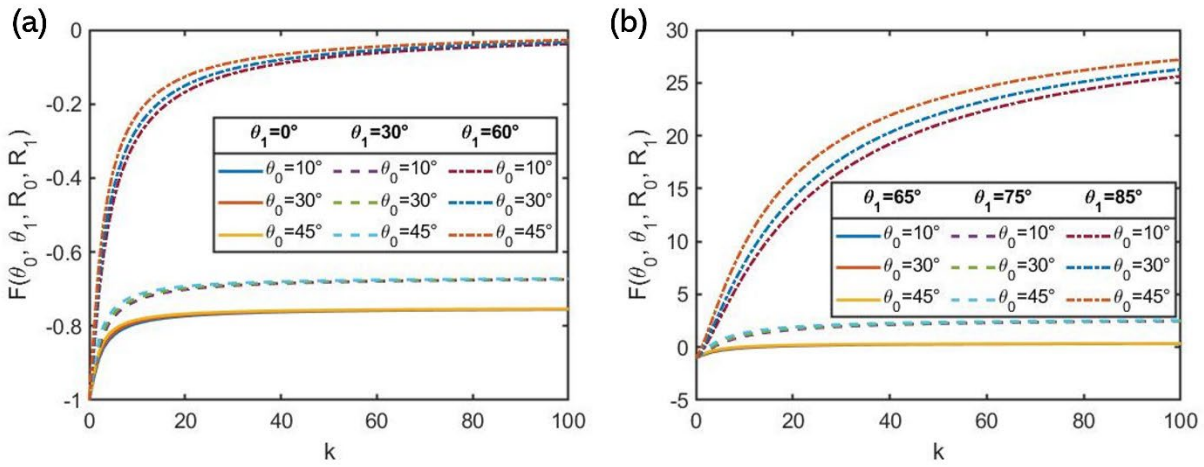

Fig. 5.4 The function F defined in (5.7) is plotted as a function of the dimensionless gap thickness $k = \frac{R_1 - R_0}{R_0} = \frac{R_1}{R_0} - 1$ *for different wetting conditions. (a) Ink approaches the inner tube at a contact angle smaller than* $60°$*. (b) Ink approaches the inner tube at a contact angle larger than* $60°$*.(Reproduced from Ref[11], with the permission of AIP Publishing)*

In Fig. 5.4, the right side of inequality (5.7) is plotted as a function of the gap thickness for different contact angles. When the ink approaches the inner tube at a contact angle smaller than $60°$ (shown in Fig. 5.4(a)), the function remains negative and the inequality (5.7) holds true,

indicating that the capillary pressure under the internal meniscus is much greater than that in the liquid cone. If the same function is plotted with contact angle θ_1 from $60°$ to $90°$ (shown in Fig. 5.4(b)), the inequality (5.7) holds true only when the ratio $\left(\frac{R_1}{l}\right)^2$ is situated above the particular curve in Fig. 5.4(b). In this case, the capillary pressure of the liquid cone is comparable in magnitude with the capillary pressure of the internal meniscus.

With the help of the high speed-motion camera, we observed that inside the tube, the viscous ink approached the moving wire with a large contact angle and the tube wall with small contact angle. When the wire is stationary, the liquid always makes zero contact angle with the wire and the tube. In Fig. 5.5, we compare function $F(\theta_1 = 0°, \theta_0 = 180°)$ with $F(\theta_1 = 0°, \theta_0 = 45°)$, and the results support inequality (5.7).

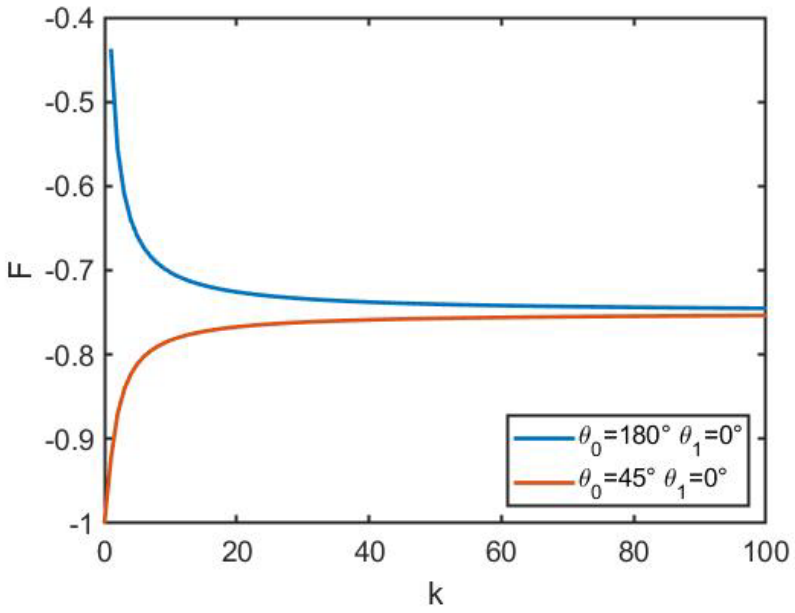

Fig. 5.5 The function F defined in (5.7) is plotted as a function of the dimensionless gap thickness $k = \frac{R_1 - R_0}{R_0} = \frac{R_1}{R_0} - 1$ *for different wetting conditions. (Reproduced from Ref[11], with the permission of AIP Publishing)*

Hence, the assumption $P_L \sim P_{atm}$ holds true for the contact angles $\theta_1 < 60°$ and $\theta_0 < 45°$. We will use these conditions in the analysis of flow scenarios.

5.2.2 Analysis of flow scenarios

We will seek the solution to Eqs. (5.2) and (5.3), Eq. (5.5) as a linear superposition of two solutions,

$$v = v_0 + v_P, \tag{5.8}$$

where velocity v_0 is a solution to Eqs. (5.2) and (5.3), with zero pressure gradient, $\frac{dP_l}{dx} = 0$ and v_P is the solution to Eq. (5.2), with the no-slip boundary conditions

$$v_P(\mathrm{R}_0) = 0; \quad v_P(\mathrm{R}_1) = 0. \tag{5.9}$$

The result is expressed as

$$r = u\frac{\ln\frac{r}{R_1}}{\ln\frac{R_0}{R_1}} + \frac{1}{4\,\eta}\frac{dP_l}{dx}\left[\left(r^2 - {R_0}^2\right) + \frac{{R_1}^2 - {R_0}^2}{ln(R_0/R_1)}ln(r/R_0)\right]. \tag{5.10}$$

And the total flow rate is expressed as

$$Q_{total} = -{R_0}^2\pi u - \frac{\pi u\left({R_1}^2 - {R_0}^2\right)}{2\,ln(R_0/R_1)} - \frac{\pi\sigma(R_1 cos\theta_1 + R_0 cos\theta_0)}{4\eta L}\left[{R_0}^2 + {R_1}^2 + \frac{{R_1}^2 - {R_0}^2}{ln(R_0/R_1)}\right]. \tag{5.11}$$

Introducing the dimensionless gap thickness k as

$$k = \frac{R_1 - R_0}{R_0} = \frac{R_1}{R_0} - 1, \tag{5.12}$$

we rewrite Eq. (5.11) in dimensionless form normalizing the total flow rate Q_{total} by the liquid volume displaced by the wire per unit time, ${R_0}^2\pi u$:

$$\left(\frac{Q_{total}}{{R_0}^2\pi u}\right) = -1 + \frac{(1+k)^2 - 1}{2\,ln(1+k)}$$
$$-\frac{(R_1/L)cos\theta_1 + (R_0/L)cos\theta_0}{4Ca}\left[1 + (1+k)^2 - \frac{(1+k)^2 - 1}{ln(1+k)}\right]. \qquad (5.13)$$

The dimensionless parameter $Ca = \frac{u\eta}{\sigma}$, the capillary number, sets up a metric for the viscous forces relative to the capillary forces.

Small $Ca \ll 1$. When the capillary number is small, the second term in Eq. (5.13) is large and hence the capillary pull of the internal meniscus is strong. Therefore, the total flowrate is negative, $Q_{total} < 0$ and one expects to observe a counterflow when one part of the liquid moves forward with the wire and another part moves backward to the tube.

Large $Ca \gg 1$. When the capillary number is large, the second term in Eq. (5.13) is small implying that the viscous shear forces prevail over the capillary pull of the internal meniscus and the liquid is forced to move out of the tube.

In Fig. 5.6, the dependence $\left(Q_{total}/{R_0}^2\pi u\right)$ on the physical parameters of the wire-in-a-tube system is shown. In these calculations, we fixed $\frac{R_1}{L} = 0.055$ $(R_1 = 0.55\,mm, L = 10\,mm)$and varied the gap thickness to evaluate the conditions when the flow rate changes its sign. The negative flow rate implies that the amount of liquid moving back to the tube due to capillary action is greater than that moving out with the wire.

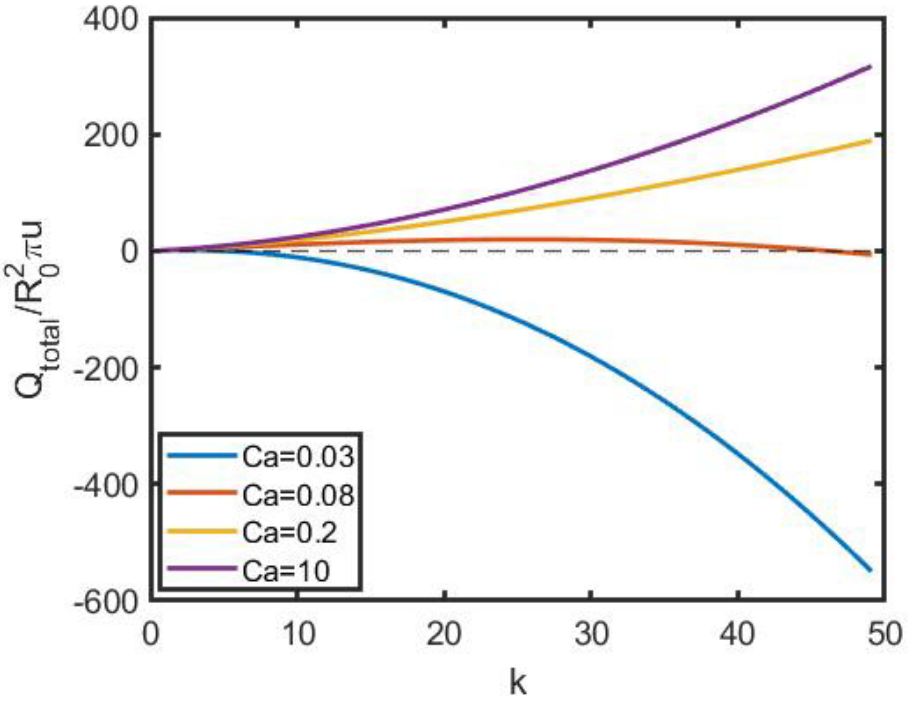

Fig 5.6 The dimensionless flow rate $Q_{total}/{R_0}^2\pi u$ versus k for different capillary numbers Ca. The following parameters $\theta_0 = 45°$ and $\theta_1 = 0°$ have been used in plotting these dependencies. Here, we hold the ration at $\frac{R_1}{L} = 0.055$ ($R_1 = 0.55\ mm, L = 10\ mm$). The radius $R_0 = \frac{R_1}{k+1}$ can be related to the independent variable k. (Reproduced from Ref[11], with the permission of AIP Publishing)

It is instructive to evaluate the conditions when the amount of liquid that has been picked up by the moving wire is equal to the amount of liquid moved back to the tube, referring to the intersection of the red curve and the $x-$axis at $k \approx 46.1, Ca = 0.08$. This condition is $Q_{total}/{R_0}^2\pi u = 0$. Therefore, the internal meniscus DE in Fig. 5.2(a) is not moving: $\pi({R_1}^2 - {R_0}^2)v_{meniscus} = Q_{total} = 0, \rightarrow v_{meniscus} \equiv 0$. This special case is defined by the product CaL/R_1 as

$$\frac{CaL}{R_1} = -\frac{\frac{1}{4}(cos\theta_1 + cos\theta_0/(1+k))\left[1 + (1+k)^2 - \frac{(1+k)^2 - 1}{ln(1+k)}\right]}{1 - \frac{[(1+k)^2 - 1]}{2\,ln(1+k)}}. \tag{5.14}$$

Inspecting this dependence on the contact angles, we observe that due to the factor $1/(1+k)$ at $cos\theta_0$, the dependence of CaL/R_1 on θ_0 is not significant: the larger the dimensionless gap thickness k, the weaker the influence of θ_0 on CaL/R_1.

Fig. 5.7(a) illustrates this behavior where we plot the product CaL/R_1 as a function of the dimensionless gap thickness. When the product CaL/R_1 is above the curve corresponding to the given θ_0, θ_1 in Fig. 5.7(a), one would expect the inequality $Q_{total} > 0$ to hold true. In this case, the forward movement of the wire will result in a net flow discharge and forward movement of the internal meniscus $Q_{total} = \left({R_1}^2 - {R_0}^2\right)v_{meniscus} > 0$. Below this curve, the forward movement of the wire will result in the backward movement of the internal meniscus $Q_{total} = \left({R_1}^2 - {R_0}^2\right)v_{meniscus} < 0$.

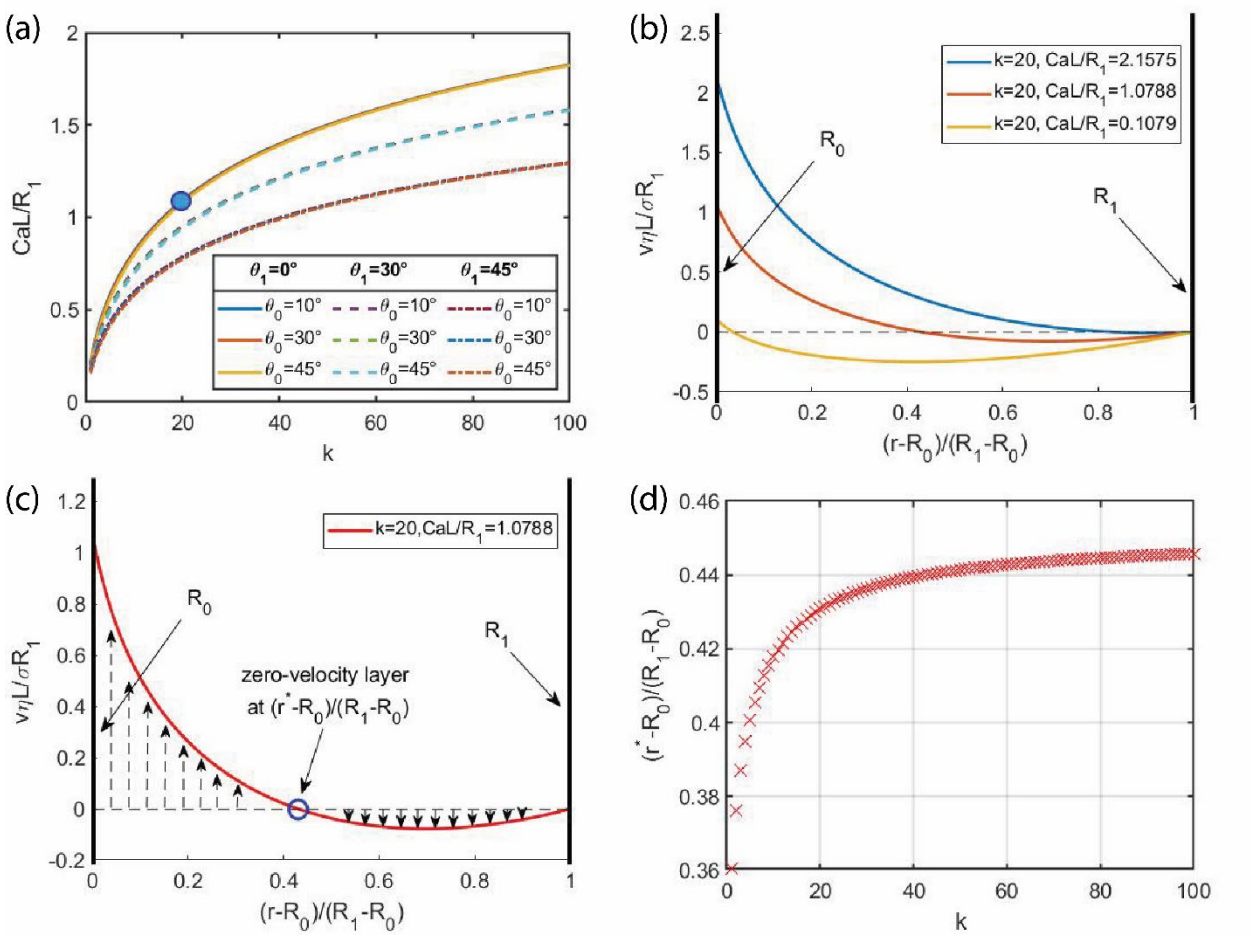

Fig. 5.7 (a) The master curves specifying the product CaL/R_1 versus k as determined by Eq. (5.14). For each dimensionless gap thickness k, and contact angles θ_1 and θ_0, the counter flow is expected to occur for the products CaL/R_1 situated below these curves. If CaL/R_1 is situated above the master curve, the ink moves predominantly with the wire. (b) The dimensionless velocity profile $\frac{v\eta L}{\sigma R_1}$ through the gap with $\theta_0 = 45°$ and $\theta_1 = 0°$ at different k and CaL/R_1. The radial coordinate is taken dimensionless as $(r - R_0)/(R_1 - R_0)$. The wire is on the left and the tube wall is on the right. (c) The dimensionless velocity profile $\frac{v\eta L}{\sigma R_1}$ showing the directions of the velocity vectors for the physical parameters corresponding to the master curve with $k = 20$, $\theta_0 = 45°$ and $\theta_1 = 0°$, marked by the solid dot in Fig. 5.7(a). (d) Dimensionless radial position of the liquid layer $R^* = (r^* - R_0)/(R_1 - R_0)$ with zero velocity. All parameters correspond to the master curves presented by Eq. (5.14) as a function of k with $\theta_0 = 45°$, $\theta_1 = 0°$.(Reproduced from Ref[11], with the permission of AIP Publishing)

To evaluate the condition when the counter flow will first appear, we analyze the velocity profile written in dimensionless form as

$$\frac{v\eta L}{\sigma R_1} = \frac{CaL}{R_1}\frac{ln\frac{r}{R_1}}{ln\frac{R_0}{R_1}}$$

$$+\frac{1}{2}\frac{\left(cos\theta_1 + \frac{R_0}{R_1}cos\theta_0\right)}{\left(1-\frac{{R_0}^2}{R_1}\right)}\left[\frac{\left(r^2-{R_0}^2\right)}{R_1^2}+\frac{1-\frac{{R_0}^2}{R_1}}{ln(R_0/R_1)}ln(r/R_0)\right] \qquad (5.15)$$

Figure 5.7(b) illustrates the dimensionless velocity profile $\frac{v\eta L}{\sigma R_1}$ through the gap. The radial coordinate is taken dimensionless as $(r-R_0)/(R_1-R_0)$, where R_0 is the position of the wire and R_1 is the position of the tube wall. The red curve shows the velocity profile for CaL/R_1 located on the master curve with $k = 20$, $\theta_0 = 45°$ and $\theta_1 = 0°$. The blue curve shows the velocity profile when CaL/R_1 is located above the same master curve. This velocity profile is developed when the internal meniscus moves forward. The yellow curve shows the velocity profile when CaL/R_1 is located below the same master curve. This velocity profile is developed when the internal meniscus moves backward. The liquid layer closer to the moving wire always moves forward together with the wire due to the no-slip boundary conditions.

With increasing the product CaL/R_1, the zero-velocity layer gets closer to the tube. The liquid layer closer to the tube may change the flow direction as one crosses the master curve. Eventually, when the capillary number is large enough, there will be no zero-velocity layer and all fluid would move forward together with the wire.

The critical case represented by the red curve in Fig. 5.7(b) is replotted in Fig. 5.7(c) to show directions of the velocity vectors. The dimensionless velocity of fluid monotonously decreases from $CaL/R_1 = 1.0788$ at the wire $r = R_0$ to zero at $r = 0.43(R_1 - R_0) + R_0$. In the range of $0.43(R_1 - R_0) + R_0 \leq r \leq R_1$, the velocity of the liquid layer increases first then decreases in a negative direction. The total flow rate is expected to be zero in this case. Dimensionless radial position of the liquid layer $R^* = (r^* - R_0)/(R_1 - R_0)$ where the flow velocity is zero is studied in Fig. 5.7(d).

The presented analysis reveals the engineering challenges in design of the wire-in-a-tube system. As shown in Fig. 5.6, the larger the capillary number Ca, the more liquid could be removed from the tube. To avoid the counter flows, one would prefer to select the engineering parameters resulting in the flow regimes corresponding to the CaL/R_1 ratio above the master curve in Fig. 5.7(a). It is also instructive to see that the CaL/R_1dependence on $\theta_0 < \pi/4$ is not significant. High surface energy materials such as metals fall in this category of materials.

5.3 The mechanism of drop formation

5.3.1 Nucleation and formation of droplets on wires

While the wire-in-a-tube DOD generator can print high viscosity inks, the limiting factor for this DOD technology is the time of drop formation: one cannot print the drop until it gets formed. To evaluate the range of characteristic times of drop formation, we studied the dynamics of 1) ink pickup and 2) drop formation. In the first stage of ink pickup, we observe formation of liquid cones and evaluate the time of film formation. In the second stage of drop formation, we study the effect of wire radii and the ink viscosity on time of formation of droplets.

Five tungsten wires with $2R_0 = 150$, $2R_0 = 125$, $2R_0 = 100$, $2R_0 = 75$, and $2R_0 = 50\ \mu m$ diameters were used in experiments. The strength of the tungsten wires guarantees their durability during the long-time printing. Two different tubes with the inner diameter of $2R_1 = 1100\ \mu m$ and $2R_1 = 1570\ \mu m$ were used to study the influence of gap thickness on the features of drop formation. The chosen tube-wire pairs satisfy the condition $R_1/R_0 \gg 1$ required for the cone formation.

Experiments were conducted with mixture of 85 wt%, 90 wt%, and 95 wt% weight percent of glycerol (Glycerin ≥99.7%, Laboratory Reagent, VWR Chemicals BDH®) in water. The higher glycerol concentration, the higher the shear viscosity of solution and the lower its surface tension. Aqueous glycerol solutions of different weight percent of glycerol provided different shear viscosity ranging from $\eta = 894.5\ mPa \cdot s$ to $\eta = 81.92\ mPa \cdot s$ but almost constant surface tension σ.

To increase viscosity even further, we prepared a highly concentrated Ba-Ce-Fe-based sol (BCF) that is used for making ceramic fuel cells[22]. In experiments, the stick-out part of the wire was fixed to about 1500 μm in length. The chosen radii of the wires and the tubes and stick-out length satisfy the condition (5.14).

We calculated the Capillary number of all used in experiments and showed them in Table 5.1.

Table 5.7 Capillary number of solutions used in experiments and CaL/R_1 (Reproduced from Ref[11], with the permission of AIP Publishing)

Solutions	Fluid viscosity η (mPa·s)	Fluid surface tension σ (mN/m)	Velocity u (m/s)	$\mathbf{Ca} = \frac{\eta u}{\sigma}$	$\frac{CaL}{R_1}$
100 wt % Glycerol - water	894.5	63.32	0.75	10.60	182
95 wt % Glycerol - water	337.9	63.55	0.75	3.99	68
90 wt % Glycerol - water	153.6	63.80	0.75	1.81	31
85 wt % Glycerol - water	81.92	64.20	0.75	0.95	16
BCF	6239.6	37.42	0.75	125.07	2146

All Capillary numbers in our experiments were large, $\mathrm{Ca} \gg 1$, confirming that the viscous forces are greater than the capillary forces.

To confirm that we are above the master curve in Fig. 5.7(a) and the cone should be present at the end of the pusher stroke, we need to have the ratio $\frac{CaL}{R_1}$ greater than the right-hand side of Eq. (5.14). With the wire of 150 μm and the tube of $1100\ \mu m$ inner diameter, the cone can be nicely observed (Fig. 5.8). Approximating the liquid cone by a truncated cone, we estimate the volume of liquid that has been displaced from the tube by the wire by subtracting the volume of the wire, πR_0^2, from the volume of the truncated cone, $\frac{1}{3}\pi l(R_1^2 + R_0^2 + R_1 R_0)$:

$$V_{displaced\ liquid} = \frac{1}{3}\pi l(R_1^2 + R_0^2 + R_1 R_0) - \pi R_0^2. \tag{5.16}$$

Where l is the stick-out length, l =1500 μm, $R_1 = 550\ \mu m$, $R_0 = 75\ \mu m$. The length of the liquid column before experiment was $L_0 = 10mm$, and the change of the length due to the ink displacement is $L_c = V_{displaced\ liquid}/\pi(R_1^2 - R_0^2)$. In the product $\frac{CaL}{R_1}$, we use $L = L_0 - L_c$, and the results of $\frac{CaL}{R_1}$ are shown in the last column of Table 5.1. All values are much greater than the

right-hand side of (5.14) for the given $k = 6.33$. This confirms that the cone should be formed as validated with the video analysis.

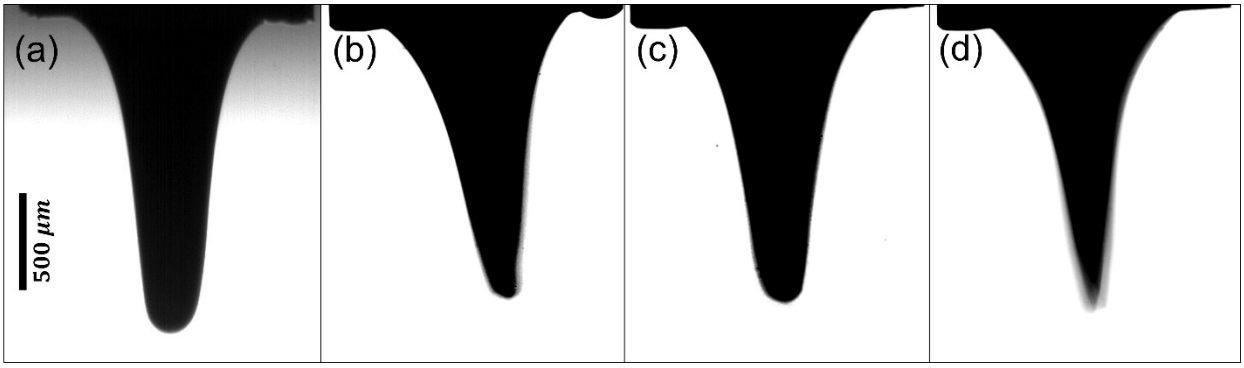

Fig. 5.8 The liquid cone of different aqueous solutions of glycerol formed on 150 μm wires in the tube of internal diameter $2R_1 = 1100$ μm. All four frames were taken 3 ms after the wire started moving. (a) pure glycerol. (b) 95 wt% glycerol-water solution. (c) 90 wt% glycerol-water solution. (d) 85 wt% glycerol-water solution. As the wire stops at the end of the pusher stroke, it still oscillates resulting in some bluriness of the image. (Reproduced from Ref[11], with the permission of AIP Publishing)

Each experiment was repeated 5 times. All videos were recorded at 500 fps for the 150 μm diameter wire and at 1000 fps for 100 μm and 50 μm diameter wires.

5.3.2 Ink pickup

The first stage of fluid pickup and formation of a film from the liquid cone happens very fast. Figure 5.1 illustrates different stages of film formation on a wire of 150 μm diameter. After the wire moves out from the tube to about 1500 μm and the liquid cone forms, the liquid starts to flow back to the tube and transforms in a liquid cylinder as illustrated in Fig. 5.1(a) and Fig. 5.1(b); the process is ended in about 4 milliseconds. When the wire stops moving, a strong backward pressure gradient is developed immediately as explained earlier. This pressure gradient pushes

the liquid back to the tube resulting in formation of a cylindrical film on the wire. The characteristic times for formation of this film are given in Table 5.2.

5.3.3 Drop formation

Once a cylindrical film has been formed, it undergoes the Plateau-Rayleigh instability resulting in the drop formation. Figure 5.1(e) shows the final shape of the drop formed on the wire. At the initial stages of the development of the Plateau-Rayleigh instability, one observes nucleation of a liquid ring on the film surface. During this process, the liquid from cylindrical film moves to the nucleated bump very fast, Fig. 5.1(b) to Fig 5.1(d), and then the drop diameter changes from Fig. 5.1(d) to Fig. 5.1(e) much slowly. This slow process of liquid collection is the limiting stage of the DOD technology which significantly depends on the wire-ink pair.

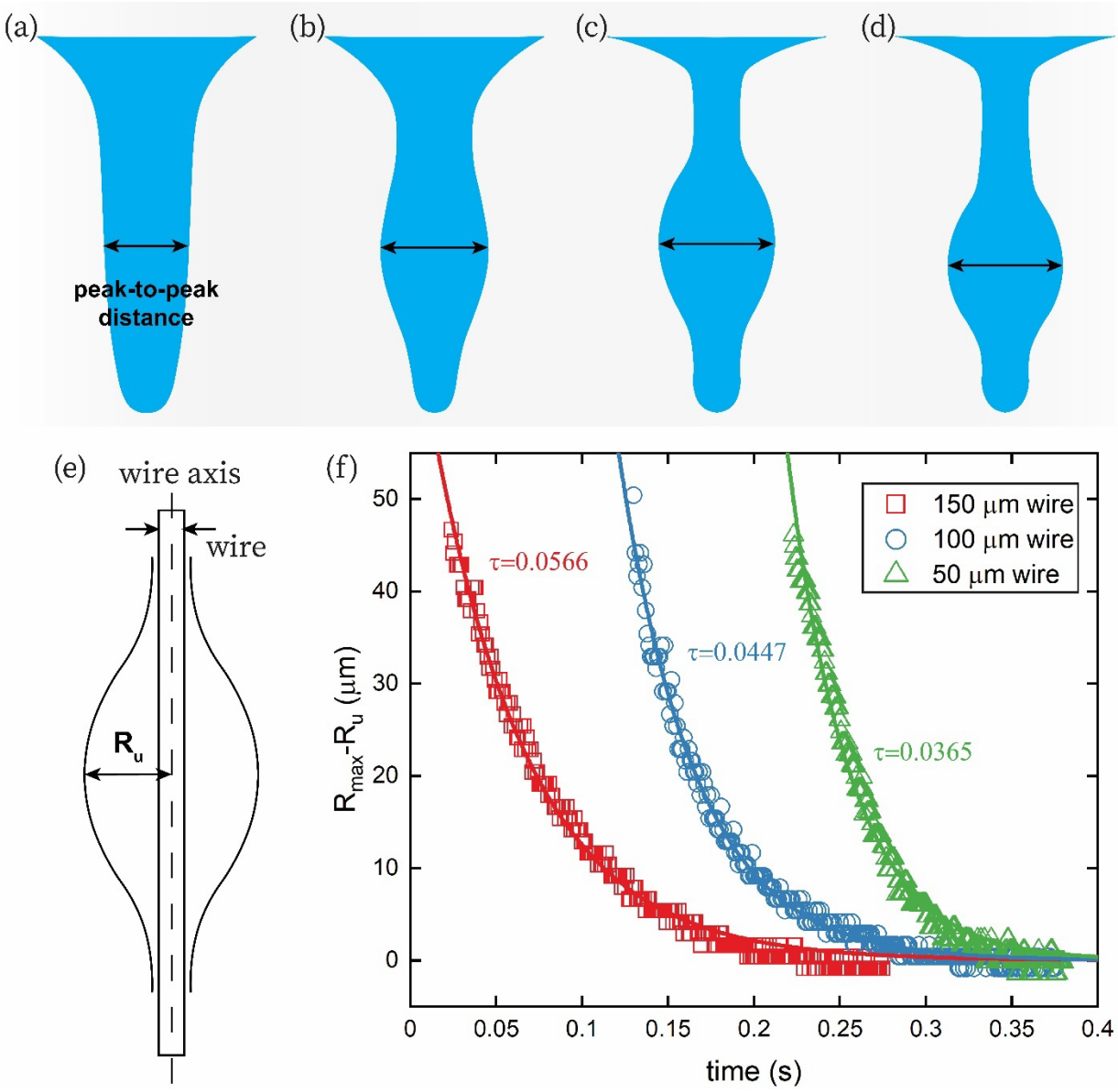

Fig. 5.9 (a)-(d) Different stages of the drop formation. (e) Definition of the drop radius on the wire. (f) The dynamics of formation of a drop from pure glycerol. The incremental change $(R_{max} - R_u)$ of the drop radius R_u from its equilibrium maximum value R_{max} as a function of time. The red squares are experimental data and the red solid curve is the exponential fitting for the 150 μm diameter W-wire; the blue experimental circles and the blue solid fitting curve correspond to the 100 μm diameter wire. The green experimental triangles experimental and the green solid curve correspond to the 50 μm diameter W-wire. For convenience, the blue data set was purposely shifted to the right by 0.1 second and the green data set was purposely shifted to the right by 0.2 second. In all experiments, the tube inner diameter was 1570 μm. (Reproduced from Ref[11], with the permission of AIP Publishing)

We analyzed the peak-to-peak distance of the ring over time (schematically shown in Figs. 5.9(a)-(d)) starting from the frame when the cylindrical film has already been formed (Fig. 5.9(a)). To process the video and to convert the peak-to-peak distance into the drop radius R_u, as defined in Fig. 5.9(e), we used LabView program "IMAQ Extract Contour VI". The drop radius R_u was measured with respect to the final radius R_{max} of the drop. An exponential function $y = A \cdot Exp(-t/\tau)$ was used to fit the observed incremental change of radius $(R_{max} - R_u)$. We call τ the relaxation time of the wire-in-a-tube DOD drop generator and A is the pre-exponential factor.

To evaluate the time of drop formation, we set a threshold value δ for the minimum rate of decline of the fitting curve $y' = -\frac{A}{\tau} \cdot Exp(-t/\tau)$. If $y' \geq \delta$, we consider the drop shape as an equilibrium unduloidal shape with the radius R_{max}. Thus, the time of the drop formation was determined by solving the equation $-\frac{A}{\tau} \cdot Exp\left(-\frac{t_{final}}{\tau}\right) = \delta$ for t_{final} as

$$t_{final} = -\tau \log\left[\frac{-\delta\tau}{A}\right]. \tag{5.17}$$

All the experimental data were collected in Table 5.2. Inspecting the relaxation times, one concludes that the thinner the wire the shorter the relaxation time.

Table 5.8 Parameters of the wire-in-a-tube DOD system. (Reproduced from Ref[11], with the permission of AIP Publishing)

No.	*wire-in-a-tube DOD system*		*Dimensionless gap thickness k*	*Fluid viscosity η (mPa·s)*	*Fluid surface tension σ (mN/m)*	*Drop formation time t_{final} (s)*	*System relaxation time τ (s)*	*Film formation time (s)*	$\frac{R_{max}}{R_0}$
	Tube (inner diameter)	*W-wire (diameter)*							

Glycerol-water solution									
1	1570 μm	50 μm	*30.40*	894.5	63.32	0.132 $\pm$ 0.009	0.035 $\pm$ 0.002	0.018 $\pm$ 0.002	3.15 $\pm$ 0.3
2	1570 μm	100 μm	*14.70*	894.5	63.32	0.167 $\pm$ 0.012	0.047 $\pm$ 0.005	0.018 $\pm$ 0.002	3.60 $\pm$ 0.0
3	1570 μm	150 μm	*9.47*	894.5	63.32	0.173 $\pm$ 0.015	0.053 $\pm$ 0.005	0.014 $\pm$ 0.002	2.74 $\pm$ 0.1
4	1100 μm	50 μm	*21.00*	894.5	63.32	0.031 $\pm$ 0.004	0.006 $\pm$ 0.001	0.004 $\pm$ 0.001	3.18 $\pm$ 0.0
5	1100 μm	100 μm	*10.00*	894.5	63.32	0.050 $\pm$ 0.004	0.010 $\pm$ 0.001	0.004 $\pm$ 0.001	2.74 $\pm$ 0.1
6	1100 μm	150 μm	*6.33*	894.5	63.32	0.107 $\pm$ 0.005	0.032 $\pm$ 0.003	0.008 $\pm$ 0.002	2.73 $\pm$ 0.3
7	1100 μm	150 μm	*6.33*	337.9	63.55	0.113 $\pm$ 0.007	0.030 $\pm$ 0.003	0.012 $\pm$ 0.002	2.71 $\pm$ 0.1
8	1100 μm	150 μm	*6.33*	153.6	63.80	0.111 $\pm$ 0.002	0.029 $\pm$ 0.001	0.012 $\pm$ 0.002	2.71 $\pm$ 0.0
9	1100 μm	150 μm	*6.33*	81.92	64.20	0.102 $\pm$ 0.007	0.021 $\pm$ 0.001	0.010 $\pm$ 0.002	2.77 $\pm$ 0.0
BCF sol									
10	1100 μm	50 μm	*21.00*	6239.6	37.42	0.067 $\pm$ 0.003	0.013 $\pm$ 0.001	0.011 $\pm$ 0.001	2.43 $\pm$ 0.0
11	1100 μm	75 μm	*13.67*	6239.6	37.42	0.063 $\pm$ 0.002	0.014 $\pm$ 0.001	0.009 $\pm$ 0.001	2.73 $\pm$ 0.0
12	1100 μm	100 μm	*10.00*	6239.6	37.42	0.068 $\pm$ 0.006	0.016 $\pm$ 0.003	0.011 $\pm$ 0.001	2.32 $\pm$ 0.1
13	1100 μm	125 μm	*7.80*	6239.6	37.42	0.099 $\pm$ 0.004	0.032 $\pm$ 0.002	0.010 $\pm$ 0.001	2.03 $\pm$ 0.0
14	1100 μm	150 μm	*6.33*	6239.6	37.42	0.072 $\pm$ 0.017	0.050 $\pm$ 0.011	0.017 $\pm$ 0.005	1.28 $\pm$ 0.7

An analysis of the effect of fluid viscosity on the system relaxation time revealed a linear relationship, $\tau \propto \eta$, Fig. 5.10(a) which follows predictions of Refs[15, 16]. According to these references, this scaling suggests that at the late stage of drop formation, the flow from cylindrical

films to the drop is driven by the difference of pressure under the cylindrical films $\sim\sigma/R_0$ and under the drop $\sim 2\sigma/(R_{max}+R_0)$[15, 16]. The pressure in the films is greater than the pressure in the drop and hence the films keep squeezing the liquid toward the drop. In our experiments, this behavior has been confirmed on glycerol solutions with a broad range of viscosities, from η ~80 $mPa\cdot s$ to η ~900 $mPa\cdot s$.

The analysis of the Plateau-Rayleigh instability, while helpful to understand the phenomenon of drop formation, cannot explain all the features. The flow, governing collection of the liquid from the films into the drop, has two contributions: from one side of the droplet, where the film does not communicate with the fluid reservoir, and from the other side where it does. The flow in the film that connects the wire end with the drop, is unidirectional as the pressure in the film is greater than the pressure in the drop. Contrary to that, the flow in the film connecting the drop with the tube is not unidirectional. In one part of the film, which is situated closer to the drop, the liquid is expected to move toward the drop. In another part of the film, which is closer to the tube end, the liquid is expected to move toward the tube where the pressure is lower. The branching point for these flows is not known in advance, it depends on the suction pressure generated by the meniscus at the tube end. Thus, the relaxation time of the drop-on-a-wire system depends on this suction pressure as well, and hence it is expected to depend on the thickness of the gap separating the wire surface from the tube surface. This gap controls the capillary pressure of the internal meniscus and the flow rate inside the tube as discussed in **Chapter 5.2**. In Fig. 5.10(b), we plot the data on the relaxation time for different gap thicknesses k. While we see a generally linear trend of the relaxation time on the gap thickness for both

aqueous glycerol solutions and BCF, there are some deviations owing to a strong capillary action as the gap thickness decreases. We will discuss these effects in the next section.

For printing applications, one would prefer to work with the large gap thicknesses where a linear relation $\tau \propto k$ holds true. Summarizing the results on effect of viscosity and gap thickness on the relaxation time of this DOD technique, we conclude that the trend for the relaxation time is as follows $\tau \propto \eta k$.

As evidenced from Table 5.2, for the large dimensionless gap thickness k, the droplet size is mostly controlled by the wire radius. As the dimensionless gap thickness k decreases, the dimensionless drop size decreases as well.

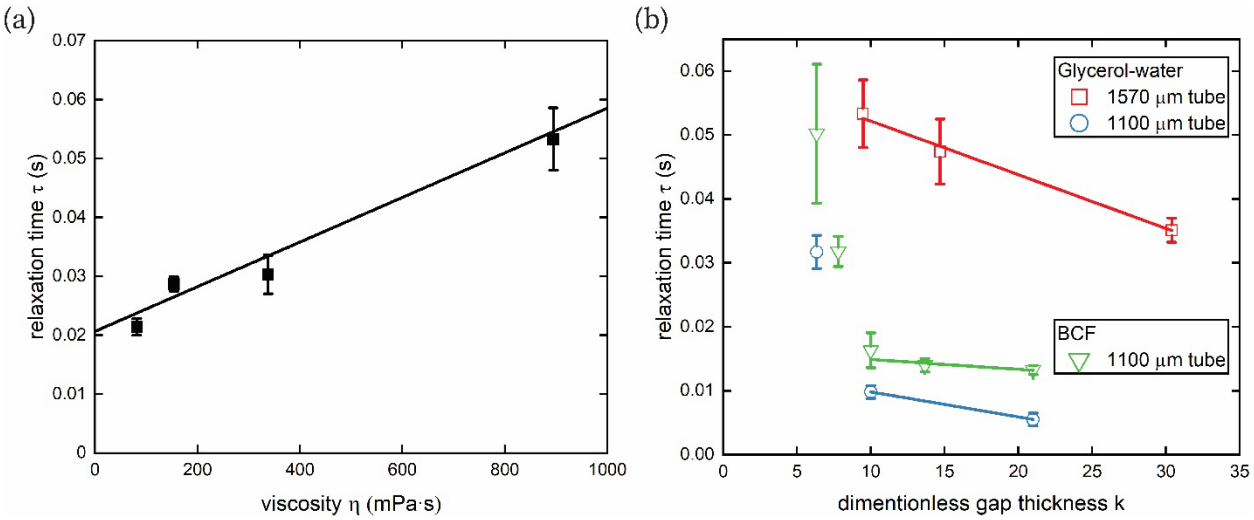

Fig. 5.10 (a) The system relaxation time τ as a function of viscosity η revealed by experiment No. 6-9 from Table 5.2. (b) The system relaxation time τ as a function of dimensionless gap thickness k as revealed by experiments No. 1-6 and 10-14 from Table 5.2. (Reproduced from Ref[11], with the permission of AIP Publishing)

5.4 Interaction of droplet with meniscus

In the analysis of the drop-meniscus interaction, we assume that the drop and meniscus shown in Fig. 5.11, are described by their equilibrium shapes, unduloids for droplets and nodoids

for menisci[23]. These solutions are unique solutions for the family of constant mean curvature surfaces. This assumption will be further verified in experiments. Thus, the entire profile of the liquid body forming the drop and meniscus is represented by an unduloid connecting to a nodoid, Fig. 5.11(b). The model is detailed in **Chapter 2**.

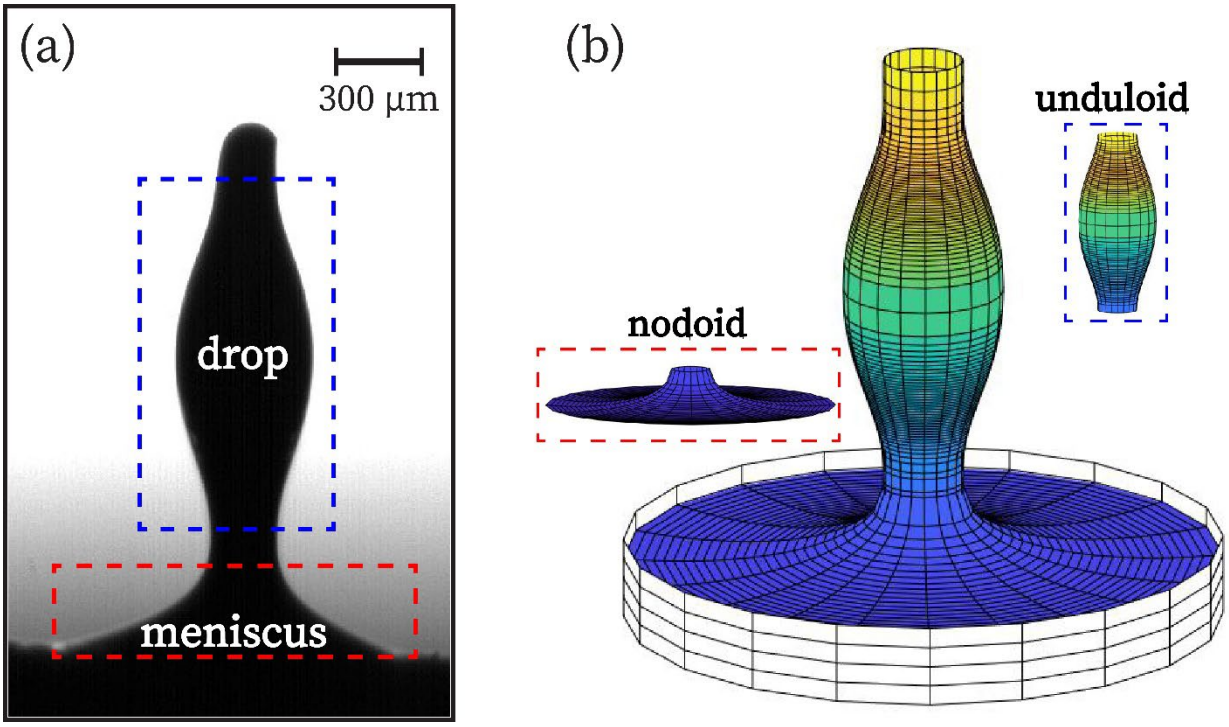

Fig. 5.11 (a) A drop is modeled as an unduloid and a meniscus is modeled as a part of nodoid. (b) An illustrative example of the unduloid-nodoid pair describing the liquid body in Fig. 5.11(a). The white cylinder represents the tube wall. A part of the meniscus is hidden under the tube wall. (Reproduced from Ref[11], with the permission of AIP Publishing)

The tube partially hides the meniscus and, therefore, in experiments, the contact angle θ_t in Fig. 5.12(a) that this meniscus forms with the tube wall is not possible to observe. Only the part of meniscus marked by the hollow red circles in Fig 5.12(b) is visible. Due to an incomplete image of the meniscus profile, we were not able to measure the contact angle θ_t directly. To address

this challenge, we used the method of Ref.[18] and introduced a new parameter, the end of the visible meniscus positioned at the distance $y = R_m$ from the wire axis. At this visible boundary, meniscus makes angle θ_{m} with the wire axis, Fig. 5.12(b).

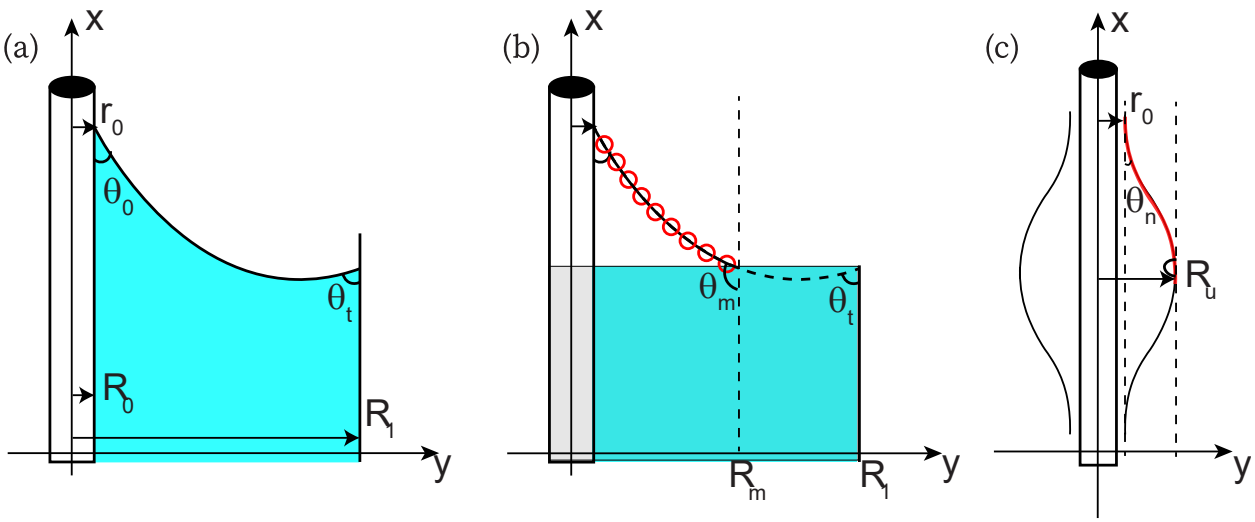

Fig. 5.12 (a) Schematic of a part of axisymmetric meniscus (blue) with the radial coordinate y and axial coordinate x. At the film surface $y = r_0 = R_0 + h'$, where R_0, is the wire radius and h' is the film thickness, meniscus makes contact angle θ_0 and at the end of the tube at $y = R_1$, the meniscus makes angle θ_t with the tube. (b) The visible part of meniscus is shown with the red circles. The vertical dashed line marks the radial coordinate $y = R_m$ of the visible meniscus. The shaded rectangle is the tube that hides from observing the meniscus and the rest of the wire. (c) Schematic of an axisymmetric unduloidal drop where R_u is the drop radius measured from the wire axis, and r_0 is the radius of the film. We set the zero contact angle, $\theta_n = 0$, that the drop makes with the film. (Reproduced from Ref[11], with the permission of AIP Publishing)

Since the wire is coaligned with the tube axis, it is safe to say that the meniscus profile is symmetric with respect to the wire axis. We set the wire axis to sit at $y = 0$ and assign Cartesian (y, x) coordinates so that one side of the film would have positive y-coordinate and the other side would have negative y-coordinate. The designed LabVIEW program can simultaneously extract the meniscus profile from the image and symmetrize the profile by taking an average

between the y-coordinates of both sides of the meniscus. Once this summarization procedure is done, we consider film profile axisymmetric and use the nodoid and unduloid models to describe meniscus and drop, respectively. The details are given in **Chapter 2**.

To evaluate the effect of flow in the film, we introduce a new parameter, the goodness of fit (gof) as: $\text{gof} = \frac{\sum_1^n \sqrt{\frac{X_i - x_i}{x_i}^2 + \frac{Y_i - y_i}{y_i}^2}}{n}$, where n is the number of data points extracted from the image, (Y_i, X_i) are the coordinates of symmetrized experimental data, (y_i, x_i) are perdictted coordinates of the nodoid or unduloid models. For each analyzed frame, the contact angle θ_t providing the smallest gof is considered as the best-fit angle. Since the unduloid model always partially or completely described the drop with zero contact angle, there were no need to search for the best-fit parameter.

The experimental profiles of the drops and menisci formed on the wire of radius $2R_0 = 150\ \mu m$ and the tube internal radius $2R_1 = 1100\ \mu m$ were examined in detail. In Fig. 5.13, we show a gallery of pictures describing the drop dynamics and the corresponding fits of the drop and menisci profiles at different time moments.

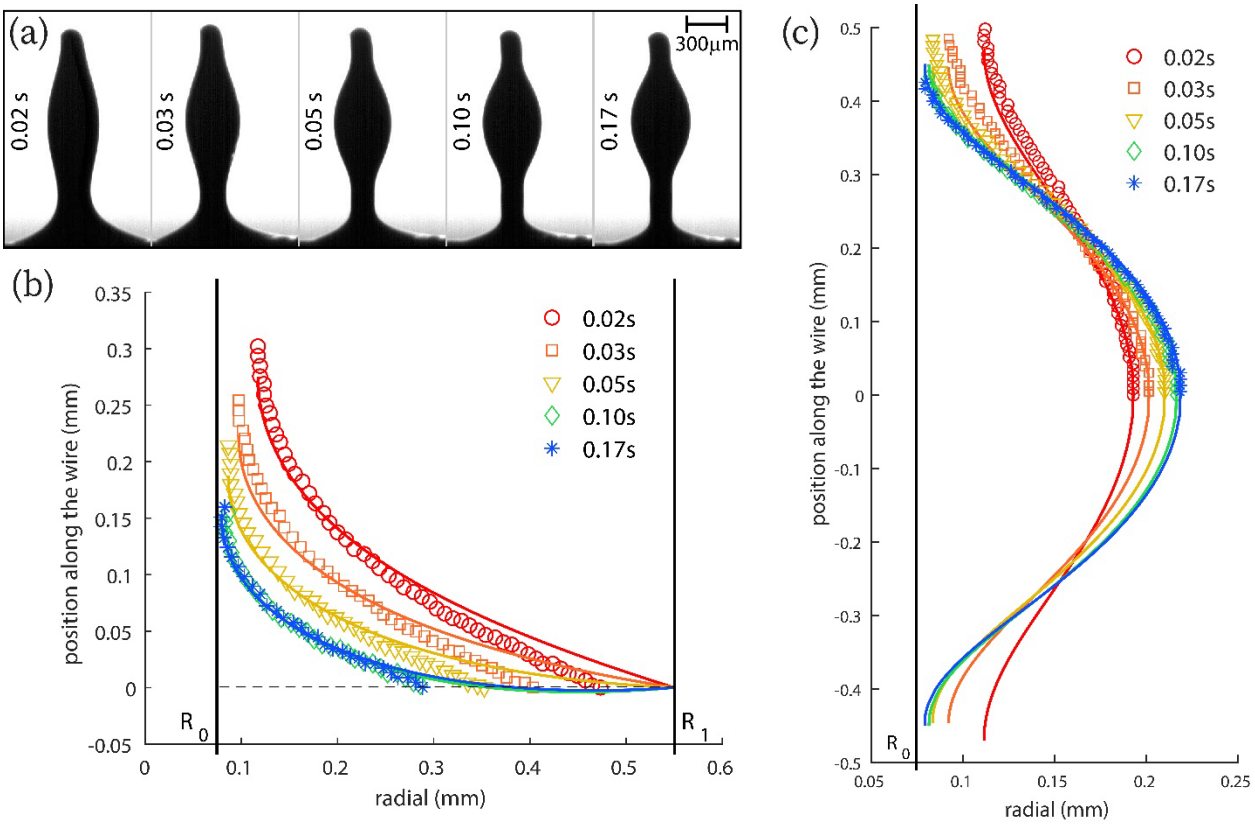

Fig. 5.13 (a) A gallery of images showing dynamics of drop formation after the wire of radius $2R_0 = 150$ μm stopped moving. (b) The scattered symbols show the profile of the meniscus at different time moments, and the solid lines of the same colors corresponding to the symbols show nodoid model specified by fitting the experimental profiles by adjusting the contact angle θ_t. (c) The best fit of the droplets shown in Fig. 5.13(a) with the unduloid model. The scattered symbols are experimental profiles, and the solid lines are the unduloids. (Reproduced from Ref[11], with the permission of AIP Publishing)

Inspecting Fig. 5.13 (b) and Fig. 5.13(c), we observe that the nodoid and unduloid models provide fairy well description of the film profile at the late stage of the film relaxation to its equilibrium configuration. However, at the beginning of the film collapse, the experimental data do not match the models very well. Knowing how fast the meniscus and drop relax to their equilibrium shapes, one can better understand the flow dynamics. Thus, the goodness of fit of

nodoid and unduloid are examined and reported in Fig. 5.14 (a) and Fig. 5.14(b), respectively, where the error bars give the corresponding standard deviations.

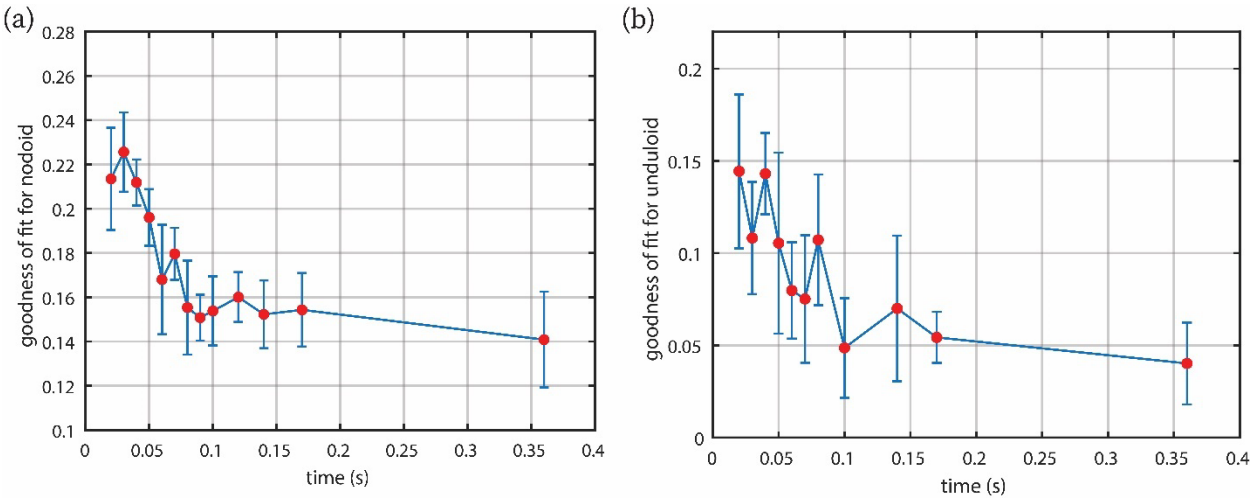

Fig. 5.14 (a) The goodness of fit for nodoid - meniscus as a function of time. (b) The goodness of fit unduloid -drop as a function of time. (Reproduced from Ref[11], with the permission of AIP Publishing)

In Fig. 5.14(a), the gof show its fast decrease over the first ~0.10 seconds indicating that the flow still deforms the meniscus profile during that period. After that, the relatively small gof value less than 0.15 shows that the model fits the profile nicely suggesting that an equilibrium meniscus has been formed. After 0.10 seconds, an average best-fit contact angle $\theta_t = 86.4 \pm 1.7°$ has been established.

A very similar gof trend can be observed in Fig. 5.14(b) for unduloidal drop. The goodness of fit for unduloid (gof<0.05) is overall better than that for the nodoid (gof <0.15). Meaning that the drop configuration is closer to its unduloidal equilibrium shape than the meniscus, which implies that the flux inside the meniscus is probably stronger than the flux inside the drop. Furthermore,

the time interval of 0.10 seconds taken as a characteristic time for drop formation is in a good agreement with the estimated drop formation time reported in Table 5.2.

With the given good description of the film profile by the unduloid and nodoid models we can evaluate the pressure distribution in the drop-film pair and meniscus-film pair. In Fig. 5.15(a), we report the results of five experiments. Each trend line is obtained by averaging the results of these experiments. The error bars give the corresponding standard deviations. The graphs show that the pressure under nodoidal meniscus is less than the atmospheric pressure ($P_{nodoid} - P_{atm} = -2\sigma(R_1 \cos\theta_t + r_0)(R_1^2 - r_0^2)^{-1}$) and under unduloidal meniscus it is greater than the atmospheric pressure($P_{unduoid} - P_{atm} = 2\sigma(R_{\mathrm{u}} - r_0)(R_{\mathrm{u}}^2 - r_0^2)^{-1}$). Thus, when the liquid bridge connects meniscus with the drop, there should be a net flow from the drop toward meniscus.

The pressure P_{flim} in the liquid bridge connecting the drop with meniscus is obtained from the Laplace equation as $P_{flim} - P_{atm} = \frac{\sigma}{r_0}$, where r_0 is found from the meniscus fitting and P_{atm} is the atmospheric pressure. In Fig. 5.15(b), the pressure differential between the liquid bridge and the drop and between the liquid bridge and the meniscus are plotted separately as functions of time. The pressure differential between the liquid bridge and the meniscus is larger than that between the liquid bridge and the drop. Hence, the liquid from the liquid bridge moves to both sides all the time but the liquid discharge toward meniscus is expected to be greater.

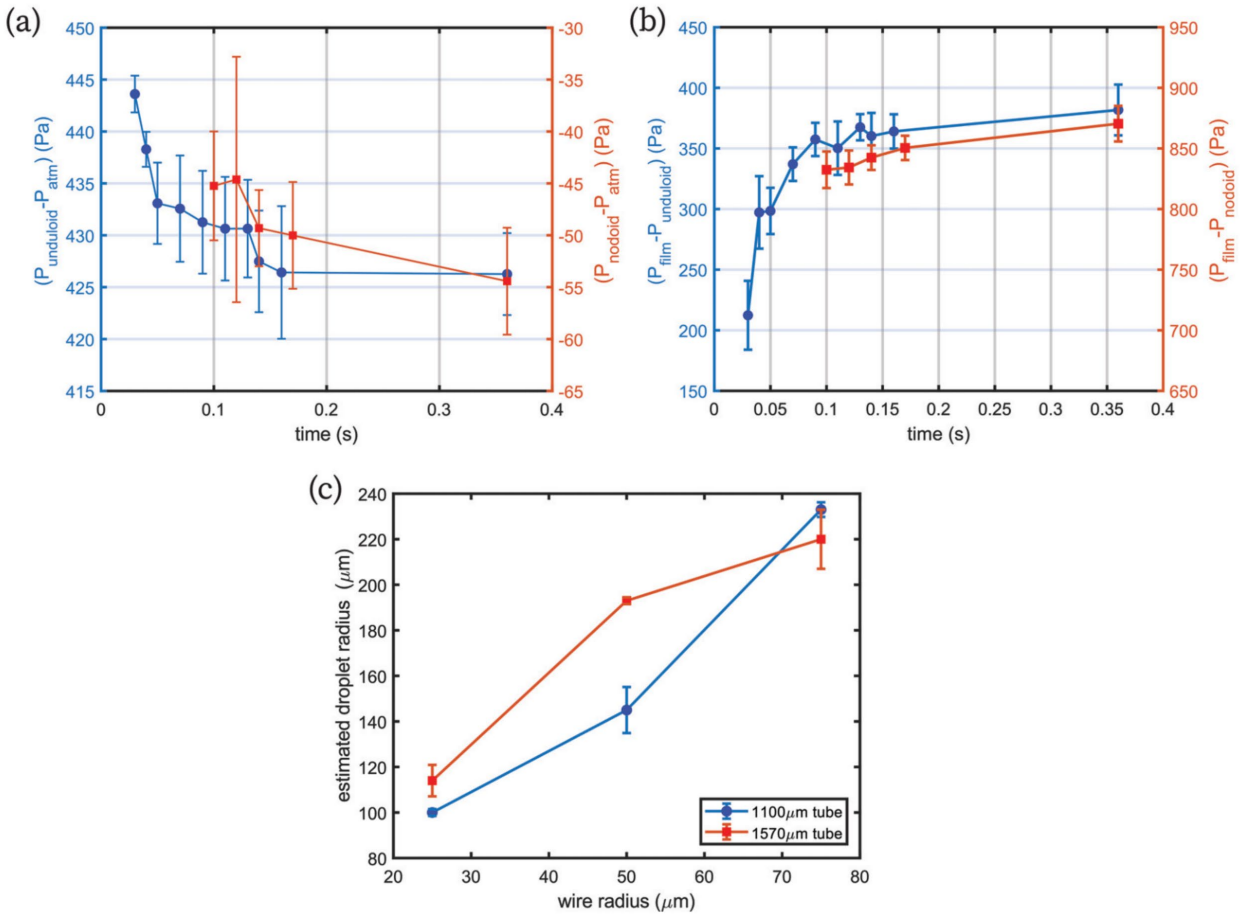

Fig. 5.15 (a) The pressure differential in the drop (the blues circles) and the meniscus (the red squares) relative to the atmospheric pressure are plotted versus time. (b) The pressure differential between the liquid bridge and the drop (the blue circles) as a function of time. The pressure differential between the liquid bridge and the meniscus (the red squares) as a function of time. (c) A theoretical estimate of the droplet radius $R_{drop} = \sqrt[3]{\frac{3}{4\pi}V_{unduloid}}$ *as a function of the wire radius. (Reproduced from Ref[11], with the permission of AIP Publishing)*

The unduloid model allows us to estimate the radius of the formed droplet as a function of the wire radius as $R_{drop} = \sqrt[3]{\frac{3}{4\pi}V_{unduloid}}$. Figure 5.15(c) provides such an estimate.

Although we used only two different tubes, the estimated drop size formed on each wire does not significantly reflect the tube size's influence. For both groups of experiments, the estimated drop radius is roughly proportional to the wire radius. This result suggests that one

would be able to control the size of generated drop by only changing the wire in this wire-in-a-tube DOD technique.

5.5 Conclusion

In this chapter, we discuss the mechanisms of drop formation in the wire-in-a-tube drop generators. We suggested a fluid flow model explaining the ink pickup where the wire move through the tube displacing the ink from it. When the ink is displaced by the moving wire, it forms meniscus inside the tube. We investigated different regimes of flow when the internal meniscus would move toward the tube end together with the wire or when it will move backward pulling the displaced ink back into the tube. The effect of the wire-tube gap thickness, capillary suction, and viscous force on the amount of displaced ink were studied and the results are summarized in Fig. 5.6 and Fig. 5.7. These results can be used not only for development of the wire-in-a-tube printing devices but can be generally used for development of the fiber coating methods when one threads a fiber through a liquid-filled tube[24-27].

Then we experimentally studied the dynamics of drop formation in the wire-in-a-tube generators. The results are collected in Table 5.2. We specified the features of drop interaction with the meniscus formed at the tube end and studied the mechanisms of liquid flow to the drop and meniscus. As shown, the drop configuration at the late stage of its formation is well described by the unduloid model; at the same time scale, the meniscus configuration is well described by the nodoid model. Using these two models, we evaluated the pressure distribution in the drop-liquid bridge-meniscus triplet. It is inferred that the ink is mostly moving from the liquid bridge toward meniscus. This preferential flow explains the mechanism of formation of drop on demand:

once the drop is nucleated, it grows by pulling the liquid mostly from the film. The liquid bridge connecting this nucleated drop with meniscus squeezes the ink down to the tube hindering communication of the drop with the feeding tube. This way, the drop remains dynamically isolated from the feeding tube. The depletion and breakup of this liquid bridge works in favor of this DOD technology. The size of the final drop is mostly controlled by the stick-out length of the wire and the wire radius. We showed that the thinner the wire and the wider the wire-tube gap thickness, the shorter the time of drop formation.

Therefore, when a specific drop radius is required for printing, one needs to choose a wire of specific diameter and a stick-out length. In practical applications, it will be convenient to calibrate a series of wires and change the wires to achieve different drop radii.

5.6 References

1. Andrukh, T., B. Rubin, and K.G. Kornev, *Wire-in-a-nozzle as a new droplet-on-demand electrogenerator.* Langmuir, 2011. **27**(6): p. 3206-10.
2. Vekselman, V., L. Sande, and K.G. Kornev, *Fully magnetic printing by generation of magnetic droplets on demand with a coilgun.* Journal of Applied Physics, 2015. **118**(22).
3. Plateau, J., Experimental and theoretical researches on the figures on equilibrium of a liquid mass withdrawn from the action of gravity, in Annual Report of the Board of Regents of the Smithsonian Institution 1863, Smithsonian Institution: Washington, DC. p. 207–285.
4. Rayleigh, L., *On the capillary phenomena of jets.* Proc. R. Soc. Lond. A, 1879. **29**: p. 71-97.
5. Basaran, O.A., Small-scale free surface flows with breakup: Drop formation and emerging applications. Aiche Journal, 2002. **48**(9): p. 1842-1848.
6. Feng, J.Q., A general fluid dynamic analysis of drop ejection in drop-on-demand ink jet devices. Journal of Imaging Science and Technology, 2002. **46**(5): p. 398-408.
7. Dong, H., W.W. Carr, and J.F. Morris, *An experimental study of drop-on-demand drop formation.* Physics of Fluids, 2006. **18**(7).
8. Fromm, J.E., *Numerical-Calculation of the Fluid-Dynamics of Drop-on-Demand Jets.* Ibm Journal of Research and Development, 1984. **28**(3): p. 322-333.
9. Reis, N., C. Ainsley, and B. Derby, *Ink-jet delivery of particle suspensions by piezoelectric droplet ejectors.* Journal of Applied Physics, 2005. **97**(9).

10. Xu, Q. and O.A. Basaran, *Computational analysis of drop-on-demand drop formation.* Physics of Fluids, 2007. **19**(10).

11. Sun, Y., et al., Making droplets from highly viscous liquids by pushing a wire through a tube. Physics of Fluids, 2022. **34**(3).

12. Lowry, B.J. and P.H. Steen, *Capillary Surfaces - Stability from Families of Equilibria with Application to the Liquid Bridge.* Proceedings of the Royal Society-Mathematical and Physical Sciences, 1995. **449**(1937): p. 411-439.

13. Haefner, S., et al., Influence of slip on the Plateau-Rayleigh instability on a fibre. Nat Commun, 2015. **6**: p. 7409.

14. Plateau, J., Statique Experimentale et The´orique des Liquides Soumis aux Seules Forces Mole´culaires. 1873, Paris,: Gauthier–Villars,.

15. Johnson, M., et al., The nonlinear growth of surface-tension-driven instabilities of a thin annular film. Journal of Fluid Mechanics, 1991. **233**: p. 141-156.

16. Yarin, A.L., A. Oron, and P. Rosenau, *Capillary instability of thin liquid film on a cylinder.* Physics of Fluids A: Fluid Dynamics, 1993. **5**(1): p. 91-98.

17. Kim, O. and J. Nam, *Confinement effects in dip coating.* Journal of Fluid Mechanics, 2017. **827**: p. 1-30.

18. Nave, M.I., et al., Is an electric field always a promoter of wetting? Electro-dewetting of metals by electrolytes probed by in situ X-ray nanotomography. Faraday Discussions, 2017. **199**: p. 101-114.

19. Birdi, K.S., Handbook of surface and colloid chemistry. 2016.

20. Gennes, P.-G., F. Brochard-Wyart, and D. Quéré, *Capillarity and Wetting Phenomena: Drops, Bubbles, Pearls, Waves*. 2004, New York: Springer.

21. Batchelor, G.K., *An introduction to fluid dynamics*. 2000, New York: Cambridge University Press.

22. Zhao, Z.Y., et al., Novel twin-perovskite nanocomposite of Ba-Ce-Fe-Co-O as a promising triple conducting cathode material for protonic ceramic fuel cells. Journal of Power Sources, 2020. **450**.

23. Langbein, D.W., Capillary Surfaces: Shape - Stability - Dynamics, in Particular Under Weightlessness Springer Tracts in Modern Physics. 2002, New York: Springer.

24. Levy, H., A.J. Lockyer, and R.G.C. Arridge, *Coating of fibers.* International Journal of Heat and Mass Transfer, 1978. **21**(4): p. 435-443.

25. Kistler, S.E. and P.M. Schweizer, eds. *Liquid film coating. Scientific principles and their technological implications*. 1997, Chapman & Hall: Glasgow, UK. 783.

26. Quere, D., *Fluid coating on a fiber.* Annual Review of Fluid Mechanics, 1999. **31**: p. 347-384.

27. Deryagin, B.M. and S.M. Levi, *Film Coating Theory*. 1964, New York: The Focal Press. 164.